THERMAL CHARACTERIZATION OF HEATED MICROCANTILEVERS AND A STUDY ON NEAR-FIELD RADIATION

A Dissertation
Presented to
The Academic Faculty

by

Keunhan Park

In Partial Fulfillment
of the Requirements for the Degree
of Doctor of Philosophy in the
George W. Woodruff School of Mechanical Engineering

Georgia Institute of Technology
May 2007

THERMAL CHARACTERIZATION OF HEATED MICROCANTILEVERS AND A STUDY ON NEAR-FIELD RADIATION

Approved by:

Dr. Zhuomin Zhang, Co-Advisor
George W. Woodruff School of Mechanical Engineering
Georgia Institute of Technology

Dr. William P. King, Co-Advisor
George W. Woodruff School of Mechanical Engineering
Georgia Institute of Technology

Dr. Yogendra Joshi
George W. Woodruff School of Mechanical Engineering
Georgia Institute of Technology

Dr. Samuel Graham
George W. Woodruff School of Mechanical Engineering
Georgia Institute of Technology

Dr. Mark G. Allen
School of Electrical and Computer Engineering
Georgia Institute of Technology

Dr. Alexei Marchenkov
School of Physics
Georgia Institute of Technology

Date Approved: March 27, 2007

ACKNOWLEDGEMENTS

My doctoral thesis and related achievement would not be possible without the assistance, cooperation, and support from a number of colleagues, friends and family.

I would first like to thank my advisors, Dr. Zhuomin Zhang and Dr. William King, for providing a careful balance of discipline, mentorship, and encouragement throughout my studies at Georgia Tech. I am also deeply grateful to my dissertation committee members. Dr. Samuel Graham has always made himself available whenever I needed his advice on research and teaching. I am indebted to Dr. Alexei Marchenkov for not only letting me use his lab facilities but teaching me details of cryogenic experiments. I want to thank Dr. Yogendra Joshi and Dr. Mark Allen for providing valuable suggestions for the improvement of this work and supporting me for my future career path.

There are many people who have helped my PhD research through their collaborations. First of all, I thank Dr. Graham Cross at Trinity College Dublin for his invaluable help in my research with nanothermometer fabrication. The collaboration with Jungchul Lee in the cantilever research was a great experience. In topography experiments, I greatly appreciate productive discussions with Dr. Kyoung Joon Kim. I thank Bong Jae Lee and Dr. Ceji Fu for their invaluable help in the surface polariton research. It was great fun to work with Soumya Basu in the near-field TPV study. I thank Brent Nelson for teaching me how to use AFM when I knew nothing about it.

My colleagues in the nanoscale thermal radiation lab (NTRL) and nanoscale thermal processing lab (NTPL) have always been a constant source of support and friendship. Dr. Hyunjin Lee is like my brother. Through our struggles and successes we made bonds for life. Dr. Qunzhi Zhu, Yu-Bin Chen, and Qinghe Li have made the NTRL

special. Our “Asian network” will last for the life time. Harry Rowland, Joe Charest, Tanya Wright, Fabian Goericke, Marcus Eliason, Shubham Saxena, Andrew Cannon, and Dr. Fuzheng Yang in the NTPL have made my days stuck to AFM bearable, meaningful, and sometimes enjoyable. Erik Sunden, Adam Christensen, Abe Greenstein, Namsu Kim, Thomas Beechem, and Rodrick Jackson in Dr. Graham’s group should be remembered for their brightness and warm hearts.

I am blessed to serve such a good church as New Church of Atlanta during my years in Atlanta. I would like to thank Rev. Bill Sim and Rev. Junho Kim for strengthening my faith. I cannot forget great times I have spent with Korean friends. My seniors; Seungwon Shin, Youngbin Park, Heungjoo Shin and their families have given me truly warm encouragement. Warm thanks to Yoonjo, Sangil, Jisung, Hoyeon, Jaemin, Hyunjung, and many other friends. I owe many big things to my old friends, Taesik and Hyunsoo. They have been my friends and my brothers. Here, I engrave their names appreciating their friendships for such a long time. I should not forget my high school teacher, Mr. Gilseop Hyun, and my former advisor, Dr. Sung Tack Ro. They are my role models as a professional as well as a teacher.

Finally, I thank my family. I am so blessed to have a strong bond with my sister and brother-in-law in my life. My parents have given me support beyond measure. Thanks to their endless love, sacrifices and prayers, I could have opportunities in my life granted to few. Especially, my heart goes to my grandmother in Korea, who has been always proud of me and trusted me. I am truly indebted to my girl friend, Hyejin. Even though we have been separated physically, she has been always right next to me all along the way, being a constant inspiration to me.

TABLE OF CONTENTS

LIST OF TABLES

Page

LIST OF FIGURES

Page

LIST OF SYMBOLS

AC	alternating current
ADC	analog-to-digital converter
AFM	atomic force microscopy (microscope)
CNTs	carbon nanotubes
DAQ	data acquisition
DC	direct current
DPN	dip pen nanolithography
FDM	finite difference method
FIB	focused ion beam
FWHM	full width at half minimum
IR	infrared
MEMS	microeletromechanical systems
NEMS	nanoelectromechanical systems
NIM	negative index metamaterial
PSD	power spectrum density
SEM	scanning electron microscope (micrograph)
SOI	silicon-on-insulator
SPM	scanning probe microscopy (microscope)
SThM	scanning thermal microscopy (microscope)
TCR	temperature coefficient of resistance
tDPN	thermal dip pen nanolithography
TPV	thermophotovoltaic (thermophotovoltaics)

A	heat transfer area (m^2)
C	capacitance (H)
c	speed of light in free space, 2.998×10^8 (m/s) or specific heat (J/kg-K)
D	diffusion coefficient (m^2/s)

d	vacuum/air gap width (m)
E_g	energy bandgap (J)
$\mathbf{E}$	electric field vector (V/m)
e	electron charge, 1.602×10^{-19} (C)
$\bar{\bar{\mathbf{G}}}$	dyadic Green's function (m^{-1})
G	Green's function (m^{-1})
g	photogeneration rate of electron-hole pairs (m^{-3})
g'''	volume density of heat generation (W/m^3)
$\mathbf{H}$	magnetic field vector (A/m)
h	Planck's constant, 6.626×10^{-34} ($J\cdot s$)
h_a	heat transfer coefficient (W/m^2K)
I	electric current (A)
J	photocurrent density (A/m^2)
$\mathbf{J}$	fluctuating electric current density vector (A/m^2)
K	parallel component of wavevector (cm^{-1})
$\mathbf{k}$	wavevector (cm^{-1})
k	thermal conductivity (W/m-K)
k_B	Boltzmann's constant, 1.381×10^{-23} (J/K)
L	inductance (H)
N	carrier concentration (m^{-3})
n^0	intrinsic carrier concentration (m^{-3})
P_C	power dissipation of the cantilever (W)
P_R	radiative heat flux (W/m^2)
P_E	electric power density (W/m^2)
q''	heat flux (W/m^2)
R_{avg}	time-averaged resistance (Ω)
R	electrical resistance (Ω)
$\mathbf{S}_\omega$	time-averaged Poynting vector ($W/m^2\,\mu m$)

S	surface recombination velocity (m/s)
$s_{z,\lambda}$	wavevector-based Poynting vector in z-direction (W/m^2 μm cm^{-1})
T	temperature (K)
T_H	cantilever heater temperature (K)
T_S	substrate surface temperature (K)
T_{TH}	thermometer temperature (K)
T_∞	environment temperature (K)
V_{IN}	total input voltage (V or V-rms)
V	voltage (V or V-rms)
V_{oc}	open-circuit voltage (V)
X_C	reactance of the cantilever (Ω)
Z	electrical impedance (Ω)

Greek symbols

β	perpendicular component of the wavevector (cm^{-1})
γ	scattering rate (rad/s)
δ	cantilever or layer thickness (m)
δ_λ	penetration depth (m)
ε	relative electric permittivity
ε_0	electric permittivity of vacuum, 8.854×10^{-12} (F/m)
η	conversion efficiency
η_q	quantum efficiency
Λ	mean free path (m)
λ	wavelength in free space (μm)
μ_0	magnetic permeability of vacuum, $4\pi \times 10^{-7}$ (H/m)
Θ	temperature oscillation of the cantileve, (K)
θ_i	incidence angle (deg)
ρ	density (kg/m^3)

σ	thermal conductivity (W/m-K)
τ	relaxation time (s)
τ_s	settling time constant (s)
τ_t	thermal time constant (s)
ω	angular frequency (rad/s)

Subscripts

A	acceptor
C	cantilever
D	donor
dp	depletion region
e	electron or electric field
g	cantilever-substrate gap or bandgap
h	hole or magnetic field
i, l	index
n	*n*-region
p	*p*-region
S	sense resistor or substrate
s	source layer

SUMMARY

Recently, remarkable advances have been made in understanding micro/nanoscale thermal energy transport, opening new opportunities in manufacturing, sensing, and energy conversion at extremely small scales. Among these applications, this dissertation focuses on the characterization of a heated microcantilever for its use as a sensitive thermal metrology tool, and near-field thermophotovoltaic (TPV) energy conversion.

The first part of the dissertation seeks to understand electrical and thermal behaviors of heated microcantilevers when they are off the substrate and in contact with the substrate. Frequency-dependent electrical and thermal behaviors of heated cantilevers were empirically investigated from 10 Hz to 1 MHz, providing the optimum operation condition under periodic heating. The cantilevers were also characterized at low temperatures and in vacuum, showing the feasibility of the heated cantilever in cryogenic environments. This work further investigates the operation of heated cantilevers in an atomic force microscope (AFM) platform. Thermally-sensed topography in tapping mode was first demonstrated with a heated cantilever. As in conventional AFM, tapping mode operation allows precise topographic imaging of soft samples while suppressing imaging artifacts, providing at least two orders of magnitude higher sensitivity than piezoresistive topography. In order to better understand the thermal interaction between the heated cantilever and substrate, surface temperature was measured with a nanofabricated resistive thermometer while the heated cantilever scanned the substrate. The experiment reveals that air conduction is a dominant heat transfer mechanism with the thermal conductance in the order of 1 μW/K, which is two orders of magnitude larger than the estimated tip-substrate contact thermal conductance of around 40 nW/K.

A strong need to develop a new type of sustainable energy conversion system has motivated the second part of this dissertation. To this end, the effect of surface and bulk polariton excitations on the radiative properties of a multilayered structure was studied, suggesting that polariton excitation can be used to effectively manipulate radiative properties. The energy conversion efficiency and power throughput of a near-field TPV system was then rigorously predicted using the fluctuation-dissipation theorem and the dyadic Green's function of a multilayered structure. This study was the first that clarified the near-field effect on the quantum efficiency of a near-field TPV system. With the obtained results, a better design of near-field TPV systems is envisaged.

CHAPTER 1

INTRODUCTION

One trillion dollars per year – this is the worldwide market size of the nanotechnology-based industry in the next 10 to 15 years, projected by the US National Science Foundation [1]. Besides the industry and economy, positive impacts of nanotechnology will span to nearly every aspect of human life, for example, from healthcare to energy issues. The key to this bright future is the advances of fundamental research on the nanoscale science and engineering, and with no doubt nanoscale thermal science and engineering is one of these fundamental studies.

Originally motivated by the continuous shrinkage of microelectronic devices down to nanometer scale and following demands for effective thermal management [2], mesoscopic (from nanoscale to microscale) thermal science and engineering has been intensively studied in four directions. The first direction has been focused on theoretical understanding of thermal transport mechanisms from the microscopic point of view [3-6]. The second research direction has come along with rapid progress in the synthesis and processing of nanostructured materials, such as nanotubes, nanowires, and nanocomposites: thermal characterization of novel nanomaterials [4,7] and their applications for thermal management [4,8] and for thermoelectricity improvement [9,10] have been vivid research topics. Thirdly, enormous efforts have been made to develop the thermal metrology that has a submicron spatial resolution [11-14]. The fourth research

area is the use of the mesoscopic thermal transport for developing new nanoscale applications, such as nanoscale manufacturing [15-17] and energy conversion [18-21].

This dissertation aims at applying the micro/nanoscale thermal transport to expand nanoscale thermal metrology and energy conversion fields. To this end, the present work thermally and electrically characterizes heated microcantilevers in various conditions and environments, seeking the feasibility to use them as an accurate thermal metrology tool. Regarding the energy conversion, near-field radiation is theoretically investigated and applied to the near-field thermophotovoltaic (TPV) system. The following sections thus review the heated microcantilevers from the application perspectives and the historical background of near-field radiation research along with the development of TPV systems.

1.1 Heated Microcantilevers

1.1.1 Atomic force microscopy

Among scanning probe microscopy (SPM) families, atomic force microscopy (AFM) [22] has become perhaps the most widely used tool for sensing and/or modifying surface features with atomic-scale resolution [23]. In most common AFM configurations, the features of a surface are imaged by controlling a vertical piezoelectric stage under the substrate to keep the deflection of the cantilever (i.e., contact mode) or to keep the cantilever oscillation amplitude (i.e., tapping mode) [24,25] in a closed feedback control loop. To measure cantilever deflections, a laser is reflected off the end of the cantilever to a position-sensitive photodetector (PSD) [26,27]. Cantilever deflections can also be

detected with various sensing mechanisms such as piezoresistive sensing [28,29], capacitive sensing [30], and thermal sensing [31,32].

In addition to remarkable advances in surface morphology, the advent of AFM has also led to the growth of a wider field of cantilever-based sensing. In fact, microfabricated cantilevers have been employed for measuring and identifying various cantilever-substrate interaction forces [24,33], acceleration sensing [34], femtojoule calorimetry [35], thermogravimetry [36], vapor- and liquid-phase chemical sensing [37], biomolecular recognition [37,38], and many others. With the introduction of nanoelectromechanical system (NEMS), measurement sensitivities of cantilever-based sensors have been unprecedentedly improved, enabling zeptogram-scale mass sensing [39,40], attonewton-scale force sensing [41,42], and sub-femtometer displacement sensing [43]. Moreover, special functionalities have been incorporated into micro/nanocantilevers to further expand the cantilever-based applications. Well known examples are cantilevers having a piezoresistive strain gauge [28,40,42], cantilevers having a piezoelectric actuator [44], and cantilevers having a resistive heater [45].

1.1.2 Applications of heated microcantilevers

Silicon microcantilevers having integrated solid-state resistive heaters at the free end were originally developed for thermomechanical data storage [15,31,32,46,47], in which the cantilever is heated to make thermomechanical formation and thermal detection of small indentations in a thin polymer film. The first demonstrations of thermomechanical data storage were performed either by depositing thermal energy into the cantilever with an external heating laser [48] or by integrating a resistive heater into the cantilever leg [49]. Cantilevers having integrated heaters at the free end were

fabricated, offering heating time in the 1 μs range [45]. Moreover, parallel write/read/erase operations were made with a functional array having more than 1,000 individually-addressable heated cantilevers [15,47]. Recent research successfully fabricated an array of 64×64 (4,096) cantilevers on a 100 μm pitch, enabling extremely high data density greater than 1 Tb/in^2 [50], much higher than the superparamagnetic limit of current magnetic data storage technology near 100-200 Gb/in^2 [51].

While research on heated cantilevers has yielded much progress towards a data storage system, heated microcantilevers have also been used for other applications. A novel method was reported on selectively synthesizing carbon nanotubes (CNTs) directly onto a heated microcantilever at room temperature [52]. A typical CNT synthesis method is a thermal chemical vapor deposition which requires slow heating and cooling cycles of the entire synthesis furnace. Since this process requires high temperature to 900 °C and processing time longer than 100 min, a direct CNT synthesis on microelectromechanical system (MEMS) devices may not be possible, as they will be thermally damaged during the process. However, by heating the cantilever coated with a catalyst, CNTs could be selectively synthesized only where the local temperature is sufficiently high. After CNTs synthesis, mass of grown CNTs was measured by monitoring the change of the fundamental resonance frequency of the cantilever. The removal of the grown CNTs is also straightforward: by heating the cantilever to about 500 °C, CNTs grown on the cantilever can be removed due to the oxidization.

Heated microcantilevers can also be used for nanolithography. Particularly, a new lithography technique called thermal dip-pen nanolithography (tDPN) was proposed to further improve dip-pen nanolithography (DPN) [53,54]. DPN is a nanopatterning

technique in which a chemically coated AFM cantilever tip delivers chemical molecules from the tip to a substrate through a water meniscus, depositing features as small as 10 nm [55]. Despite the nanopatterning capability, the DPN technique has a couple of challenges to be resolved. The first challenge is that the chemical transfer cannot be controlled during the process: chemicals transfer from the tip to the substrate, or even from the substrate to the tip, whenever the tip touches the substrate [56,57]. This phenomenon also gives rise to contamination problems when more than one chemical are to be deposited with the same tip. Thermal DPN overcomes these limitations by performing DPN with a heated cantilever. In tDPN, a material coated on the cantilever tip is delivered to the substrate only when the cantilever tip is heated above the melting temperature. Material deposition is thus controllable and vacuum compatible because tDPN does not require a water meniscus. Whilst tDPN is a positive lithography, a recent research showed that a negative lithography is also possible with the heated cantilever [58]. In the experiment, they demonstrated that an energetic material (i.e., pentaerythritol tetranitrate, or PETN) was completely decomposed to make a cross mark without a pileup or residue when the heated cantilever scanned over the material with the heater temperature above a decomposition threshold temperature.

Besides nanomaterial synthesis and lithography, heated cantilevers have shown to be applicable as physical and chemical sensors. Local thermal analyses using Wollaston-wire probes have provided material properties associated with phase transitions, such as glass-transition temperature, recrystallization, and melting temperatures of polymer substrates [59-61]; the oxidative stabilization depth [62]; and the phase change enthalpy of nanogram (ng) material [63,64]. Recently, nanoscale thermal analysis has been

proposed using the heated microcantilever, in which the glass transition temperature of polystyrene was measured by monitoring a tip penetration depth into the substrate [65]. A decomposition threshold temperature of PETN was also similarly measured with a nanometer spatial resolution [58]. Berger et al. [36] used heated cantilevers as thermogravimetry, in which 420 ng of copper-sulfate-pentahydrate ($CuSO_4 \cdot 5H_2O$) is put on a heated cantilever and its mechanical resonance frequency was monitored while increasing heating to detect discrete dehydration steps. The measurement of thermal force with heated cantilevers [66] revealed that not only the magnitude but direction of the observed force depend on the temperatures of substrate and cantilever. Another cantilever-related research showed that heated cantilevers can detect the heat released by deflagration of explosive gas by monitoring its bending response during a heating pulse [67,68]: deflagration was detected at large heating pulses only after exposure to trinitrotoluene (TNT).

1.2 Near-Field Radiation

1.2.1 Near-field radiation

It is well known that the radiative energy is transferred by electromagnetic wave propagation. Electromagnetic waves near the surface consist of propagating waves and evanescent waves. The evanescent waves are localized waves that exponentially decay away from the surface within a distance comparable to its wavelength [69]. Thus, only propagating waves are responsible for the radiative energy transport when two bodies are separated far enough. In this case, the amount of radiative heat transfer can be calculated from the Stefan-Boltzmann law. However, when the distance between the two bodies

becomes comparable to or smaller than the dominant radiation wavelength, radiative energy transport is tremendously enhanced due to near-field effects such as photon tunneling and surface polaritons [5].

It was in the mid-1960's when near-field effects on the thermal radiation attracted scientists and engineers working on cryogenics. While making cryogenic thermal insulation, they found that the Stefan-Boltzmann law could not accurately predict thermal radiation within the small spacing between adjacent insulation layers [70]. Since then, many theoretical [71-73]. and experimental [74-76] studies have focused on near-field spacing effects on the thermal radiation between parallel metallic plates at cryogenic temperatures. For theoretical prediction of net radiative heat transfer between two parallel metallic plates, the complicated formalism have been established by using the electromagnetic fluctuation-dissipation theorem and dyadic Green's function, along with Drude model-based optical properties [71-73]. The electromagnetic fluctuation-dissipation theorem states that thermal emission from a solid surface is due to the fluctuating electromagnetic field produced by the random thermal motion of charged particles in the solid [77]. The implementation of the fluctuation-dissipation theorem has allowed the direct calculation of the near-field thermal radiation while the dyadic Green's function is responsible for the system geometry.

Recently, the near-field radiation in various materials and structures has been studied. Mulet et al. [78] investigated the near-field radiation between two semi-infinite polar materials that support surface waves, such as SiC or glass, demonstrating that surface waves can enhance the thermal radiation by several orders of magnitude. They also studied the radiative heat transfer between a small particle and a plane surface and

showed that the near-field radiation rate increases with $1/d^3$ for the particle-plane surface case whilst $1/d^2$ for the plane surface-plane surface case, where d is the distance [79]. Radiative heat transfer between two spheres was also examined with considering the retardation effect [80]. Fu and Zhang [81] investigated the near-field radiation between semi-infinite doped silicon plates and showed that the radiative heat flux can be more than ten times larger than the heat flux through air conduction even at atmospheric pressure.

As clarified by Mulet et al. [78], surface waves are an important factor that enhances the near-field thermal radiation. Surface waves, or surface polaritons, are localized electromagnetic fields that propagate along the interface and decay exponentially into both media due to charge density oscillation [82]. Surface waves can be surface plasmon polaritons or surface phonon polaritons depending on the charges being electrons or ion cores. For radiative energy transport, surface waves greatly enhance local density of emitted electromagnetic modes near the surface, resulting in significant change of the near-field thermal emission spectrum [83,84]. As a consequence, when surface waves are excited, the near-field spectral energy density can be several orders of magnitude greater than when there are no surface waves. If another material is placed very close to the surface, this large energy density is responsible for large radiative energy transport due to the tunneling effect.

Huge enhancement of thermal radiation in a small gap has drawn practical interests. One exemplary application is high-resolution non-contacting near-field thermal microscopy [85,86]. Another example is the near-field thermophotovoltaic (TPV) energy

conversion. More detailed discussion of near-field TPV energy conversion will be discussed at Chapter 7, and a general TPV system will be briefly reviewed here.

1.2.2 Thermophotovoltaic energy conversion

Thermophotovoltaic (TPV) devices are energy conversion systems that generate electric power directly from thermal radiation. Since the waste heat of other processes can be used as a thermal emission source, TPV systems have been considered as one of the promising methods for recycling waste heat and increasing the overall energy conversion efficiency. Increasing global concerns for reducing energy losses and preserving the environment have indeed developed a growing interest in TPV systems. The key components of a TPV device are a thermal emitter and TPV cell. The TPV cell is a *p-n* junction semiconductor that can convert the radiative photon energy to electric power, which can be realized with the photogeneration of electron-hole pairs. Since the TPV device does not have any moving parts, it guarantees silent operation. Moreover, recent research demonstrated that the power density more than 10 kW/m^3, 10 to 1,000 times higher than that of commercial batteries, can be achieved by a TPV system [87]. These advantages have made TPV systems very promising for space, military, and microelectronics applications. However, low power throughput and poor conversion efficiency have still remained as technical challenges to be overcome for the further development of TPV systems [21].

To resolve these technical challenges, many suggestions that would improve the performance of each component of the TPV system have been made. Chubb and Wolford [88] predicted that a dual layer emitter, a selective emitter consisting of two layers separated by a vacuum, can increase the emitter efficiency by nearly factor of 2 by

suppressing long wavelength emittance. Narayanaswamy and Chen [89] demonstrated one-dimensional (1-D) metallodielectric photonic crystals as a good wavelength-selective thermal emitter, whose emission spectrum can be easily tailored with the dielectric thickness. A 1-D Si/SiO_2 photonic crystal was shown to be applicable for a wavelength-selective TPV filters from 1 to 4 μm [90]. The analysis of a TPV system with stacked TPV cells revealed that the multilayered TPV cells can substantially increase the electrical power output [91].

1.3 Overview of the Dissertation

The main objective of this dissertation is two-fold: to thermally characterize the heated microcantilever with and without the presence of the substrate, through which the heated cantilever can be used in unexplored cantilever-based sensing area, and to investigate the near-fled thermal radiation in multilayered structures, through which the performance and efficiency of the near-field thermophotovoltaic energy conversion system can be investigated.

Following this introductory chapter, Chapter 2 describes the frequency-dependent electrical and thermal response of the heated microcantilever in the frequency range from 10 Hz to 1 MHz. Chapter 3 examines thermal and electrical behaviors of the heated cantilever under steady- and periodic-heating operations when it resides at cryogenic temperatures and in vacuum, seeking the feasibility of the heated cantilever in cryogenic applications as a small heating source and a thermal metrology tool. In Chapter 4, the focus moves on to the application of the heated cantilever as a topographic imaging tool. Particularly, Chapter 4 demonstrates the possibility of the thermally-sensed topography in

tapping mode. While Chapters 2 and 3 focus only on the cantilever far off the substrate, topographical imaging described in Chapter 4 strongly requires the thorough understanding of the thermal interaction between the heated cantilever and substrate. Thus, in Chapter 5 the experimental investigation of the heat transfer from the heated cantilever to the substrate using a submicron-scale resistive thermometer is described.

Chapters 6 and 7 deal with the radiative energy transport in multilayered structures. Chapter 6 describes the effects of the surface and bulk polaritons on the radiative properties in a three-layered structure. To this end, a negative index metamaterial is employed in the structure. Based on the results obtained in Chapter 6, Chapter 7 elucidates the energy transfer and energy conversion processes in near-field TPV systems. Particularly, the near-field effects on the local radiation absorption and photocurrent generation in the TPV cell are considered using the fluctuation-dissipation theorem together with a multilayer dyadic Green's function. Finally, the summary and conclusions of Chapter 8 describe possible future research and technology made possible by the work described in this dissertation.

1.4 References

[1] M. C. Roco and W. S. Baingridge, *Societal Implication of Nanoscience and Nanotechnology*: National Science Foundation, 2001.

[2] C. L. Tien and G. Chen, "Challenges in microscale conductive and radiative heat transfer," *Journal of Heat Transfer*, vol. 116, pp. 799-807, 1994.

[3] C. L. Tien, A. Majumdar, and F. M. Gerner, *Microscale Energy Transport*, Washington, D.C.: Taylor & Francis, 1998.

[4] D. G. Cahill, W. K. Ford, K. E. Goodson, G. D. Mahan, A. Majumdar, H. J. Maris, R. Merlin, and S. R. Phillpot, "Nanoscale thermal transport," *Journal of Applied Physics*, vol. 93, pp. 793-818, 2003.

[5] K. Joulain, J. P. Mulet, F. Marquier, R. Carminati, and J. J. Greffet, "Surface electromagnetic waves thermally excited: Radiative heat transfer, coherence properties and Casimir forces revisited in the near field," *Surface Science Reports*, vol. 57, pp. 59-112, 2005.

[6] G. Chen, *Nanoscale energy transport and conversion : a parallel treatment of electrons, molecules, phonons, and photons*, New York: Oxford University Press, 2005.

[7] W. Kim, R. Wang, and A. Majumdar, "Nanostructuring expands thermal limits," *Nanotoday*, vol. 2, pp. 40-47, 2007.

[8] P. K. Schelling, L. Shi, and K. E. Goodson, "Managing heat for electronics," *Materials Today*, vol. 8, pp. 30, 2005.

[9] G. Mahan, B. Sales, and J. Sharp, "Thermoelectric materials: new approaches to an old problem," *Physics Today*, vol. 50, pp. 42-47, 1997.

[10] M. S. Dresselhaus, G. Dresselhaus, X. Sun, Z. Zhang, S. B. Cronin, T. Koga, J. Y. Ying, and G. Chen, "The promise of low-dimensional thermoelectric materials," *Microscale Thermophysical Engineering*, vol. 3, pp. 89-100, 1999.

[11] A. Majumdar, "Scanning thermal microscopy," *Annual Review of Materials Science*, vol. 29, pp. 505-585, 1999.

[12] H. M. Pollock and A. Hammiche, "Micro-thermal analysis: techniques and applications," *Journal of Physics D-Applied Physics*, vol. 34, pp. R23-R53, 2001.

[13] D. G. Cahill, K. Goodson, and A. Majumdar, "Thermometry and thermal transport in micro/nanoscale solid-state devices and structures," *Journal of Heat Transfer*, vol. 124, pp. 223-241, 2002.

[14] J. Lee and N. A. Kotov, "Thermometer design at the nanoscale," *Nanotoday*, vol. 2, pp. 48-51, 2007.

[15] P. Vettiger, G. Cross, M. Despont, U. Drechsler, U. Dürig, B. Gotsmann, W. Haberle, M. A. Lantz, H. E. Rothuizen, R. Stutz, and G. K. Binnig, "The "millipede" - Nanotechnology entering data storage," *IEEE Transactions on Nanotechnology*, vol. 1, pp. 39-55, 2002.

[16] M. Geissler and Y. N. Xia, "Patterning: principles and some new developments," *Advanced Materials*, vol. 16, pp. 1249-1269, 2004.

[17] H. D. Rowland, A. C. Sun, P. R. Schunk, and W. P. King, "Impact of polymer film thickness and cavity size on polymer flow during embossing: toward process design rules for nanoimprint lithography," *Journal of Micromechanics and Microengineering*, vol. 15, pp. 2414-2425, 2005.

[18] M. S. Dresselhaus and I. L. Thomas, "Alternative energy technologies," *Nature*, vol. 414, pp. 332-337, 2001.

[19] T. F. Zeng, "Thermionic-tunneling multilayer nanostructures for power generation," *Applied Physics Letters*, vol. 88, 153104, 2006.

[20] M. Laroche, R. Carminati, and J. J. Greffet, "Near-field thermophotovoltaic energy conversion," *Journal of Applied Physics*, vol. 100, 063704, 2006.

[21] S. Basu, Y.-B. Chen, and Z. M. Zhang, "Microscale radiation in thermophotovoltaic devices - A review," *International Journal of Energy Research*, 2007 (available online, doi: 10.1002/er.1286).

[22] G. Binnig and C. F. Quate, "Atomic force microscope," *Physical Review Letters*, vol. 56, pp. 930-933, 1986.

[23] G. Binnig, C. Gerber, E. Stoll, T. R. Albrecht, and C. F. Quate, "Atomic Resolution with Atomic Force Microscope," *Europhysics Letters*, vol. 3, pp. 1281-1286, 1987.

[24] R. Garcia and R. Perez, "Dynamic atomic force microscopy methods," *Surface Science Reports*, vol. 47, pp. 197-301, 2002.

[25] F. J. Giessibl, "Advances in atomic force microscopy," *Reviews of Modern Physics*, vol. 75, pp. 949-983, 2003.

[26] G. Meyer and N. M. Amer, "Novel optical approach to Atomic force microscopy," *Applied Physics Letters*, vol. 53, pp. 1045-1047, 1988.

[27] S. Alexander, L. Hellemans, O. Marti, J. Schneir, and V. Elings, "An atomic-resolution atomic-force microscope implemented using an optical lever," *Journal of Applied Physics*, vol. 65, pp. 164-167, 1989.

[28] M. Tortonese, R. Barrett, and C. Quate, "Atomic resolution with an Atomic force microscope using piezoresistive detection," *Applied Physics Letters*, vol. 62, pp. 834-836, 1993.

[29] B. W. Chui, T. W. Kenny, H. J. Mamin, B. D. Terris, and D. Rugar, "Independent detection of vertical and lateral forces with a sidewall-implanted dual-axis piezoresistive cantilever," *Applied Physics Letters*, vol. 72, pp. 1388-1390, 1998.

[30] M. Napoli, B. Bamieh, and K. Turner, "A capacitive microcantilever: Modelling, validation, and estimation using current measurements," *Journal of Dynamic Systems, Measurement, and Control*, vol. 126, pp. 319-326, 2004.

[31] G. Binnig, M. Despont, U. Drechsler, W. Haberle, M. Lutwyche, P. Vettiger, H. J. Mamin, B. W. Chui, and T. W. Kenny, "Ultrahigh-density atomic force microscopy data storage with erase capability," *Applied Physics Letters*, vol. 74, pp. 1329-1331, 1999.

[32] W. P. King, T. W. Kenny, K. E. Goodson, G. Cross, M. Despont, U. Dürig, H. Rothuizen, G. K. Binnig, and P. Vettiger, "Atomic force microscope cantilevers for combined thermomechanical data writing and reading," *Applied Physics Letters*, vol. 78, pp. 1300-1302, 2001.

[33] Y. Sugimoto, P. Pou, M. Abe, P. Jelinek, R. Perez, S. Morita, and O. Custance, "Chemical identification of individual surface atoms by atomic force microscopy," *Nature*, vol. 446, pp. 64-67, 2007.

[34] J. Fricke and E. Obermeier, "Cantilever beam accelerometer based on surface micromachining technology," *Journal of Micromechanics and Microengineering*, vol. 3, pp. 190-192, 1993.

[35] J. R. Barnes, R. J. Stephenson, C. N. Woodburn, S. J. Oshea, M. E. Welland, T. Rayment, J. K. Gimzewski, and C. Gerber, "A femtojoule calorimeter using micromechanical sensors," *Review of Scientific Instruments*, vol. 65, pp. 3793-3798, 1994.

[36] R. Berger, H. P. Lang, C. Gerber, J. K. Gimzewski, J. H. Fabian, L. Scandella, E. Meyer, and H. J. Guntherodt, "Micromechanical thermogravimetry," *Chemical Physics Letters*, vol. 294, pp. 363-369, 1998.

[37] N. V. Lavrik, M. J. Sepaniak, and P. G. Datskos, "Cantilever transducers as a platform for chemical and biological sensors," *Review of Scientific Instruments*, vol. 75, pp. 2229-2253, 2004.

[38] X. D. Yan, H. F. Ji, and T. Thundat, "Microcantilever (MCL) biosensing," *Current Analytical Chemistry*, vol. 2, pp. 297-307, 2006.

[39] Y. T. Yang, C. Callegari, X. L. Feng, K. L. Ekinci, and M. L. Roukes, "Zeptogram-scale nanomechanical mass sensing," *Nano Letters*, vol. 6, pp. 583-586, 2006.

[40] M. Li, H. X. Tang, and M. L. Roukes, "Ultra-sensitive NEMS-based cantilevers for sensing, scanned probe and very high-frequency applications," *Nature Nanotechnology*, online available (doi:10.1038/nnano.2006.208), 2007.

[41] H. J. Mamin and D. Rugar, "Sub-attonewton force detection at millikelvin temperatures," *Applied Physics Letters*, vol. 79, pp. 3358-3360, 2001.

[42] J. L. Arlett, J. R. Maloney, B. Gudlewski, M. Muluneh, and M. L. Roukes, "Self-sensing micro- and nanocantilevers with attonewton-scale force resolution," *Nano Letters*, vol. 6, pp. 1000-1006, 2006.

[43] A. Naik, O. Buu, M. D. LaHaye, A. D. Armour, A. A. Clerk, M. P. Blencowe, and K. C. Schwab, "Cooling a nanomechanical resonator with quantum back-action," *Nature*, vol. 443, pp. 193-196, 2006.

[44] S. R. Manalis, S. C. Minne, and C. F. Quate, "Atomic force microscopy for high speed imaging using cantilevers with an integrated actuator and sensor," *Applied Physics Letters*, vol. 68, pp. 871-873, 1996.

[45] B. W. Chui, T. D. Stowe, Y. S. Ju, K. E. Goodson, T. W. Kenny, H. J. Mamin, B. D. Terris, and R. P. Ried, "Low-stiffness silicon cantilever with integrated heaters and piezoresistive sensors for high-density data storage," *Journal of Microelectromechanical Systems*, vol. 7, pp. 69-78, 1998.

[46] H. J. Mamin, B. D. Terris, L. S. Fan, S. Hoen, R. C. Barrett, and D. Rugar, "High-density data storage using proximal probe techniques," *IBM Journal of Research and Development*, vol. 39, pp. 681-699, 1995.

[47] W. P. King, T. W. Kenny, K. E. Goodson, G. L. W. Cross, M. Despont, U. T. Dürig, H. Rothuizen, G. Binnig, and P. Vettiger, "Design of atomic force microscope cantilevers for combined thermomechanical writing and thermal reading in array operation," *Journal of Microelectromechanical Systems*, vol. 11, pp. 765-774, 2002.

[48] H. J. Mamin and D. Rugar, "Thermomechanical writing with an atomic force microscope tip," *Applied Physics Letters*, vol. 61, pp. 1003-1005, 1992.

[49] H. J. Mamin, "Thermal writing using a heated atomic force microscope tip," *Applied Physics Letters*, vol. 69, pp. 433-435, 1996.

[50] M. Despont, T. Altebaeumer, P. Bächtold, G. K. Binnig, G. Cherubini, U. Drechsler, U. Dürig, E. Eleftheriou, B. Gotsmann, W. Häberle, C. Hableitner, D. Jubin, A. Knoll, M. A. Lantz, A. Pantazi, H. Pozidis, H. Rothuizen, A. Sebastian, R. Stutz, P. Vettiger, D. Wiesmann, and J. Windeln, "A highly parallel probe-

based storage system," *Digest of Papers - Microprocessor and Nanotechnology 2004*, pp. 4-5, 2004.

[51] D. A. Thompson and J. S. Best, "The future of magnetic data storage technology," *IBM Journal of Research and Development*, vol. 44, pp. 311-322, 2000.

[52] E. O. Sunden, T. L. Wright, J. Lee, S. A. Graham, and W. P. King, "Room temperature chemical vapor deposition and mass detection on a heated atomic force microscope cantilever," *Applied Physics Letters*, vol. 88, 033107, 2006.

[53] P. E. Sheehan, L. J. Whitman, W. P. King, and B. A. Nelson, "Nanoscale deposition of solid inks via thermal dip pen nanolithography," *Applied Physics Letters*, vol. 85, pp. 1589-1591, 2004.

[54] B. A. Nelson, W. P. King, A. R. Laracuente, P. E. Sheehan, and L. J. Whitman, "Direct deposition of continuous metal nanostructures by thermal dip-pen nanolithgraphy," *Applied Physics Letters*, vol. 88, 033104, 2006.

[55] R. D. Piner, J. Zhu, F. Xu, S. H. Hong, and C. A. Mirkin, "Dip-pen nanolithography," *Science*, vol. 283, pp. 661-663, 1999.

[56] M. Zhang, D. Bullen, S. W. Chung, S. Hong, K. S. Ryu, Z. F. Fan, C. A. Mirkin, and C. Liu, "A MEMS nanoplotter with high-density parallel dip-pen nanolithography probe arrays," *Nanotechnology*, vol. 13, pp. 212-217, 2002.

[57] D. Bullen, S. W. Chung, X. F. Wang, J. Zou, C. A. Mirkin, and C. Liu, "Parallel dip-pen nanolithography with arrays of individually addressable cantilevers," *Applied Physics Letters*, vol. 84, pp. 789-791, 2004.

[58] W. P. King, S. Saxena, B. A. Nelson, B. L. Weeks, and R. Pitchimani, "Nanoscale thermal analysis of an energetic material," *Nano Letters*, vol. 6, pp. 2145-2149, 2006.

[59] A. Hammiche, D. J. Hourston, H. M. Pollock, M. Reading, and M. Song, "Scanning thermal microscopy: subsurface imaging, thermal mapping of polymer blends, and localized calorimetry," *Journal of Vacuum Science & Technology B*, vol. 14, pp. 1486-1491, 1996.

[60] A. Hammiche, L. Bozec, M. Conroy, H. M. Pollock, G. Mills, J. M. R. Weaver, D. M. Price, M. Reading, D. J. Hourston, and M. Song, "Highly localized thermal, mechanical, and spectroscopic characterization of polymers using miniaturized thermal probes," *Journal of Vacuum Science & Technology B*, vol. 18, pp. 1322-1332, 2000.

[61] D. S. Fryer, P. F. Nealey, and J. J. de Pablo, "Thermal probe measurements of the glass transition temperature for ultrathin polymer films as a function of thickness," *Macromolecules*, vol. 33, pp. 6439-6447, 2000.

[62] C. Blanco, S. Lu, S. P. Appleyard, and B. Rand, "The stabilisation of carbon fibres studied by micro-thermal analysis," *Carbon*, vol. 41, pp. 165-171, 2003.

[63] R. Berger, C. Gerber, J. K. Gimzewski, E. Meyer, and H. J. Guntherodt, "Thermal analysis using a micromechanical calorimeter," *Applied Physics Letters*, vol. 69, pp. 40-42, 1996.

[64] Y. Nakagawa, R. Schafer, and H. J. Guntherodt, "Picojoule and submillisecond calorimetry with micromechanical probes," *Applied Physics Letters*, vol. 73, pp. 2296-2298, 1998.

[65] B. A. Nelson and W. P. King, "Measuring material softening with nanoscale spatial resoultion using heated silicon probes," *Review of Scientific Instruments*, vol. 78, 023702, 2007.

[66] B. Gotsmann and U. Dürig, "Experimental observation of attractive and repulsive thermal forces on microcantilevers," *Applied Physics Letters*, vol. 87, 194102, 2005.

[67] L. A. Pinnaduwage, A. Gehl, D. L. Hedden, G. Muralidharan, T. Thundat, R. T. Lareau, T. Sulchek, L. Manning, B. Rogers, M. Jones, and J. D. Adams, "A microsensor for trinitrotoluene vapour," *Nature*, vol. 425, pp. 474-474, 2003.

[68] L. A. Pinnaduwage, A. Wig, D. L. Hedden, A. Gehl, D. Yi, T. Thundat, and R. T. Lareau, "Detection of trinitrotoluene via deflagration on a microcantilever," *Journal of Applied Physics*, vol. 95, pp. 5871-5875, 2004.

[69] M. Born, E. Wolf, and A. B. Bhatia, *Principles of Optics: Electromagnetic Theory of Propagation, Interference and Diffraction of Light*, 7th ed., New York: Cambridge University Press, 1999.

[70] C. L. Tien and G. R. Cunnington, "Recent advances in high-performance cryogenic thermal insulation," *Cryogenics*, vol. 12, pp. 419-421, 1972.

[71] D. Polder and M. Vanhove, "Theory of radiative heat transfer between closely spaced bodies," *Physical Review B*, vol. 4, pp. 3303-3314, 1971.

[72] R. P. Caren, "Thermal-radiation between closely spaced metal-surfaces at low-temperature due to travelling and quasi-stationary components of radiation field," *International Journal of Heat and Mass Transfer*, vol. 17, pp. 755-765, 1974.

[73] J. J. Loomis and H. J. Maris, "Theory of heat transfer by evanescent electromagnetic waves," *Physical Review B*, vol. 50, pp. 18517-18524, 1994.

[74] E. G. Cravalho, G. A. Domoto, and C. L. Tien, "Measurements of thermal radiation of solids at liquid helium temperatures," in *Progress in Aeronautics and Astronautics*, vol. 21, J. T. Debans, Ed., 1968, pp. 531-542.

[75] G. A. Domoto, R. F. Boehm, and C. L. Tien, "Experimental Investigation of Radiative Transfer between Metallic Surfaces at Cryogenic Temperatures," *Journal of Heat Transfer*, vol. 92, pp. 412-417, 1970.

[76] C. M. Hargreaves, "Radiative-transfer between closely spaced bodies," *Philips Research Reports Supplements*, vol. 5, pp. 1-80, 1973.

[77] S. M. Rytov, Y. A. Kravtsov, and V. I. Tatarskii, *Principles of Statistical Radiophysics*, vol. 4, Berlin: Springer-Verlag, 1989.

[78] J. P. Mulet, K. Joulain, R. Carminati, and J. J. Greffet, "Enhanced radiative heat transfer at nanometric distances," *Microscale Thermophysical Engineering*, vol. 6, pp. 209-222, 2002.

[79] J. P. Mulet, K. Joulain, R. Carminati, and J. J. Greffet, "Nanoscale radiative heat transfer between a small particle and a plane surface," *Applied Physics Letters*, vol. 78, pp. 2931-2933, 2001.

[80] A. I. Volokitin and B. N. J. Persson, "Radiative heat transfer between nanostructures," *Physical Review B*, vol. 6320, 205404, 2001.

[81] C. J. Fu and Z. M. Zhang, "Nanoscale radiation heat transfer for silicon at different doping levels," *International Journal of Heat and Mass Transfer*, vol. 49, pp. 1703-1718, 2006.

[82] H. Raether, *Surface Plasmons on Smooth and Rough Surfaces and on Gratings*, Berlin ; New York: Springer-Verlag, 1988.

[83] K. Joulain, R. Carminati, J. P. Mulet, and J. J. Greffet, "Definition and measurement of the local density of electromagnetic states close to an interface," *Physical Review B*, vol. 68, 245405, 2003.

[84] A. V. Shchegrov, K. Joulain, R. Carminati, and J. J. Greffet, "Near-field spectral effects due to electromagnetic surface excitations," *Physical Review Letters*, vol. 85, pp. 1548-1551, 2000.

[85] C. C. Williams and H. K. Wickramasinghe, "Scanning thermal profiler," *Applied Physics Letters*, vol. 49, pp. 1587-1589, 1986.

[86] W. Muller-Hirsch, A. Kraft, M. T. Hirsch, J. Parisi, and A. Kittel, "Heat transfer in ultrahigh vacuum scanning thermal microscopy," *Journal of Vacuum Science & Technology A*, vol. 17, pp. 1205-1210, 1999.

[87] T. J. Coutts, "A review of progress in thermophotovoltaic generation of electricity," *Renewable and Sustainable Energy Reviews*, vol. 3, pp. 77-184, 1999.

[88] D. L. Chubb and D. S. Wolford, "Dual layer selective emitter," *Applied Physics Letters*, vol. 87, 141907, 2005.

[89] A. Narayanaswamy and G. Chen, "Thermal emission control with one-dimensional metallodielectric photonic crystals," *Physical Review B*, vol. 70, 125101, 2004.

[90] F. O'Sullivan, I. Celanovic, N. Jovanovic, J. Kassakian, S. Akiyama, and K. Wada, "Optical characteristics of one-dimensional Si/SiO_2 photonic crystals for thermophotovoltaic applications," *Journal of Applied Physics*, vol. 97, 033529, 2005.

[91] L. Z. Shi and R. F. Boehm, "Performance of multilayered thermophotovoltaic elements at moderate temperature," *Journal of Thermophysics and Heat Transfer*, vol. 15, pp. 458-462, 2001.

CHAPTER 2

FREQUENCY-DEPENDENT ELECTRICAL AND THERMAL RESPONSES OF A HEATED MICROCANTILEVER

This chapter describes the electrical and thermal response of the heated microcantilevers in the frequency range from 10 Hz to 1 MHz. Spectrum analysis of the cantilever voltage response to periodic heating distinguishes different thermal behaviors of the cantilever in the frequency domain: the cantilever voltage at low frequencies is modulated by higher order harmonics, and at high frequencies, it oscillates with 1ω only. A simple model facilitates the understanding of complicated electrical and thermal behaviors in the cantilever, thus it is possible to determine the cantilever temperature. The calculation predicts that temperature oscillation is restricted to the heater region when the cantilever is operated at about 10 kHz, suggesting that the periodic-heating operation of the cantilever may be employed for highly sensitive thermal metrology.

2.1 Introduction

The atomic force microscope (AFM) has become an important tool for probing physical, chemical, and electromagnetic phenomena in domains of size from 1 nm to 100 μm. Silicon AFM cantilevers having resistive heaters integrated near the cantilever tip were originally developed for thermomechanical data storage but have also been shown to be useful for nanoscale manufacturing and metrology, as already reviewed in Chapter 1. To date, heated cantilevers have been characterized and operated either at steady-state

or with short electrical pulses, as would be appropriate for interfacing with digital control electronics. However, operating heated cantilevers with oscillatory heating could enable new measurement techniques and applications. To this end, this work analyzes the frequency-dependent electrical and thermal behavior of heated AFM cantilevers for driving frequency in the range of 10 Hz to 1 MHz.

Periodic-heating operation of the cantilever could facilitate the development of scientific measurements that would not be feasible with the steady-state cantilever operation, because various noise sources including 1/f noise and electronic noise in the cantilever can be reduced [1]. Frequency-modulated measurements have been studied in various AFM cantilever-based metrologies to enhance measurement sensitivity; for example: thermogravimetry [2], noncontact surface imaging [3], scanning thermal microscopy [4], scanning near-field thermal microscopy [5], and scanning near-field ultrasound holography [6]. While one previously published report [7] investigated frequency response of a heated microcantilever, it used a simple resistor-capacitor network to find the thermal time constant of the cantilever and did not investigate oscillatory temperature or periodic heat flow in the cantilever. There remains lack of understanding of the heated microcantilever behavior during periodic-heating operation, which prevents a number of possible uses of the heated cantilever for nano/microscale measurement.

Highly accurate measurements of the cantilever thermal responses under periodic excitation are complicated by several coupled physical phenomena. First, the temperature-dependent cantilever resistance is nonlinear, which significantly affects the way the cantilever resistance oscillates with the periodic heater temperature. This

nonlinearity has been a main issue in previous work on steady-state cantilever heating [8-10]. The thermal diffusion length of the cantilever also complicates the analysis of the cantilever frequency response, as the diffusion length depends on excitation frequency. At high frequencies, the diffusion length may be shorter than the cantilever length, giving rise to temperature oscillations restricted to only part of the cantilever. Finally, the intrinsic electrical impedance of the cantilever is also frequency-dependent, and can compete with the actual cantilever sensor signal. A thorough analysis should account for all of these coupled effects.

This work investigates the electrical and thermal responses of heated microcantilevers under the periodic heating in the range of 10 Hz to 1 MHz. Steady-state thermal characterization is first described, followed by the discussion of thermal characterization under periodic heating. Spectrum analysis of the heated cantilever voltage illustrates four different operating regions that are distinguished by the number of harmonic signals generated. The electrical resistance oscillation and the reactance of the cantilever are extracted from measured data. A simple model simulates the thermal response of the heated cantilever to predict the cantilever temperature oscillation, which cannot be directly obtained through experiment.

2.2 Experiment

The experiment used heated microcantilevers made from a silicon-on-insulator (SOI) wafer [11,12]. Figure 2.1(a) shows the scanning electron microscope (SEM) image of the cantilever used in the experiment. The cantilever is u-shaped, having the heater integrated at the free end. The tip is fabricated at the center of the heater region with the

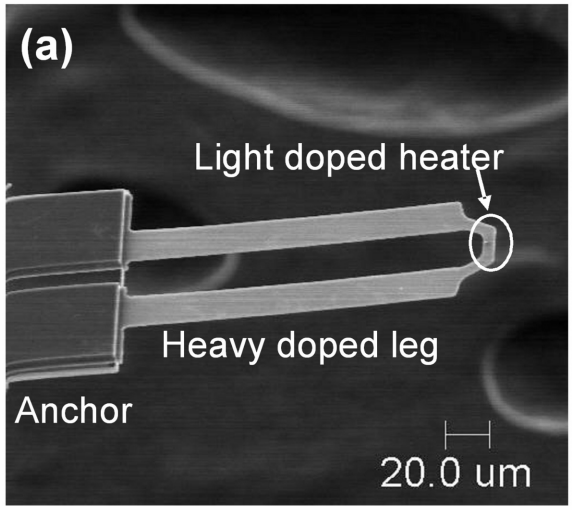

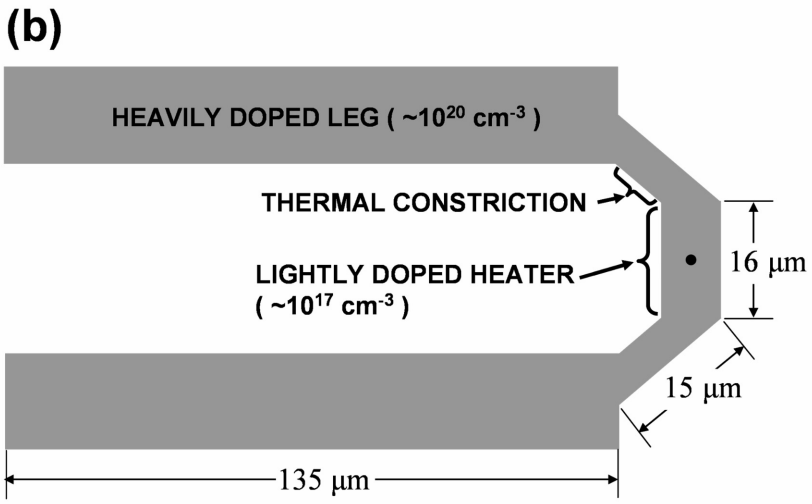

Figure 2.1 The image of a heated AFM cantilever. (a) A SEM micrograph of a cantilever chip and (b) a drawing of the cantilever part.

height of around 500 nm and tip radius of 20 to 50 nm. The cantilever thickness is designed to be around 1 μm, but may slightly change depending on the etching condition. As shown in Fig. 2.1(b), the cantilever consists of three regions: heater, leg, and thermal constriction. The heater region is highly resistive region of 8 μm × 16 μm that is realized with light phosphorus doping of around 10^{17} cm^{-3}. The leg region, whose length and width are respectively 135 μm and 15 μm, is heavily phosphorus-doped to around 10^{20} cm^{-3} for electrical leads. The thermal constriction, which has 5 μm in width and 15 μm in length, improves the cantilever heating and cooling efficiency [7]. The electrical resistance of cantilevers is typically 1 to 3 kΩ, with around 90 % of the resistance being from the heater region. When the electrical current flows through the cantilever, the heater region predominantly dissipates the electrical power, resulting in temperature rise over 1,000 K [12]. The anchor that connects the base silicon and the cantilever creates the buffer zone that mitigates any inconsistency of the backside etching process and allows for improved laser access when mounted on a commercial AFM system.

In steady-state operation, or DC mode operation, the thermal behavior of a heated AFM cantilever can be characterized by measuring its temperature-dependent electrical resistance. The cantilever is usually operated in a simple bridge structure, in series with a second bridge resistor (i.e., a sense resistor), to protect the cantilever from high input voltage and enhance the resolution of the cantilever power increment. A 10 kΩ carbon film resistor was used as the sense resistor in the present study. By measuring the current and the voltage drop across the sense resistor while varying the total input voltage, the cantilever resistance can be obtained. As illustrated in Fig. 2.2(a), the characterization of the cantilever in periodic heating operation, or AC mode operation, follows a similar

procedure as DC mode, but more instruments are required to capture the complex cantilever response. A periodic voltage source drives the circuit consisting of the cantilever and the sense resistor. An amplifier increases the dynamic range of the input voltage. Total input voltage V_A and voltage drop across the sense resistor V_B were measured with a digital oscilloscope to obtain the cantilever voltage, $V_C(t) = V_A - V_B$. A spectrum analyzer measured the magnitude and the phase of the cantilever voltage signal. The current $I(t)$ was obtained from V_B and the sense resistance.

The sense resistor value changes with frequency due to the parasitic inductance and device capacitance [13], and thus the impedance effect of the sense resistor was considered for accurate evaluation of the current. Figure 2.2(b) shows the impedance of the sense resistor measured with a Solartron SI 1260 impedance/gain-phase analyzer. The impedance effect of the sense resistor can be ignored up to 100 kHz. Above 100 kHz, however, the decreasing sense resistance will significantly affect the cantilever operation, which will be discussed later. The equivalent circuit in the inset of Fig. 2(b) accounts for the electric behavior of the sense resistor:

$$Z_S = \frac{R_S(1-\omega^2 L_S C_S) + j\omega L_S R_S}{1 + j\omega C_S R_S} \tag{2.1}$$

The sense capacitance and inductance was estimated to be 3.09 pF and 47.3 μH. The modeled impedance describes the measurement within 0.2 % standard error up to 5 MHz. The current is thus calculated by $I(t) = \mathrm{Re}[V_B / Z_S]$, where Re denotes the real part of a complex number.

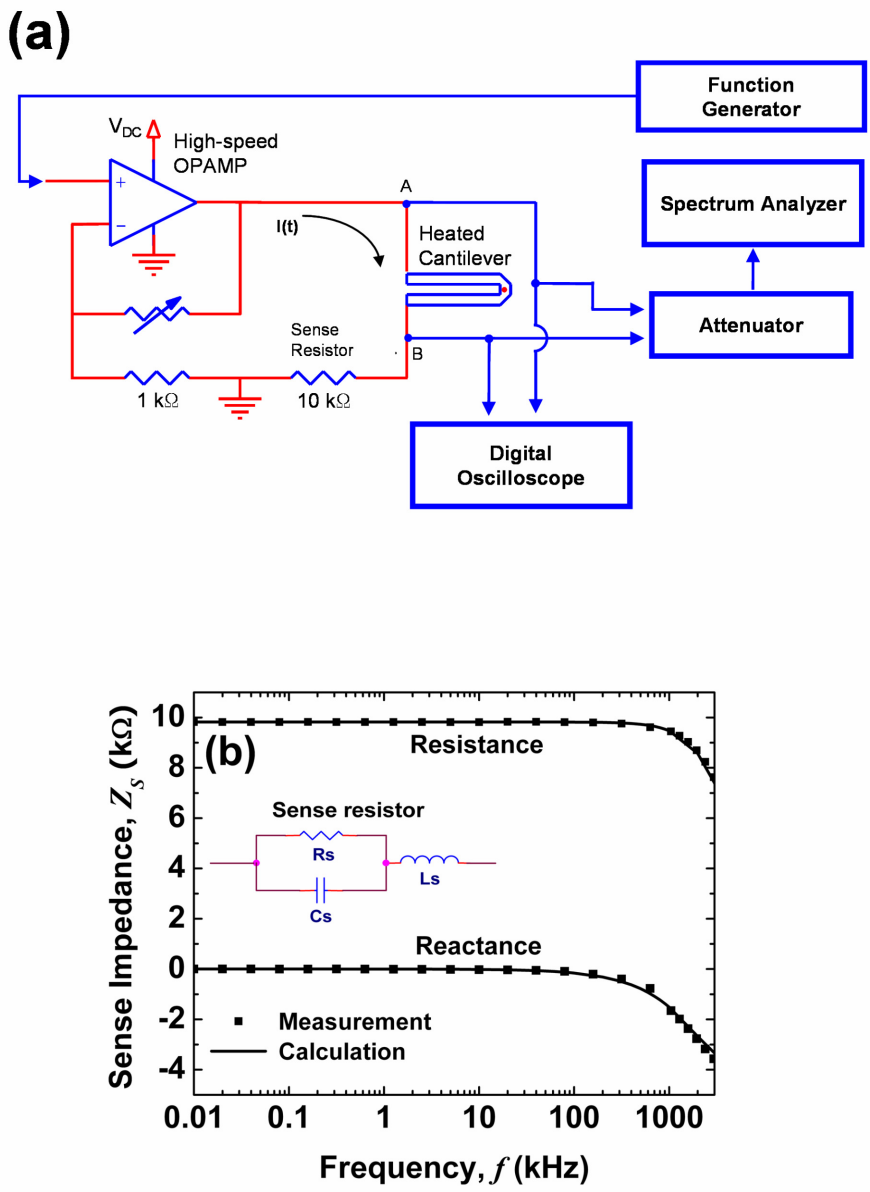

Figure 2.2 The experimental description for the AC characterization of the heated cantilever. (a) The schematic diagram describing the AC characterization experiment. DC characterization can also be performed with this setup if a DC power supply is used instead of the function generator. (b) The measured and modeled impedance of the sense resistor in the frequency domain that is used to determine the current out of the voltage drop across the sense resistor.

The steady temperature at the heater region was measured using a Raman spectroscope with a spatial resolution near 1 μm [12,14,15]. Raman spectroscopy is an optical technique that measures inelastic scattering of light from materials. Since the inelastic light scattering frequency changes with temperature, measuring the light scattering patterns will provide the local temperature of the material . However, Raman spectroscopy typically requires a long exposure time (i.e., 30 - 60 s), thus it cannot measure temperature oscillation. Since the hottest temperature at the heater region was of interest, only the center of the heater region was measured in the experiment and taken as the heater temperature. The Raman spectroscope was calibrated for phosphorus-doped silicon that closely resembled the cantilever material, yielding uncertainties of ±2.1 K for 300 to 500 K, ±3.7 K for 500 to 800 K, ±5.4 K for 800 to 1000 K, and ±7.6 K for 1000 to 1300 K [15].

2.3 Electrical and Thermal Characterization

2.3.1 Spectrum analysis

The cantilever was first characterized in DC mode in order to establish a baseline response. Figure 2.3(a) shows the cantilever resistance as a function of the cantilever heater temperature. The cantilever resistance increases with temperature up to around 900 K and then decreases, indicating that the temperature coefficient of resistance (TCR) is a function of temperature and becomes negative above 900 K. Figure 2.3(b) also shows the nonlinearity of the cantilever resistance with the total input voltage. The estimated uncertainties of the cantilever resistance and the cantilever power are respectively

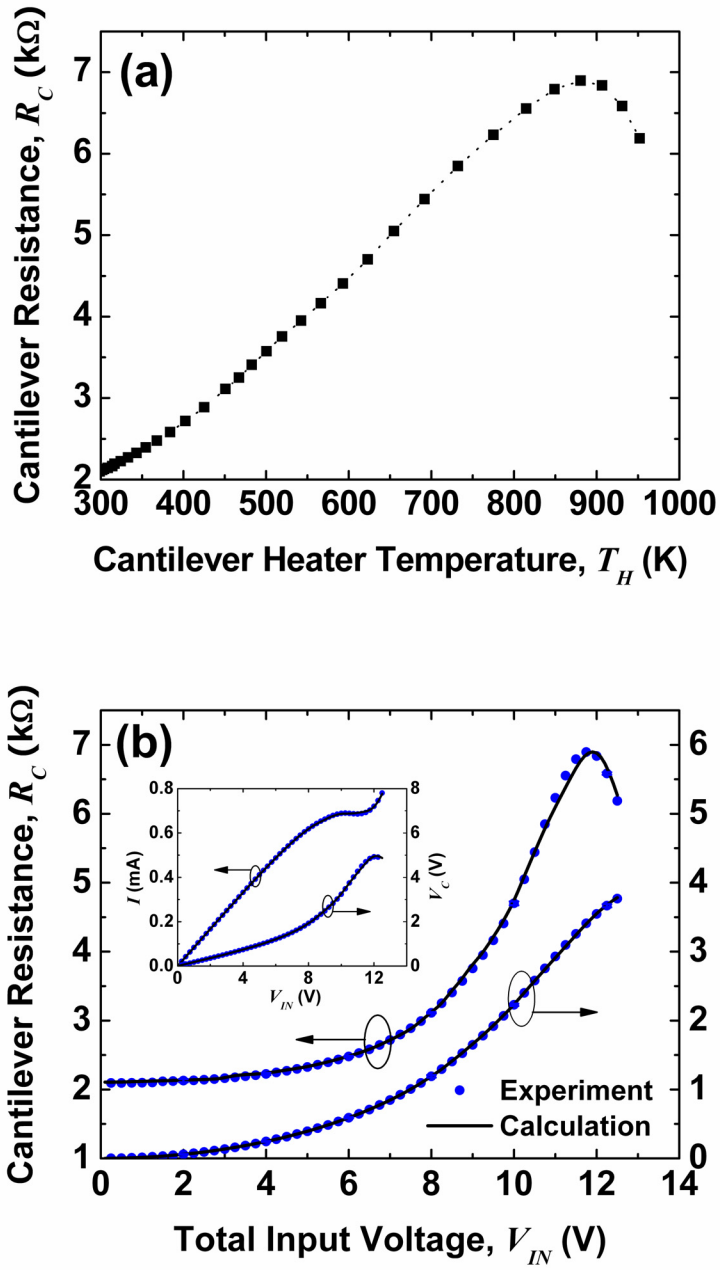

Figure 2.3 DC response of a heated cantilever. (a) The cantilever resistance and the cantilever heater temperature measured with a Raman spectroscope. (b) The cantilever resistance and the cantilever power as a function of the total input voltage. In the inset, the current and cantilever voltage plotted against the total input voltage. The solid curves are numerical modeling results that are discussed in Section 2.4.

± 0.6 % and ± 0.7 %. The solid curves are numerical modeling results to be discussed later. As shown in the inset of Fig. 2.3(b), sharp increase of the cantilever resistance around the input voltage of 10 V is accompanied with sharp increase of the cantilever voltage and a plateau of the current. The negative cantilever TCR above 12 V reduces the cantilever resistance and increases the current as the input voltage further increases. More power is thus dissipated in the cantilever, leading to further decrease of the resistance. This feedback cycle causes the temperature of the heater region to rise suddenly: that is, "thermal runaway" occurs within the heater region [9,12].

Under the AC operation, periodic heating of the cantilever is coupled with the periodic electrical signal, giving rise to the harmonic cantilever voltage. When periodic excitation voltage with the frequency ω is applied to a heated cantilever, the power dissipation will oscillate at frequency 2ω, causing fluctuations of temperature as well as electrical resistance at 2ω. Combined with the current oscillation at ω, this resistance oscillation modulates the cantilever voltage to yield the 3ω harmonic signal. Since this third harmonic is thermally generated, its magnitude depends on the AC temperature rise and cantilever thermophysical properties. The so-called "3ω method" [16] has been used to measure thermophysical properties such as the thermal conductivity and the specific heat in various materials and structures [17-19].

The magnitude of the 3ω signal depends on the AC power input and the driving frequency, and may generate higher odd harmonics in combination with the even harmonics of the cantilever resistance. Figure 2.4(a) shows the frequency-dependence of the odd harmonics across the cantilever for the total input voltage 7 V-rms. The 1ω signal is plotted with $\text{dBV-rms} = 20\log_{10}(V_{\omega,rms})$, and higher harmonics are with

$\mathrm{dB} = 20\log_{10}(V_{n\omega,rms}/V_{\omega,rms})$, where $n = 3,5,7,\cdots$ denotes the higher odd harmonics. The *y*-axis label starts from -40 dB, indicating that the smallest meaningful signal is 1 % of the 1ω signal. No harmonic signals change their magnitudes until the frequency increases above 100 Hz, suggesting that the cantilever maintains thermal equilibrium with its environment during the operation. As the frequency further increases, the 3ω and 5ω signals decrease. Finally, there is a frequency region above about 30 kHz where only the 1ω signal is important. In this region, the cantilever heater temperature does not oscillate with time, because the power oscillates too fast for the cantilever to thermally respond. A total input voltage other than 7 V-rms would yield different harmonic curves although the trends in harmonic curves will be similar.

With a fixed cantilever excitation frequency of 100 Hz, Fig. 2.4(b) shows measured harmonic signals as a function of total input voltage. The 3ω signal emerges at 3 V-rms and drastically increases by 10 times from –40 dB to –20 dB as total input voltage increases from 3 V-rms to 6 V-rms. The 3ω signal then starts decreasing after around 8.5 V-rms. This nonlinear behavior of the 3ω signal is attributed to the nonlinearity of cantilever resistance, shown in Fig. 2.3(b). The nonlinear cantilever resistance is also responsible for the generation of the higher harmonics. Due to its nonlinearity, the cantilever resistance cannot be first-order approximated with the temperature change. The cantilever resistance can be expressed as

$$R \approx R_0 + \left.\frac{dR}{dT}\right|_{T_0} \Delta T + \frac{1}{2}\left.\frac{d^2R}{dT^2}\right|_{T_0} \Delta T^2 + \cdots \tag{2.2}$$

Since ΔT oscillates with 2ω, the higher cantilever voltage harmonics are due to the presence of the higher-order terms in Eq. (2.2). Moreover, the second and third terms,

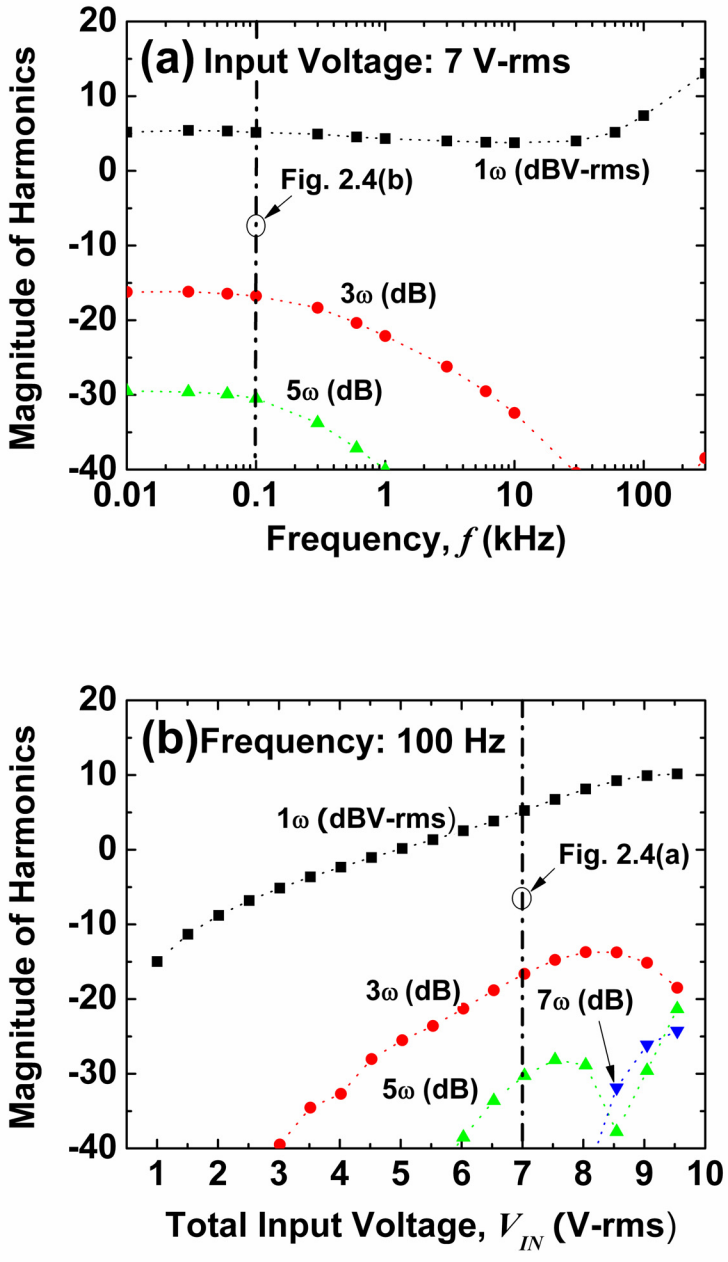

Figure 2.4 Spectrum analysis results of the voltage drop across the cantilever (a) when the frequency sweeps at the fixed total input voltage 7 V-rms and (b) when the total input voltage sweeps at the fixed frequency 100 Hz. Note that the unit of 1ω signal is dBV-rms while those of higher harmonics are dB to the magnitude of 1ω signal.

each of which is associated to the 3ω and 5ω harmonic signals, are related with each other by a derivative with respect to temperature. When T_0 becomes the thermal runaway temperature, the 5ω signal experiences a sharp decrease because the 3ω signal has an extremum at that point, as shown in Fig. 2.4(b). The emerging 7ω and 9ω signals can be explained similarly. The 9ω signal is not included in the plot for clarity since it almost overlaps with the 7ω signal. Thermal runaway can be thus determined with a sharp decrease of the 5ω signal and the appearance of the higher harmonics.

In order to accurately describe the thermal behavior of the cantilever, higher order harmonic signals should be considered depending on the input voltage and the frequency.

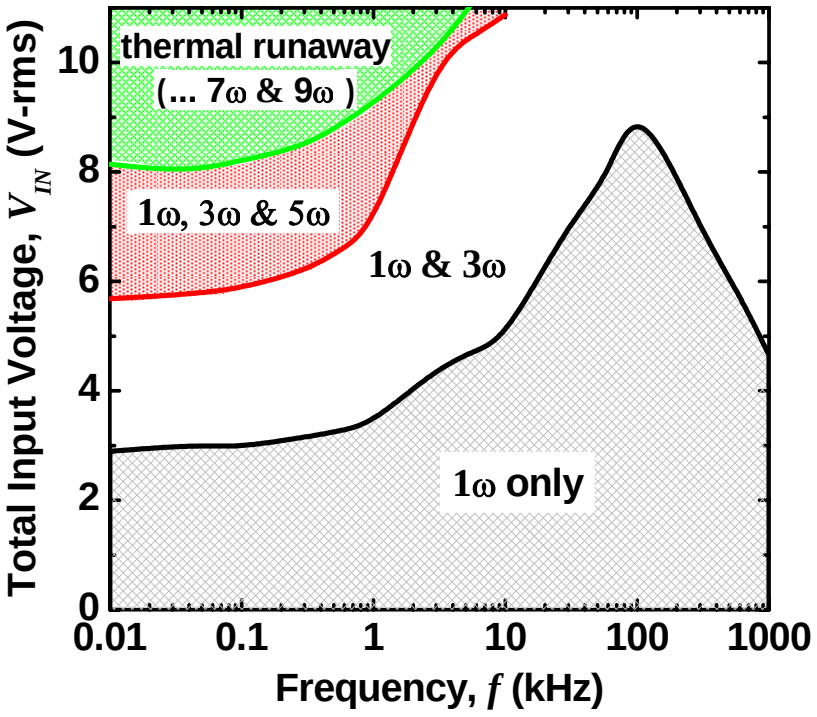

Figure 2.5 A regime map delineating the AC response of the cantilever. The boundaries of regimes are obtained from the spectral analysis when a cutoff ratio is set to -40 dB. In the low frequency region, higher harmonic terms become important as more power is dissipated on the cantilever. In high frequency region, on the other hand, only 1ω and 3ω signals are shown.

Figure 2.5 shows a frequency domain regime map, distinguishing four regions of different harmonic signals. The regime map was obtained by repeating the procedure that produced Fig. 2.4(b) for different frequencies and achieving boundaries at which emerging higher harmonics become larger than –40 dB. For frequencies lower than 10 kHz, increasing AC power input yields higher odd harmonic cantilever voltage signals. At frequencies higher than 10 kHz, only 1ω and 3ω signals exist, indicating that the cantilever temperature oscillation amplitude is small. The descending upper boundary of the 1ω region above 100 kHz is the combination of the cantilever characteristics and the impedance effect of the sense resistance. As shown in Fig. 2.2, the sense resistance starts decreasing at around 100 kHz, concentrating more power on the cantilever and, correspondingly, causing more temperature rise compared to the low frequency operation.

The different regions of Fig. 2.5 can be better understood by examining the cantilever voltage and current traces for each region. Figure 2.6 shows the oscilloscope traces of the cantilever voltage and current at each region of the regime map when the frequency is 100 Hz. The voltage and current signals become increasingly modulated as the input voltage increases. In particular, both the voltage and current traces at 9 V-rms have secondary valleys and hills at poles, which are associated with higher harmonic signals at the thermal runaway. The I-V curves in Fig. 2.6(c) provide a clear view that the cantilever resistance, which appears linear when the input voltage is low, becomes nonlinear at higher input voltages. All I-V curves intersect with the origin, indicating that the electric power is totally dissipated by Joule heating. The insets of Fig. 2.6(a) and (c)

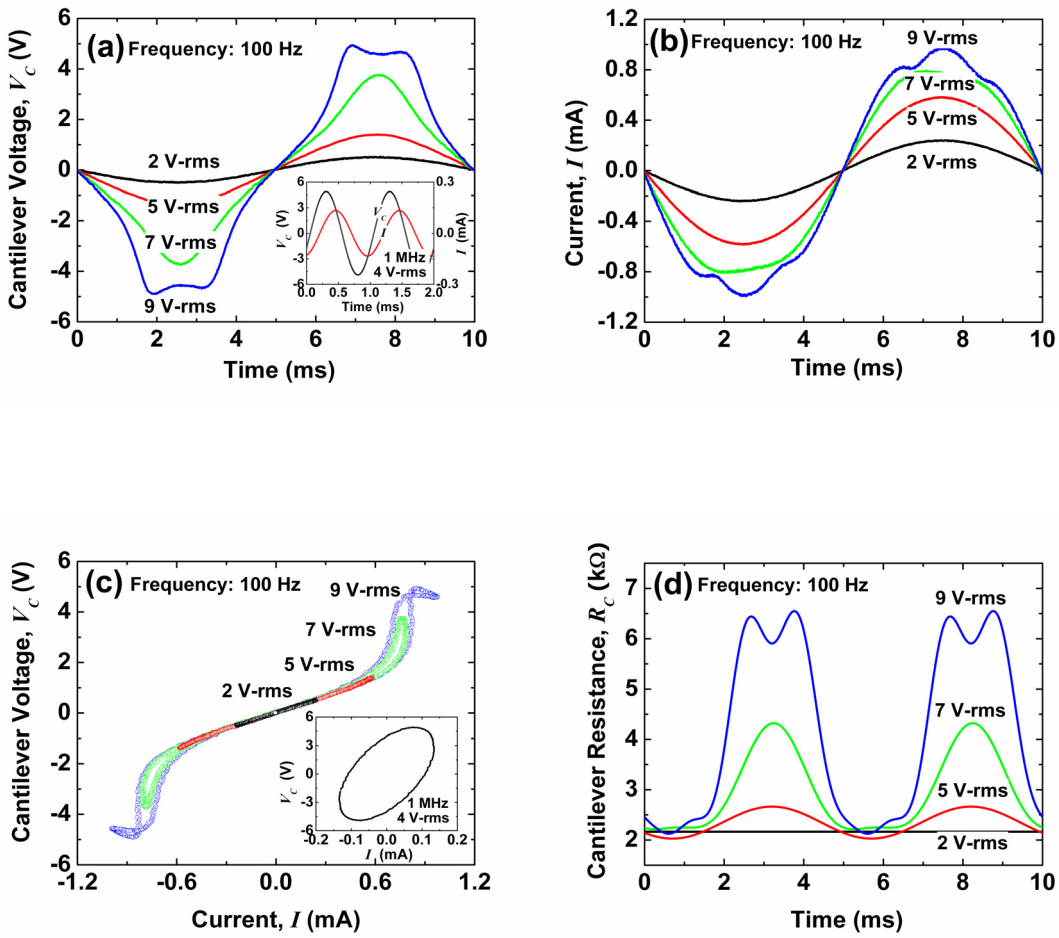

Figure 2.6 The cantilever voltage and current relationship at the low and high frequency regions. (a) Oscilloscope traces of the cantilever voltage and (b) the current for different total input voltages at 100 Hz. (c) The I-V curves that clearly illustrate the nonlinear relations between the cantilever voltage and the current at high input voltages. The insets in (a) and (c) shows oscilloscope traces of the cantilever voltage and the current at 1 MHz, indicating that the electrical impedance causes a considerable phase difference between the cantilever voltage and the current at the high frequency region. (d) The time-dependent cantilever resistances are extracted from (a) and (b).

show the cantilever voltage and current, respectively, when the cantilever is operated at 4 V-rms and 1 MHz. The main difference from the low frequency region is the phase difference between the voltage and current, suggesting that the impedance plays an important role in the high frequency response. The cantilever resistance can be obtained from I-V relations, detailed discussions on which are in the following section.

2.3.2 Cantilever resistance and reactance

Since the cantilever resistance is directly related with the cantilever temperature, calculation of the cantilever resistance from the measured cantilever voltage and current will provide valuable information on the cantilever thermal behavior. However, the oscillating cantilever resistance during AC operation complicates the calculation and requires a complex number approach. The voltage drop across the cantilever can be expressed as

$$V_C(t) = \sum_{i=1,3,5\cdots} V_i \cos(i\omega t + \phi_i) \tag{2.3}$$

where $\omega = 2\pi f$ is the angular frequency, and V_i and ϕ_i are the magnitude and phase of the *i*-th harmonic, respectively. Similarly, the current is

$$I(t) = \sum_{i=1,3,5\cdots} I_i \cos(i\omega t + \psi_i) \tag{2.4}$$

where I_i and ψ_i are the magnitude and phase of the *i*-th harmonic. All of the magnitudes and phases of harmonic components are experimentally obtained from the spectrum analysis. Since the cantilever is an ohmic conductor in the low frequency region, the cantilever resistance $R_C(t)$ can be obtained by applying Ohm's law, $V_C(t) = I(t)R_C(t)$. The cantilever resistance can be written as

$$R_C(t) = R_{avg} + \sum_{l=2,4,6\cdots} R_l \cos(l\omega t + \varphi_l) \tag{2.5}$$

following the power oscillation that contains only even harmonic terms. Here, R_{avg} is the time-averaged resistance obtained from $R_{avg} = (1/T)\int_0^T R(t)dt$. The heating power is the product of the cantilever voltage and current, i.e., $I(t)V_C(t)$, and contains only even harmonic terms. In Eq. (2.5), R_{avg} is the time-averaged resistance, R_l the amplitude of the resistance oscillation corresponding to the *l*-th harmonic, and φ_l the phase of the *l*-th harmonic. Substituting Eqs. (2.3), (2.4), and (2.5) into Ohm's law and performing complex number analysis provide the cantilever resistance. As discussed in the previous section, cantilever voltage and current signals at frequencies higher than 30 kHz have only the 1ω harmonic with a phase difference. Thus, only the first terms of Eqs. (2.3) and (2.4) are taken into account, and the cantilever impedance can be simply calculated using the phasor analysis [20]. The cantilever voltage and current are expressed as $V_C = V_\omega e^{j\phi_\omega}$ and $I = I_\omega e^{j\psi_\omega}$, so that the impedance is calculated by

$$Z_C = R_C + jX_C = \frac{V_\omega}{I_\omega}\left[\cos(\phi_\omega - \psi_\omega) + j\sin(\phi_\omega - \psi_\omega)\right] \tag{2.6}$$

where R_C and X_C represent the resistance and reactance of the cantilever, respectively.

Figure 2.6(d) shows the cantilever resistance at 100 Hz. When the input voltage is 2 V-rms, the resistance is essentially constant because the small amount of heating causes little change in the cantilever heater temperature. When the input voltage becomes 5 V-rms, however, the resistance oscillates with time. The oscillation amplitude of the cantilever resistance becomes larger as the input voltage increases. The resistance

oscillation at 9 V-rms shows small valleys on top of the resistance trace. From comparison with the DC resistance curve in Fig. 2.3(b), it is clear that the small valleys emerge due to the thermal runaway. The resemblance of the resistance trace with the DC thermal characterization also indicates that the resistance of the cantilever fully follows the oscillation of the electrical power at low frequencies. This is because the power oscillation frequency is slow enough for the cantilever to achieve a thermal equilibrium with the environment [7].

As can be seen in Fig. 2.6(d), both the peak-to-peak amplitude of the cantilever resistance oscillation, R_{pp}, and the time-averaged resistance, R_{avg}, increase with the total input voltage. These two values will also change with the frequency. Figure 2.7(a) shows R_{pp} for different frequencies as a function of the total input voltage. R_{pp} increases with the total input voltage. However, overall value of R_{pp} decreases with the frequency because thermal response time of the cantilever is not as fast as the power oscillation. Note that R_{pp} becomes constant once it reaches the maximum, because the cantilever reaches the peak resistance and experiences thermal runaway. Since R_{pp} decreases with increasing frequency, R_{avg} asymptotically approaches the DC cantilever resistance, shown in Fig. 2.7(b). However, for frequencies higher than 30 kHz, the cantilever resistance drastically deviates from the DC response, as the cantilever impedance begins to compete with the temperature-dependent cantilever resistance. Figure 2.7(c) shows that the cantilever reactance increases with both frequency and input voltage. Note that both the resistance and reactance at 300 kHz suddenly drop when the input voltage becomes 7 V-rms. When compared with the regime map in Fig. 2.5, this drop occurs when the cantilever operation

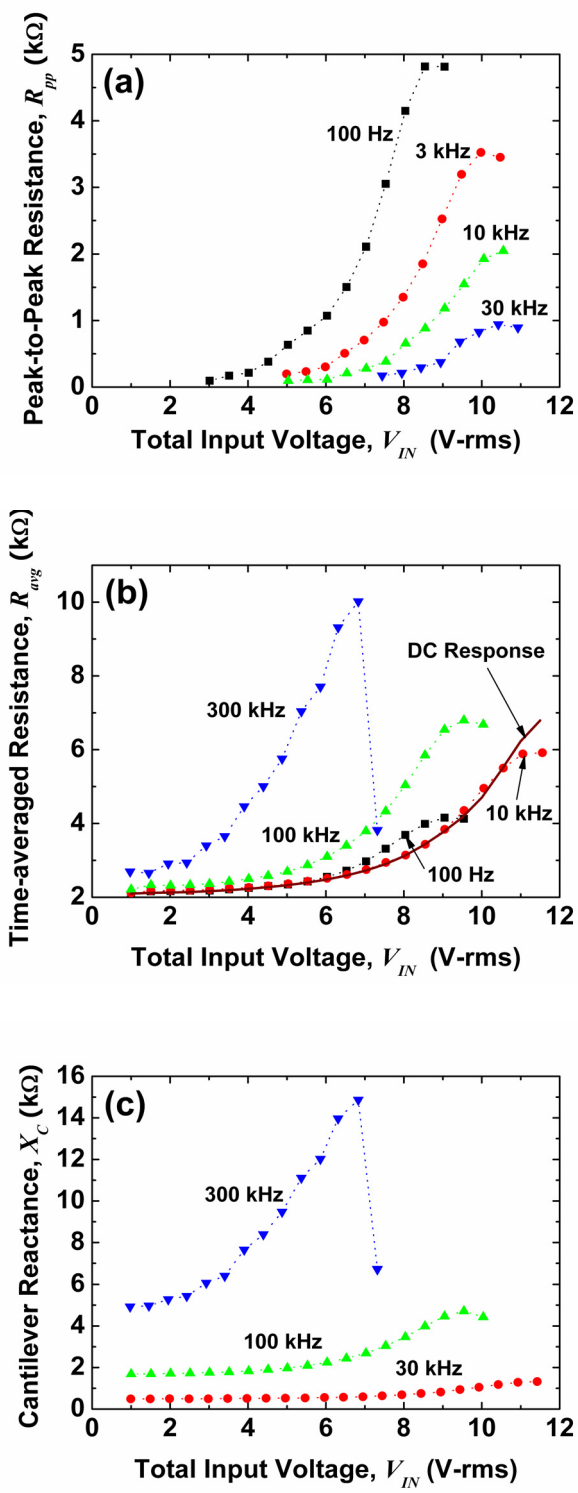

Figure 2.7 The cantilever resistance and reactance for various total input voltages and different frequencies. (a) The peak-to-peak oscillation amplitudes of the cantilever resistance decreases as the frequency increases. (b) The time-averaged cantilever resistance approaches the DC response as the frequency increases, but the impedance effect increases the resistance far from the DC response. (c) The cantilever reactance clearly shows the effect of the impedance in the high frequency region.

point crosses the boundary of the 1ω region. This sudden decrease of the cantilever resistance and reactance is likely the combined response of the thermal runaway and the electronic impedance of the sense resistor. Therefore, for frequencies higher than 30 kHz, the thermal behavior of the cantilever significantly deviates from the DC response, requiring detailed numerical modeling to interpret experimental results.

2.4 Numerical Modeling

Numerical [9,10] and analytical [21] models have predicted the thermal and electrical characteristics of the cantilever during heating. These studies provided physical insights of the heat transfer mechanisms and helped clarify various design parameters and their effects on the cantilever performance. However, little attention was paid to the transient response of the cantilever to periodic excitation.

Provided that the thermal resistances across the cantilever thickness and width are very small compared to that along or from the cantilever, the cantilever can be modeled with one-dimensional heat conduction equation [10]:

$$\rho c \frac{\partial T_C}{\partial t} = \frac{1}{A_C} \frac{\partial}{\partial x} \left(k_C A_C \frac{\partial T_C}{\partial x} \right) + g''' - h_a P (T_C - T_\infty) \tag{2.7}$$

where ρ is the density, c the specific heat, k_C the thermal conductivity, A_C the cross sectional area, g''' the volume density of heat generation, h_a the heat transfer coefficient, P the perimeter, T_∞ the surrounding temperature, and T_C the cantilever temperature. Due to the symmetry, only half of the cantilever was modeled with the adiabatic boundary condition at the free end. The opposite end was assumed to be fixed with the room temperature as the silicon base can be taken as a heat sink. The heat transfer

coefficient, h_a, was obtained from the thermal behavior of the cantilever far from the substrate [12,22]. The estimated heat transfer coefficient is in the range between 1,000 and 5,000 W/m^{2}K, depending on temperature. This large heat transfer coefficient is due to the reduced surface area of the cantilever. Since the cantilever thickness can vary depending on the fabrication condition, it was measured with SEM to be 590 nm with around 10 % uncertainty. Standard values of silicon properties were used for the density and specific heat [23]. The thermal conductivity of the cantilever was taken from empirical and theoretical works considering the doping level, temperature, and size effect [24-28].

Since all the variables in Eq. (2.7) are position-dependent, a fully implicit finite-difference method was employed for physically-realistic and stable computation. In the calculation, Δx is set to 0.5 μm and Δt is chosen to be one hundredth of the voltage oscillation period to achieve a good accuracy [29]. The challenge is to obtain the cantilever resistance at each node as a function of temperature, which is semi-empirically obtained from Fig. 2.3(a). The cantilever temperature is iteratively calculated until the cantilever resistance converges to within 0.01 %. The quasi-steady solution is obtained when the cantilever resistance changes less than 0.01 % compared to the previous period. However, Fig. 2.3(a) is not applicable when the frequency is higher than 10 kHz, because the resistance significantly deviates from the DC response. Instead, the cantilever temperature can be calculated from the power dissipation in the cantilever, which depends on the following cantilever impedance:

$$Z_C = \frac{R_C + j\omega L_C}{1 - \omega^2 L_C C_C + j\omega R_C C_C} \tag{2.8}$$

Since Z_C becomes R_C at steady state, the DC resistance curve in Fig. 2.3(b) was applied to determine R_C. The cantilever capacitance, C_C, and the cantilever inductance, L_C, were determined from the measured cantilever electrical impedance. Estimated C_C and L_C are in the order of 10 pF and 100 μH. These capacitance and inductance parasitically lie in the cantilever, and their values depend on the cantilever geometry and the environment. Since the objective of this study is to characterize the cantilever under a typical AFM operation, the experiment was performed in a commercial AFM (Asylum MFP-3D), and no special treatment was taken to suppress these parasitic effects.

Before the numerical model was applied to AC operation, the model was validated in DC operation. The cantilever response in DC operation was calculated and compared with the measurements in Fig. 2.3(b). The simulation results and the measured data are in good agreement within 1.2 % standard error, suggesting that the numerical model can provide a reasonable estimate of the cantilever temperature in AC operation. Figure 2.8(a) shows the cantilever resistance and reactance versus frequency when the input voltage is fixed at 7 V-rms. The calculated values match well with the experimental data: only the simulated peak-to-peak resistance overestimates the measurements with a 7.4 % relative error at low frequencies. This deviation could be attributed to an underestimate of the volumetric heat capacity of the cantilever or the variation of the effective heat transfer coefficient. The cantilever heater temperature in Fig. 2.8(b) shows a similar trend as the resistance, confirming that the temperature can be estimated with the resistance change even in the AC mode operation. It is also noteworthy that the frequency-dependence of the cantilever heater temperature shows a similar trend to that of a harmonic signal in Fig. 2.4(a). More specifically, the time-averaged response can be related to the 1ω signal, whereas the

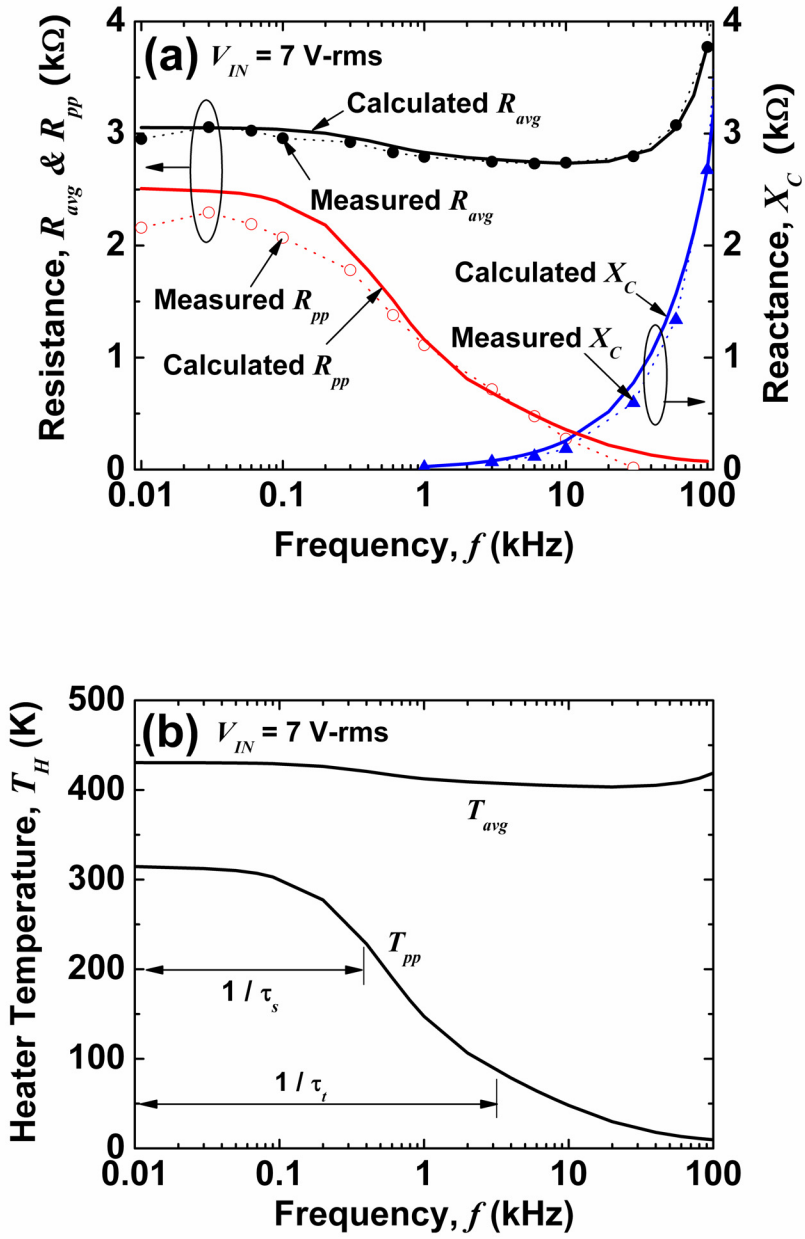

Figure 2.8 The calculated results on the electrical and thermal responses of the cantilever. (a) Comparison of the cantilever impedances that are experimentally and numerically obtained when the frequency varies at a fixed input voltage 7 V-rms. (b) Calculated cantilever heater temperature for the same case as (a). In the figure, τ_s is the settling time constant whereas τ_t is the thermal time constant.

peak-to-peak amplitude to the 3ω signal. After all, the 1ω and 3ω signals are generated mostly due to the time-averaged cantilever resistance and the resistance oscillation amplitude, respectively. By monitoring the 1ω and 3ω signals of the cantilever voltage, one can estimate the AC cantilever heater temperature in real time without any post-analysis of the data.

In order to safely operate the cantilever in AC mode, it is important to wisely choose the driving frequency according to intrinsic time constants of the cantilever. Figure 2.8(b) provides two different thermally-related time constants. The "slow" time constant is the time needed for the cantilever and its holder to reach a thermal equilibrium with the environment [7], and can be obtained from the frequency at which the peak-to-peak resistance decreases to −3 dB (i.e., 70 %) of the maximum [20]. The "slow" time constant, or the *settling time constant*, is estimated to $\tau_s = 2.5$ ms, which corresponds to 400 Hz. If the driving frequency is slower than the settling time constant, the frequency has no effect on the thermal response of the cantilever. The "fast" time constant, or the *thermal time constant*, determines how fast the cantilever thermally responds to an abrupt change of the cantilever power. The thermal time constant is obtained from the frequency at which the peak-to-peak resistance decreases to be −30 dB (i.e., 30%) of the maximum value. The thermal time constant is estimated to be $\tau_t = 280$ μs, which is in the same order of the thermal time constant measured from the heating pulse experiment [12]. While not investigated here, there should be another time constant close to 1 MHz that is associated with the heating and cooling of only the cantilever heater region.

Figure 2.9(a) shows the heater temperature oscillations at different frequencies. When the frequency is low (i.e., below 100 Hz), the temperature oscillates with a large

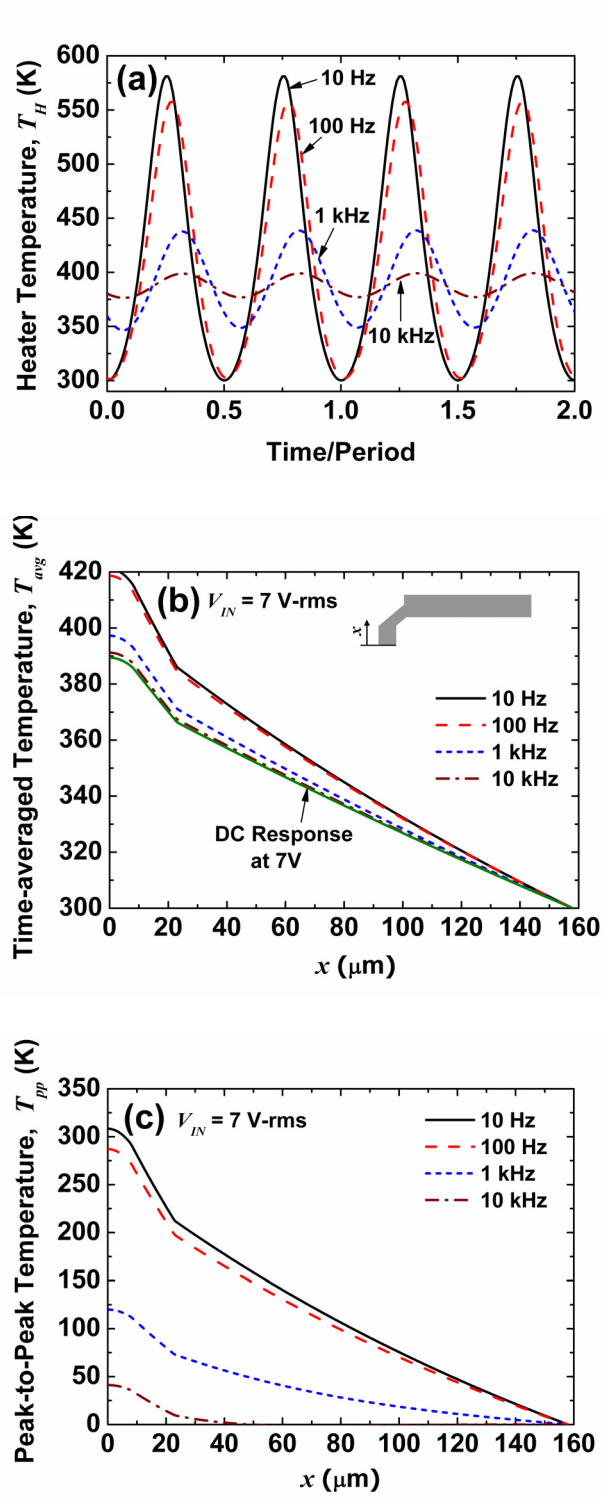

Figure 2.9 The calculated temperature of the cantilever. (a) The traces of the cantilever heater temperatures at the total input voltage 7 V-rms. (b) Calculated time-averaged temperature and (c) peak-to-peak temperature distribution along the cantilever for the same case as (a).

amplitude, decreasing to the room temperature when the input power reaches zero. As frequency increases, the temperature oscillation amplitude becomes small, approaching a constant time-averaged temperature. It should be noted that the time-averaged temperature is not located in the middle of the oscillation: simply taking a median value from the temperature oscillation would provide an erroneous estimate of the time-averaged temperature. Figures 2.9(b) and (c) provide the time-averaged and peak-to-peak temperature distributions along the cantilever. As the frequency increases, the time-averaged temperature distribution approaches the DC response. Interestingly, when the frequency is 10 kHz, the peak-to-peak temperature distribution becomes zero everywhere except the heater region: the temperature oscillation is restricted to only a small part of the cantilever. This local temperature oscillation would allow the cantilever to be used for a very sensitive thermogravimetry, or for the measurement of thermophysical properties of a substrate, such as the thermal conductivity and diffusivity.

2.5 Conclusion

This work characterized a heated microcantilever in AC operation. Spectrum analysis suggests that higher order harmonic signals must be considered to accurately describe the thermal behavior of the cantilever. Below 100 Hz, the cantilever resistance fully follows the power oscillation because the time taken for the cantilever to reach a thermal equilibrium with its environment is faster than its periodic-heating frequency. As the frequency increases, however, the cantilever cannot thermally respond to the power oscillation fast enough, and the thermal lag results in a suppression of the cantilever resistance oscillation. Furthermore, the cantilever impedance begins to play a role in the

electric behavior at high frequencies. The temperature oscillation of the cantilever was predicted with a numerical model. Comparison of the calculation and measurement suggests that the cantilever heater temperature can be monitored in real time with the first and third harmonic cantilever voltage signals. The frequency-dependence of the cantilever thermal behavior determines two different time constants: 280 μs as the thermal time constant and 2.5 ms as its settling time constant. When the cantilever is operated at frequencies higher than the thermal time constant, the temperature oscillation is restricted to the cantilever heater region. The obtained results provide better understanding of heated microcantilevers, particularly when it is used in periodic operation for sensitive AFM-based thermal metrologies.

.

2.6 References

[1] S. Lefèvre and S. Volz, "3ω-scanning thermal microscope," *Review of Scientific Instruments*, vol. 76, 033701, 2005.

[2] R. Berger, H. P. Lang, C. Gerber, J. K. Gimzewski, J. H. Fabian, L. Scandella, E. Meyer, and H. J. Guntherodt, "Micromechanical thermogravimetry," *Chemical Physics Letters*, vol. 294, pp. 363-369, 1998.

[3] T. R. Albrecht, P. Grutter, D. Horne, and D. Rugar, "Frequency-modulation detection using high-Q cantilevers for enhanced force microscope sensitivity," *Journal of Applied Physics*, vol. 69, pp. 668-673, 1991.

[4] O. Kwon, L. Shi, and A. Majumdar, "Scanning thermal wave microscopy (STWM)," *Journal of Heat Transfer*, vol. 125, pp. 156-163, 2003.

[5] A. Altes, R. Heiderhoff, and L. J. Balk, "Quantitative dynamic near-field microscopy of thermal conductivity," *Journal of Physics D-Applied Physics*, vol. 37, pp. 952-963, 2004.

[6] G. S. Shekhawat and V. P. Dravid, "Nanoscale imaging of buried structures via scanning near-field ultrasound holography," *Science*, vol. 310, pp. 89-92, 2005.

[7] B. W. Chui, T. D. Stowe, Y. S. Ju, K. E. Goodson, T. W. Kenny, H. J. Mamin, B. D. Terris, R. P. Ried, and D. Rugar, "Low-stiffness silicon cantilevers with integrated heaters and piezoresistive sensors for high-density AFM thermomechanical data storage," *Journal of Microelectromechanical Systems*, vol. 7, pp. 69-78, 1998.

[8] W. P. King, T. W. Kenny, K. E. Goodson, G. Cross, M. Despont, U. Dürig, H. Rothuizen, G. K. Binnig, and P. Vettiger, "Atomic force microscope cantilevers for combined thermomechanical data writing and reading," *Applied Physics Letters*, vol. 78, pp. 1300-1302, 2001.

[9] B. W. Chui, M. Asheghi, Y. S. Ju, K. E. Goodson, T. W. Kenny, and H. J. Mamin, "Intrinsic-carrier thermal runaway in silicon microcantilevers," *Microscale Thermophysical Engineering*, vol. 3, pp. 217-228, 1999.

[10] W. P. King, "Design analysis of heated atomic force microscope cantilevers for nanotopography measurements," *Journal of Micromechanics and Microengineering*, vol. 15, pp. 2441-2448, 2005.

[11] B. W. Chui, T. D. Stowe, Y. S. Ju, K. E. Goodson, T. W. Kenny, H. J. Mamin, B. D. Terris, and R. P. Ried, "Low-Stiffness Silicon Cantilever with Integrated Heaters and Piezoresistive Sensors for High-Density Data Storage," *Journal of Microelectromechanical Systems*, vol. 7, pp. 69-78, 1998.

[12] J. Lee, T. Beechem, T. L. Wright, B. A. Nelson, S. Graham, and W. P. King, "Electrical, thermal, and mechanical characterization of silicon microcantilever-heaters," *Journal of Microelectromechanical Systems*, vol. 15, pp. 1644-1655, 2006.

[13] M. Pecht, P. Lall, G. Ballou, C. Sankaran, and N. Angelopoulos, "Passive components," in *The Electrical Engineering Handbook*, R. C. Dorf, Ed. Boca Raton: CRC Press LLC, 2000.

[14] B. McCarthy, Y. M. Zhao, R. Grover, and D. Sarid, "Enhanced Raman scattering for temperature measurement of a laser-heated atomic force microscope tip," *Applied Physics Letters*, vol. 86, 111914, 2005.

[15] M. R. Abel, T. L. Wright, W. P. King, and S. Graham, "Thermal metrology of silicon micro-structures using Raman spectroscopy," *IEEE Transactions on Components and Packaging Technologies*, to be published.

[16] D. G. Cahill, "Thermal conductivity measurement from 30 to 750 K: the 3ω method," *Review of Scientific Instruments*, vol. 61, pp. 802-808, 1990.

[17] T. Borca-Tasciuc, A. R. Kumar, and G. Chen, "Data reduction in 3ω method for thin-film thermal conductivity determination," *Review of Scientific Instruments*, vol. 72, pp. 2139-2147, 2001.

[18] L. Lu, W. Yi, and D. L. Zhang, "3ω method for specific heat and thermal conductivity measurements," *Review of Scientific Instruments*, vol. 72, pp. 2996-3003, 2001.

[19] N. Kim, B. Comercq, S. Yoo, A. Christensen, B. Kippelen, and S. Graham, "Thermal transport properties of thin films of small molecule organic semiconductors," *Applied Physics Letters*, vol. 87, 241908, 2005.

[20] P. Horowitz and W. Hill, *The Art of Electronics*, 2nd ed., New York: Cambridge University Press, 1989.

[21] U. Dürig, "Fundamentals of micromechanical thermoelectric sensors," *Journal of Applied Physics*, vol. 98, 044906, 2005.

[22] J. Lee, T. L. Wright, M. R. Abel, E. O. Sunden, A. Marchenkov, S. Graham, and W. P. King, "Thermal conduction from microcantilever heaters in partial vacuum," *Journal of Applied Physics*, vol. 101, 014906, 2007.

[23] Y. S. Touloukian and E. H. Buyco, *Specific Heat : Metallic Elements and Alloys*, vol. 4, New York,: IFI/Plenum, 1970.

[24] D. Fortier and K. Suzuki, "Effect of *p*-donors on thermal phonon scattering in Si," *Journal De Physique*, vol. 37, pp. 143-147, 1976.

[25] B. W. Chui, "Advanced silicon micromachined cantilevers for atomic force microscope data storage," Ph. D dissertation, Dept. Elec. Eng., Stanford Univ., Palo Alto, CA, 1998.

[26] M. Asheghi, K. Kurabayashi, R. Kasnavi, and K. E. Goodson, "Thermal conduction in doped single-crystal silicon films," *Journal of Applied Physics*, vol. 91, pp. 5079-5088, 2002.

[27] W. Liu and M. Asheghi, "Thermal conduction in ultrathin pure and doped single-crystal silicon layers at high temperatures," *Journal of Applied Physics*, vol. 98, 123523, 2005.

[28] W. J. Liu and M. Asheghi, "Thermal conductivity measurements of ultra-thin single crystal silicon layers," *Journal of Heat Transfer*, vol. 128, pp. 75-83, 2006.

[29] S. V. Patankar and B. R. Baliga, "A new finite-difference scheme for parabolic differential equations," *Numerical Heat Transfer*, vol. 1, pp. 27-37, 1978.

CHAPTER 3

CHARACTERIZATION OF HEATED MICROCANTILEVERS AT LOW TEMPERATURES

This chapter describes the electrical and thermal behaviors of heated microcantilevers under steady- and periodic-heating operation at low temperatures and in vacuum. The cantilever resistance drastically increases as temperature decreases below 150 K, providing a large and negative temperature coefficient of resistance of –0.023 K^{-1} at 100 K. Under steady-heating, the cantilever heater can be heated above 300 K even when its environment is at 77 K. Electrical and thermal transfer functions are derived to depict the electrical and thermal cantilever responses under periodic heating and to extract cantilever thermophysical properties. The calculation of in-phase and out-of-phase temperatures along the cantilever reveals that its response becomes out of phase and restricted to the heater region at high frequencies. These results enable the use of heated cantilevers in cryogenic applications as a localized heat source and a sensitive thermal metrology tool.

3.1 Introduction

Cryogenic atomic force microscopy, or cryo-AFM, provides promising opportunities for AFM-based applications at low temperatures [1-3], perhaps most notable is high resolution imaging of biomolecules. By operating AFM at 77 K, difficulties in achieving high resolution at room temperature can be overcome, such as

sample softness or thermal motion of macromolecules. Radenovic et al. [2] showed that a cryo-AFM in ultrahigh vacuum can accurately measure DNA plasmid height, while the room temperature measurement provides only half of the true value. The probe mechanical properties such as resonance frequency, spring constant, and quality factor depend upon temperature [3]. Few if any cryo-AFM studies have focused on thermal applications. If heated AFM cantilevers were used as a thermal source in cryo-AFM, new AFM measurements would be possible such as thermal property measurement of frozen cells, low temperature calorimetry, study of local heating effect on freezing processes, and thermal management in cryopreservation [4]. The low-temperature electrical and thermal behavior of heated cantilevers must be understood in order to realize these applications. However, nearly all of the published works of heated microcantilevers have focused on room temperature. While one paper places the cantilever in a cryostat [5], no paper has reported detailed cryogenic operation.

This chapter describes electrical and thermal behaviors of heated microcantilevers at low temperatures. While varying the stage temperature in a cryostat, steady-state characterization was performed by monitoring the temperature-dependent cantilever electrical resistance. For periodic-heating analysis, electrical and thermal transfer functions were derived and used to determine frequency-dependent cantilever thermal behaviors as well as the thermophysical properties of the cantilever at low temperatures. The periodic cantilever temperature was calculated from the measured properties and thermal diffusion time. The results obtained in this work aim to expand the use of the heated microcantilevers to cryogenic conditions.

3.2 Experiment

The experiment was performed with a heated microcantilever mounted in a Janis He-3-SSU-He3 refrigerator. A heated cantilever used in the experiment was of the same geometry as that described in Chapter 2. Figure 3.1 shows the stage of the cryostat containing a resistive heater and a thermometer so that the stage temperature can be controlled by a PID temperature controller. A 100 Ω platinum resistance thermometer measured temperature from 77 K to room temperature. The cantilever resistance was monitored simultaneously to verify thermal equilibrium between the stage and the cantilever. The measurements were performed at various stage temperatures starting from 77 K. Vacuum condition better than 10^{-7} bar was maintained during the experiment. In this vacuum condition, thermal conduction along the length of the cantilever dominates thermal radiation [5].

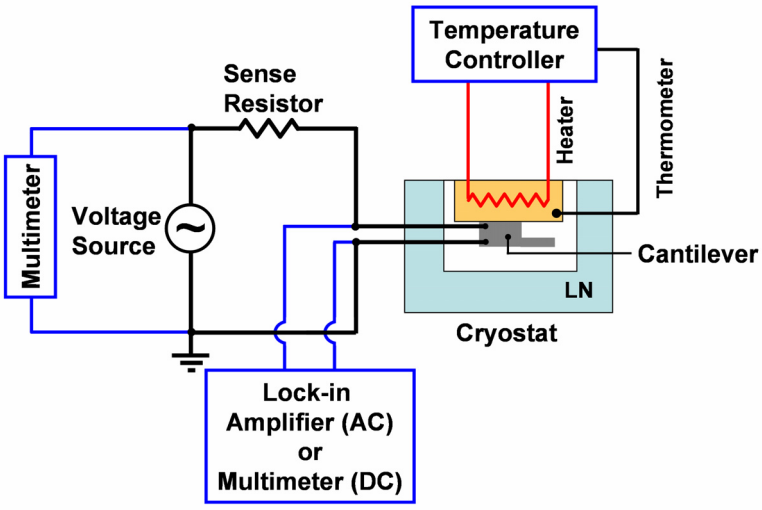

Figure 3.1 The experimental description for the cantilever characterization at low temperature. The cantilever is mounted on a stage whose temperature can be controlled in the range of 77 K to 300 K. A good vacuum condition is maintained around the cantilever.

The cantilever was characterized in under both steady (DC) and periodic (AC) heating excitation. In DC operation, the cantilever was characterized by obtaining its temperature-dependent electrical resistance. In periodic-heating operation, or AC operation, harmonic voltage signals across the cantilever was measured with a lock-in amplifier under a differential scheme [6]. While increasing the driving frequency at a fixed input voltage, the AC experiment was performed by measuring the harmonic cantilever voltage and the current, which can be obtained by $I = V_S / R_S$ where V_S is the voltage drop across the sense resistor of the resistance R_S. The sense resistor was a non-inductive 10 kΩ resistor with 1% tolerance. This resistor response is purely resistive at frequencies up to 100 MHz, preventing the electrical impedance effect discussed in Chapter 2.

3.3 Steady-Heating Operation

The cantilever resistance is temperature-dependent and can be used to estimate the temperature of the heater region [7]. Figure 3.2 shows temperature calibration of the cantilever resistance, when the stage was in thermal equilibrium with the cantilever. The cantilever power dissipation during the measurement was 0.2 μW, yielding a heater temperature increase < 0.02 K. In Fig. 3.2, the cantilever resistance increases dramatically as temperature decreases. This behavior is much different from the cantilever resistance change above room temperature, i.e., in Fig. 2.3. At low temperature, the cantilever temperature coefficient of resistance (TCR), defined as $b(T) = (1/R)(dR/dT)$, is negative and large. At 100 K the estimated cantilever TCR is $-0.023\ \mathrm{K}^{-1}$, which is about twice that of platinum, $0.013\ \mathrm{K}^{-1}$. This large TCR suggests

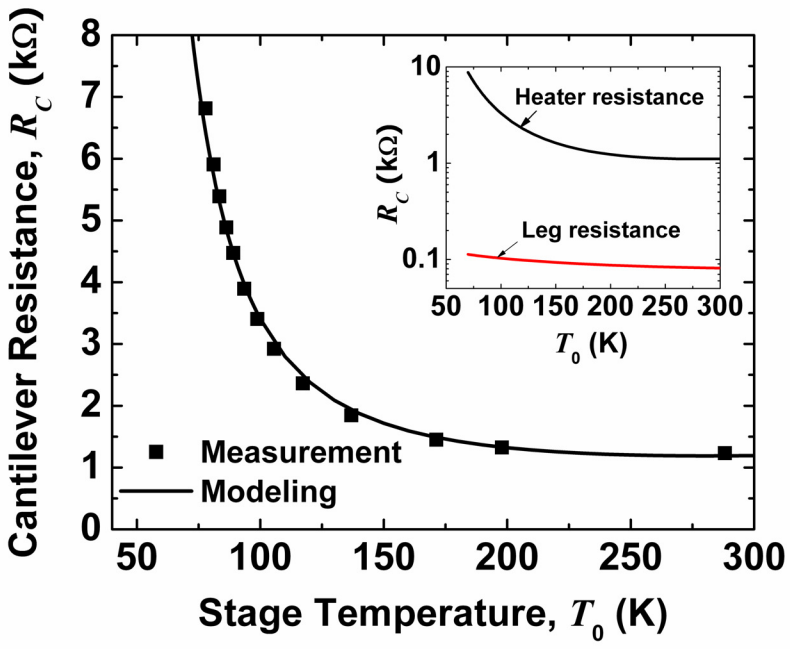

Figure 3.2 The cantilever resistance change as a function of temperature. Marks denote the measured values whereas the solid curve is calculation. The inset shows the calculated resistance of the heater region and that of the leg region including the thermal constriction and the anchor.

$-0.023\ \mathrm{K}^{-1}$, which is about twice that of platinum, $0.013\ \mathrm{K}^{-1}$. This large TCR suggests that the heated cantilever can sensitively measure cryogenic temperature.

The temperature-dependence of the cantilever resistance may be understood using a temperature-dependant resistivity model of phosphorus-doped silicon. Assuming that the minority carrier density is negligibly small, the resistivity can be calculated with $\rho = 1/(en\mu_e)$, where e, n, and μ_e are respectively the electron charge, density, and mobility. Even though silicon electron density and mobility have been extensively studied [8-11] and general knowledge is available in textbooks [12-14], there are not many resistivity models that accurately predict the resistivity change for wide range of temperatures from 50 K to 400 K and doping levels from 10^{16} cm^{-3} to 10^{21} cm^{-3}. Furthermore, available models from the literature are not consistent with each other, as

they still have many restrictions [9,15,16]. Here we develop a model for the cantilever resistance by modifying available models for bulk silicon.

Recently, Mnatsakanov et al. [17] suggested a simple analytical carrier mobility model that is applicable to various semiconductors for a wide range of temperatures and dopant densities, with accuracy within 7 % relative error on average [17]. Modeling of the electron density for *n*-doped silicon starts from the charge neutral condition, which equates the electron density and ionized donor density, $n \simeq N_D^+$, if the minor carrier numbers are negligible. Assuming Fermi-Dirac statistics, parabolic energy bands, and a single-energy impurity level, Blakemore [18] developed a model for calculating the electron density, in which the electron density and the ionized donor density are

$$n = N_C F_{1/2}(\eta) \tag{3.1}$$

and

$$N_D^+ = N_D \left\{ 1 - \frac{1}{1 + 0.5 \exp\left[(E_D - E_F)/k_B T \right]} \right\} \tag{3.2}$$

$F_{1/2}(\eta)$ is a Fermi-Dirac integral of order 1/2 as a function of $\eta = (E_F - E_g)/k_B T$, based on zero energy level of the valence band, i.e., $E_V = 0$ [19]; E_F is the Fermi energy; E_g is the band gap energy given by $E_g = 1.165 - 0.000473T^2/(T + 673)$ [20]; k_B is the Boltzmann constant; N_D is the dopant density; and E_D is the donor energy level. The donor energy level E_D, or the donor ionization energy $\Delta E_D \equiv E_C - E_D$, is dependent upon the dopant density according to the $N_D^{1/3}$ law [9,21]:

$$\Delta E_D = \Delta E_D(0) - \zeta N_D^{1/3} \tag{3.3}$$

where $\Delta E_D(0) = 0.045$ eV is the ionization energy of the phosphorus donor, and ζ is a coefficient to be used as a fitting parameter. The electron density model given by Eqs. (3.1) thru (3.3) was verified by comparing computed electron densities with the measured values [22,23] over the temperature range from 50 K to 300 K for several dopant densities lower than 1×10^{18} cm^{-3}: they are in good agreement within 8%. For dopant concentrations higher than approximately 1×10^{19} cm^{-3}, however, this model generates a considerable error because a high donor energy band is broadened and begins to merge with the conduction band, generating more free carriers than Eq. (3.2) would predict. The calculation [21] and measurement [24] suggested that when the doping concentration is higher than 1×10^{19} cm^{-3}, the dopant density is fully ionized and thus becomes independent of temperature: that is, the electron density is the same as the dopant density.

Based on the electron mobility and density models, the cantilever resistance was calculated with two fitting parameters. The first fitting parameter was ζ and determined to be 1.7×10^{-8} eV-cm, which is in the same order of those obtained in previous research [9,21]. Another fitting parameter was the effective dopant density of the heater and estimated to be 5.9×10^{17} cm^{-3}. However, since the leg region is heavily doped over 10^{20} cm^{-3}, the electron density of the leg region was simply obtained from the impurity diffusion analysis for given ion-implantation parameters. The calculated electron density of the leg is 4.3×10^{20} cm^{-3}. Figure 3.2 shows the calculated cantilever resistance together with the measurement. The cantilever resistance measurements were very accurate within 0.1 % uncertainty, and the agreement between the measurement and calculation is within 3 % relative error on average. The inset in Fig. 3.2 shows the

modeled resistance of the heater region and that of the leg region including the thermal constriction and the anchor. From the inset, it is clear that the most of the cantilever resistance is attributed to the heater region: the heater resistance takes more than 97% of the cantilever resistance at 100 K and 93% at room temperature. This result confirms that power is predominantly dissipated in the heater region. Under steady heating, Fig. 3.2 can be used to directly estimate the heater temperature from the cantilever resistance.

The drastic increase of the cantilever resistance at low temperatures can be attributed to electron freezing and large impurity scattering at the heater region. Compared to the heater region, the heavy dopant concentration of the leg region is completely ionized, and thus the leg resistance experiences little change with temperature. Note that the scattering rate is inversely proportional to the mobility $\mu = e / m_e^* \gamma$, where m_e^* is the electron effective mass and γ is the scattering rate. At around room temperature, the cantilever resistance becomes almost constant because the slightly increasing electron density competes with the slightly decreasing electron mobility. The decreasing mobility at room temperature is because increasing lattice scattering due to the increasing phonon density of states exceeds the decreasing impurity scattering. If temperature further increases over room temperature, the lattice scattering rate will continuously rise while the electron density becomes saturated, resulting in the increase of the cantilever resistance. However, the boundary scattering effect is negligibly small because the electron mean free path of is the order of 10 nm [24], much smaller than the cantilever thickness.

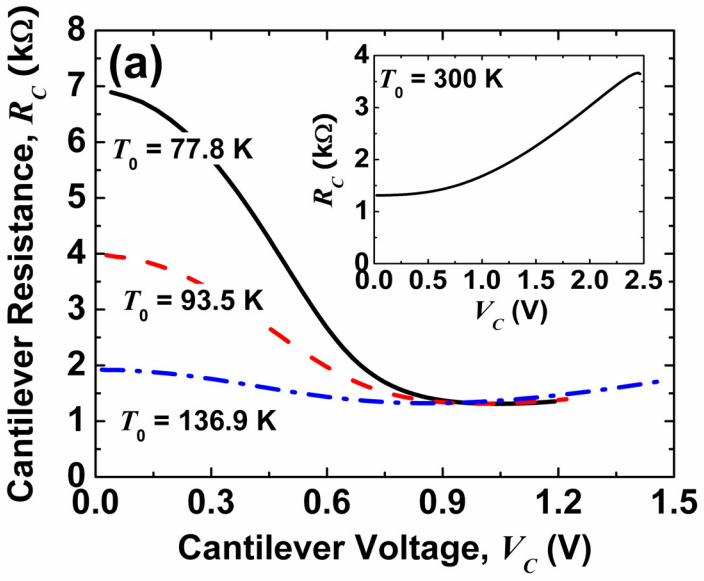

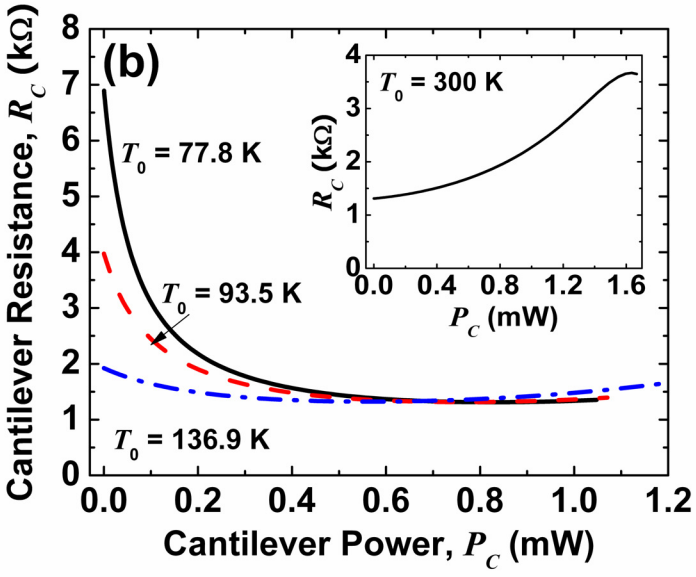

Figure 3.3 The cantilever resistance change (a) as a function of the cantilever voltage and (b) as a function of the cantilever power for different stage temperatures. The insets are the cantilever resistance change at room temperature. Solid curves are measured values.

Figures 3.3(a) and (b) show the DC characteristics of the cantilever measured at different stage temperatures. The cantilever resistance decreases as the cantilever voltage increases, which is consistent with Fig. 3.2. The cantilever resistance at $T_0 = 77.8$ K is reduced to the room temperature resistance when the cantilever voltage is around 1 V, indicating that the cantilever heater temperature is near 300 K. For higher stage temperatures, the cantilever resistance goes through the minimum values around 1.3 kΩ and then increases. When compared with cantilever response at room temperature shown in the insets, this increasing resistance is because of the temperature rise above room temperature. In fact, the cantilever can be heated much higher than room temperature as long as the electrical current through the cantilever does not exceed the maximum current density the cantilever can hold: if the current exceeds the limit, current congestion at the thermal constriction will cause a local temperature rise above silicon melting temperature. Because the cantilever heater temperature can be controlled from 77 K to 300 K when the cantilever base resides at 77 K, the heated cantilever could be used as a local thermal management tool in various cryogenic applications.

3.4 Periodic-Heating Operation

3.4.1 Electrical and thermal transfer functions

In order to correctly interpret the AC experimental results and extract meaningful thermophysical properties from data, several analytical and numerical approaches have been suggested for various thermal systems [25-28]. Recently, Dames and Chen [29] suggested a general framework of thermal and electrical transfer functions of a sample

containing a line heater, such that the electrical and thermal responses of the sample can be clarified when it is under a periodic joule heating with or without a DC offset. However, their transfer functions are not applicable when power is not uniformly dissipated over the sample, which is the characteristic feature of the heated cantilever. Previous reports provide an insufficient framework to analyze the heated cantilever, and so this paper establishes transfer functions that overcome these limitations and can be applied to more general cases.

When the cantilever is heated by a sinusoidal current at angular frequency ω, $I(t) = I_1 \sin(\omega t)$, the cantilever resistance can be approximated to

$$R_C(t) = R_0 \left[1 + \sum_i \xi_i b_i \bar{\Theta}_i(t) \right] \tag{3.4}$$

under the condition that the cantilever consists of four electrically active parts, i.e., heater, thermal constriction, leg, and anchor. Here, R_0 is the DC cantilever resistance at a specific temperature, b_i and $\bar{\Theta}_i(t)$ are respectively the TCR and averaged temperature oscillation at each part. $\xi_i \equiv R_i / R_0$ denotes the ratio of the individual resistance to the DC cantilever resistance, satisfying $\sum \xi_i = 1$. The index i is taken as *h, c, l,* and *a*, each of which denotes heater, thermal constriction, leg, and anchor region. Equation (3.4) is valid for both linear and nonlinear resistance systems as long as the temperature oscillation amplitude is small: The nonlinearity is involved in the temperature-dependent DC resistance and TCR. Since $\sum \xi_i b_i \Theta_i(t) << 1$ in Eq. (3.4), the power dissipation at the cantilever can be approximated to $\dot{Q}(t) = I(t)^2 R_0$, and the average temperature oscillation $\bar{\Theta}_i(t)$ can be written as

$$\bar{\Theta}_i(t) = \dot{Q}_i(t) \otimes Z_{t,i} \tag{3.5}$$

where $\dot{Q}_i = \xi_i \dot{Q}(t)$ is the power dissipation of each part, $\otimes$ denotes convolution, and $Z_{t,i}$ is the inverse Fourier transform of the thermal transfer function $Z_{\omega,i}$. By combining Eqs. (3.4) and (3.5) and employing Ohm's law, the voltage drop across the cantilever can be expressed as

$$V_C(t) = I(t)R_0\left[1 + R_0 \sum \xi_i^2 b_i Z_{t,i} \otimes I^2(t)\right] \tag{3.6}$$

If the thermal transfer function of the cantilever is defined as

$$Z_C \equiv \frac{1}{b_0} \sum \xi_i^2 b_i Z_{t,i} \tag{3.7}$$

where b_0 is the cantilever TCR obtained from the measurement, electrical transfer functions over the harmonics *n* can be expressed as [29]

$$\frac{V_{n\omega,rms}}{2b_0 R_0^2 I_{1,rms}^3} = X_{n\omega}(\omega) + jY_{n\omega}(\omega) \tag{3.8}$$

Where $V_{n\omega,rms}$ is rms-harmonic signals of the cantilever voltage, and $j = \sqrt{-1}$. Here, $X_{n\omega}$ and $Y_{n\omega}$ are in-phase and out-of-phase electrical transfer functions and can be related with thermal transfer functions, as suggested by Dames and Chen [29].

The thermal transfer function of the cantilever can be obtained by modeling heat transfer in each region of the cantilever. Since the thermal resistance across the thickness and the width of the cantilever is very small compared to the thermal resistance along or from the cantilever, one-dimensional transient heat conduction equation is appropriate for the thermal modeling of the cantilever:

$$C_i \frac{\partial \Theta_i(x,t)}{\partial t} = k_i \frac{\partial^2 \Theta_i(x,t)}{\partial x^2} + \frac{\dot{Q}_i(t)}{V_i} \tag{3.9}$$

where $\Theta_i(x,t)$, C_i, k_i, and $\dot{Q}_i(t)$ are the temperature oscillation, the volumetric heat capacity, the thermal conductivity, and the power dissipation of each region of volume V_i. The equation is set on the local coordinate of the control volume: x ranges from 0 to l_i, the length of the i-th region. Since the cantilever is symmetric, only half of the cantilever is modeled with the adiabatic boundary condition at the free end. The opposite end at the anchor can be assumed to be maintained with the stage temperature as the silicon base can be taken as a heat sink. Good vacuum condition during the experiment prevents the convection heat loss from the cantilever to the environment. Radiation heat loss can also be neglected during the periodic-heating operation of the cantilever. According to Lu et al. [28], radiation heat loss can be neglected if $8hT_0^3 l^2 / \pi^2 k\delta \ll 1$ for a suspended blackbody sample, where $h = 5.67\times10^{-8}$ W/m^{2}K^4 is the Stefan-Boltzmann constant, T_0 is the base temperature, l is the sample length, k is the thermal conductivity, and δ is the cantilever thickness. The estimated criterion value for the heated cantilever is 3.72×10^{-3}, which is small enough to neglect radiation heat loss.

If $\dot{Q}(t)$ is expressed as $\dot{Q}(t) = Q_\omega \cos(\omega_H t) = \mathrm{Re}\left[Q_\omega e^{j\omega_H t} \right]$, Eq. (3.9) can be Fourier transformed as

$$j\omega_H C_i \Theta_{\omega,i} = k_i \frac{\partial^2 \Theta_{\omega,i}}{\partial x^2} + \frac{Q_{\omega,i}}{V_i} \tag{3.10}$$

where $\Theta_i(x,t) = \mathrm{Re}\left[\Theta_{\omega,i} e^{j\omega_H t}\right]$ and ω_H is the heating frequency. Equation (3.10) can be solved with a modified matrix formulation [30]. After considerable manipulation, $\Theta_{\omega,i}$ can be obtained with the following equation:

$$\Theta_{\omega,i}(x,\omega_H) = Q_\omega \left\{ W_i(0,\omega_H)\cosh\left[\beta_i x(1+j)\right] - \frac{f_i(0,\omega_H)}{k_i A_i \beta_i (1+j)}\sinh\left[\beta_i x(1+j)\right] + \frac{\xi_i}{j\omega_H C_i V_i} \right\} \tag{3.11}$$

where $\beta_i = \sqrt{\omega_H / 2\alpha_i}$ is the thermal wave vector, $\alpha_i = k_i / C_i$ is the thermal diffusivity, $W_i(x,\omega_H) = (\Theta_{\omega,i} / Q_\omega) - \left(\xi / j\omega_H CV\right)_i$ is an equivalent temperature oscillation, and $f_i(x,\omega) = -k_i A_i \, \partial W_i / \partial x$ is the nondimensional heat transfer rate at each region. The thermal transfer function of each region can be calculated from Eq. (3.11), yielding

$$Z_{\omega,i}(\omega_H) = \frac{W_i(0,\omega_H)}{\xi_i \beta_i l_i (1+j)}\sinh\left[\beta_i l_i (1+j)\right] + \frac{f_i(0,\omega_H)}{\xi_i k_i V_i {\beta_i}^2 (1+j)^2}\left\{1 - \cosh\left[\beta_i l_i (1+j)\right]\right\} + \frac{1}{j\omega_H C_i V_i} \tag{3.12}$$

Thus, the thermal transfer function of the cantilever can be obtained from Eqs. (3.7) and (3.12). It should be emphasized that the thermal transfer function can be interpreted as the thermal impedance, representing the amount of temperature rise for a given unit AC power.

In order to compromise the deviation of the thermal transfer function caused by using a voltage source, not an ideal current source, in the experiment, thermal transfer function is modified to [29]

$$Z_{true} = Z_C \left(1 - \frac{R_c}{R_{total}}\right)^{-1} \tag{3.13}$$

where Z_C is calculated from Eq. (3.12), and R_{total} is total resistance including the cantilever resistance, the wire resistance, and the output impedance of the voltage source. Equation (3.12) is now combined with Eq. (3.13) to characterize electrical and thermal cantilever response under periodic heating. In addition, cantilever thermophysical properties such as the thermal conductivity and specific heat can be obtained from the measurement.

3.4.2 Results and discussion

As in the DC characterization, AC experiment was performed for different stage temperatures from 77 K to 200 K. 1ω and 3ω cantilever voltage signals were measured while a small input voltage (i.e., $V_{IN} = 0.3$ V-rms) was applied to the circuit. Figures 3.4(a) and (b) show in-phase and out-of-phase 1ω cantilever voltages for three stage temperatures. The in-phase signals in Fig. 3.4(a) maintain their values until around 10 kHz and drastically decrease. On the other hand, the out-of-phase signals have valleys in the range from 30 kHz to 100 kHz, depending on the stage temperature. These cantilever responses are due to changing electrical impedance of the cantilever, rather than changing thermal characteristics. The equivalent circuit illustrated in the inset of Fig. 3.4(a) represents the cantilever as a parallel connection of a resistor R_C and a capacitor C_C, yielding the cantilever voltage as

$$V_{1\omega} = \frac{R_C V_{IN}}{(R_S + R_C) + j\omega R_S R_C C_C} \tag{3.14}$$

1ω cantilever voltages calculated from the above equation are plotted together in Fig. 3.4 with solid curves. Calculated values agree very well with the measurement except around

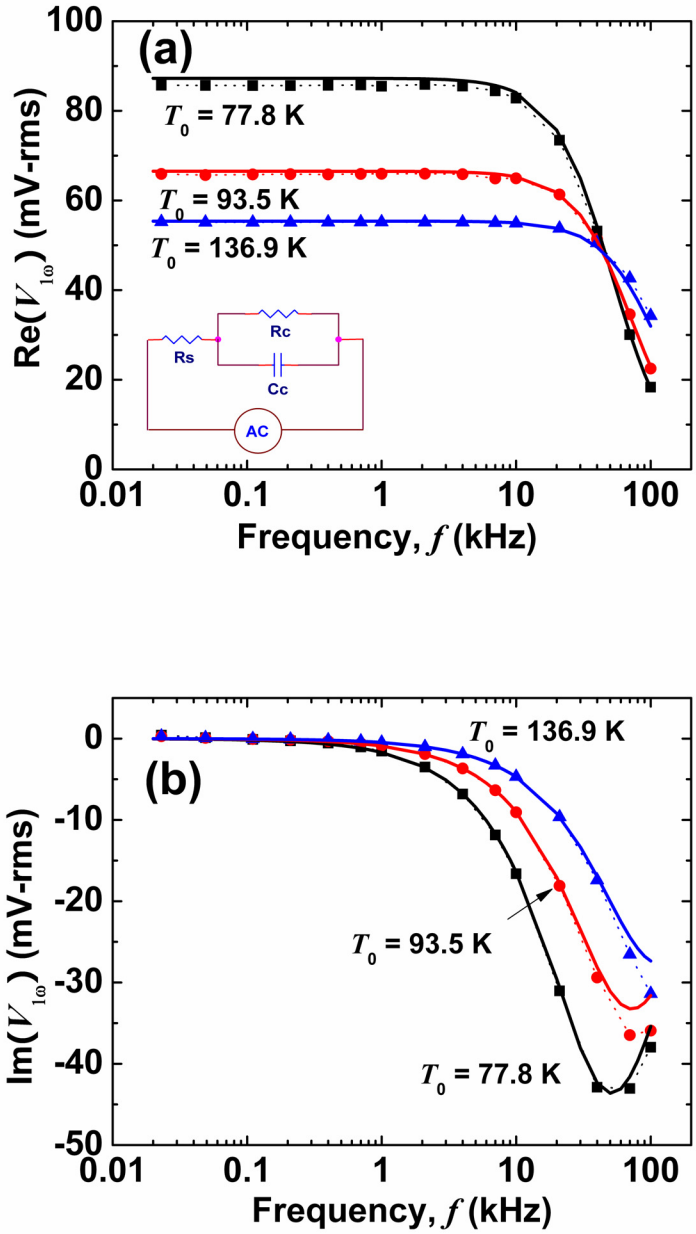

Figure 3.4 1ω cantilever voltage signals for different stage temperatures. (a) Real and (b) imaginary components of the 1ω cantilever voltage indicate that the cantilever can be modeled as a parallel connection of the equivalent resistance and capacitor, as illustrated in the inset of (a). The solid curves are calculated values from the equivalent circuit.

valleys of out-of-phase signals at higher stage temperatures. The cantilever capacitance C_C is estimated in the order of 100 pF. However, the cantilever inductance is negligibly small, which is different from Chapter 2. In fact, these parasitic capacitance and inductance depend on cantilever geometries and its operation environments. As discussed in 0, the presence of the cantilever capacitance and/or inductance significantly changes the cantilever electrical behavior at frequencies higher than 10 kHz. Combined with the cantilever capacitance, the decreasing cantilever resistance with temperature reduces the signal magnitudes and shifts the valley position of the out-of-phase signal to the higher frequency. Since the electrical impedance effect on the 1ω signal is significant, the thermal information of the 1ω signal is hardly recognizable: after all, the harmonic cantilever voltage change due to the thermal effect is on the order of 100 μV-rms for the setup input voltage, much smaller than that due to the electrical impedance effect.

Figures 3.5(a) and (b) show the in-phase and out-of-phase electrical transfer functions obtained from the 3ω cantilever voltage signals. In Fig. 3.5(a), the in-phase 3ω transfer function, $X_{3\omega}$, maintains its magnitude up to around 100 Hz before approaching zero, because a driving frequency less than 100 Hz provides enough time for the cantilever to reach a thermal equilibrium with the environment: see Chapter 2. Since $X_{3\omega} = -\mathrm{Re}[Z_c(2\omega)]/4$ and $Y_{3\omega} = -\mathrm{Im}[Z_c(2\omega)]/4$ [29], the decrease of $X_{3\omega}$ and $Y_{3\omega}$ magnitudes with increasing temperature indicates that the cantilever thermal impedance decreases with temperature. The peak location of $Y_{3\omega}$ moves to a smaller frequency as temperature increases, which implies that the propagation speed of the thermal information along the cantilever becomes slower at high temperatures due to increasing phonon scattering rate.

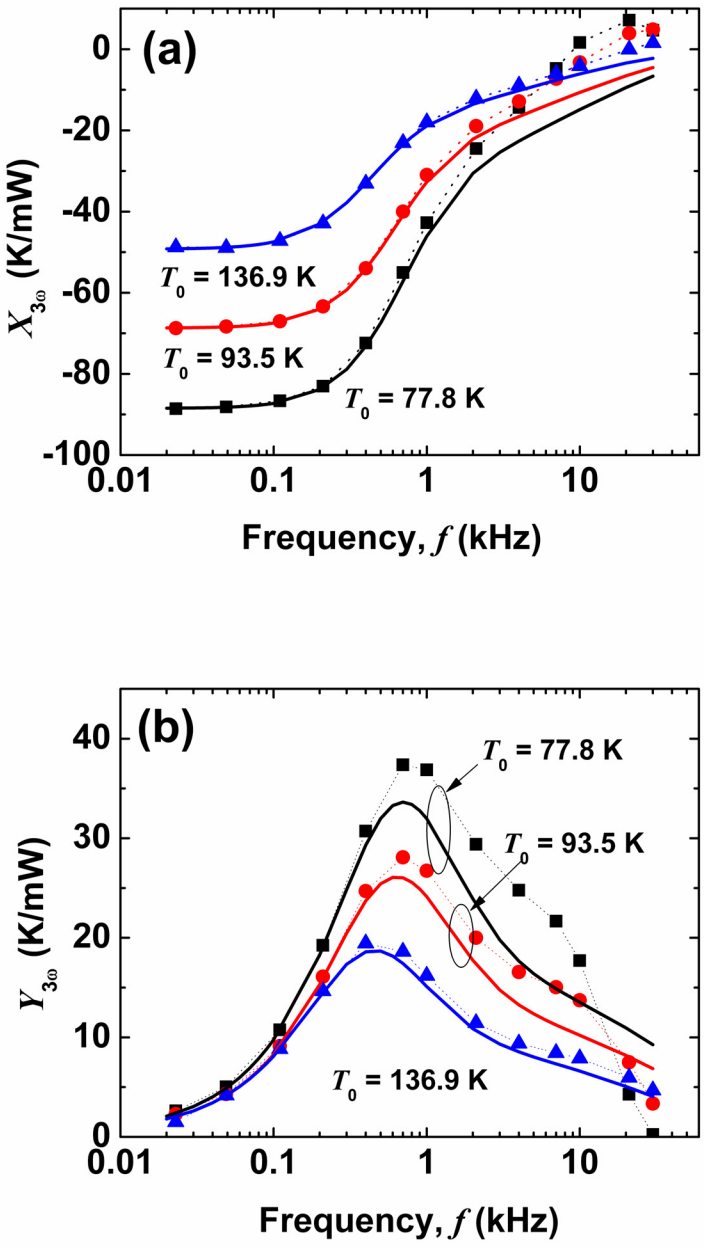

Figure 3.5 The electrical transfer functions converted from the 3ω cantilever voltage for different stage temperatures. (a) The in-phase electrical transfer functions and (b) out-of-phase transfer functions are plotted and compared with the calculation, which are plotted with solid curves.

The calculated electrical transfer functions are plotted together as solid curves in Fig. 3.5. The calculation and the measurement are in excellent agreement at low frequencies, but deviate at high frequencies. The deviation could be explained with two reasons. First, $X_{3\omega}$ and $Y_{3\omega}$ can be modulated by the electrical impedance at high frequencies. The deviation frequency of $X_{3\omega}$ at 77.8 K is approximately 1 kHz, coincident with 2 kHz at which the out-of-phase 1ω voltage in Fig. 3.4(b) starts to change: the 3ω signal reflects the thermal response at 2ω. Moreover, the calculation and the measurement agree much better at higher stage temperature, being an additional evidence of the signal modulation because the impedance effect is pushed to high frequencies as temperature increases. Another possible reason of the deviation is that the modeling did not consider a depletion region between the heater and the thermal constriction, which may affect the high frequency thermal response of the cantilever. Huge difference of the carrier concentration at the heater boundary can enhance the scattering rate in a small depletion region, forming a "hot spot" whose thermal response spectrum is located at high frequencies. A shoulder observed in measured $Y_{3\omega}$ at around 10 kHz, but not in calculated $Y_{3\omega}$, might be due to the presence of this depletion region. The depletion region effects should be investigated as future research and will not be further discussed here.

Despite the deviation between the calculation and the measurement at high frequencies, good overall agreement enables the extraction of cantilever thermophysical properties. Particularly, the properties of the heavily doped leg region can be obtained through the fitting process to the measurements. Even though the electrical resistance is dominated by the heater region, the thermal resistance of the cantilever mostly depends

on the heat conduction through the leg. Thus, thermal conductivity of the leg region and the specific heat (or thermal diffusivity) will determine the cantilever thermal transfer function, especially at low frequencies. Due to the small size of the heater and relatively large thermal conductivity of lightly doped silicon, the thermal behavior of the cantilever is not sensitive to the thermal conductivity of the heater region. The thermal conductivity at the heater is not adequate as a fitting parameter. Instead, thermal conductivity of the heater was taken from literature [31] considering the cantilever thickness [32]. Specific heat of the heater region was assumed to be the same as that of the leg region. Figures 3.6(a) and (b) respectively show the thermal conductivity and the specific heat of the leg region. Compared to the thermal conductivity shown in the inset as a reference [33], the leg thermal conductivity is around a half of the reference value, and its peak position is shifted to higher temperature. These differences are mainly due to the heavy doping concentration (4.3×10^{20} cm^{-3}) and thin cantilever thickness (0.59 μm): phonon-carrier and phonon-impurity scattering increase with doping level [34] while phonon-boundary scattering increases as the layer thickness decreases [32]: the estimated phonon mean free path at temperature range being considered is comparable to the cantilever thickness, reducing the thermal conductivity by nearly 50 %. As shown in Fig. 3.6(b), the specific heat of the cantilever leg is very close to that of pure and bulk silicon [35]. A small increase of the specific heat from that of pure silicon is expected because the Debye temperature of silicon slightly decreases with doping level [36]: the decrease of the Debye temperature Θ_D enhances the specific heat by $C \propto (T/\Theta_D)^3$ when temperature is low (i.e., $T/\Theta_D < 50$) [37]. The successful extraction of thermophysical properties of the cantilever indicates that the heated cantilever structure could be used more broadly

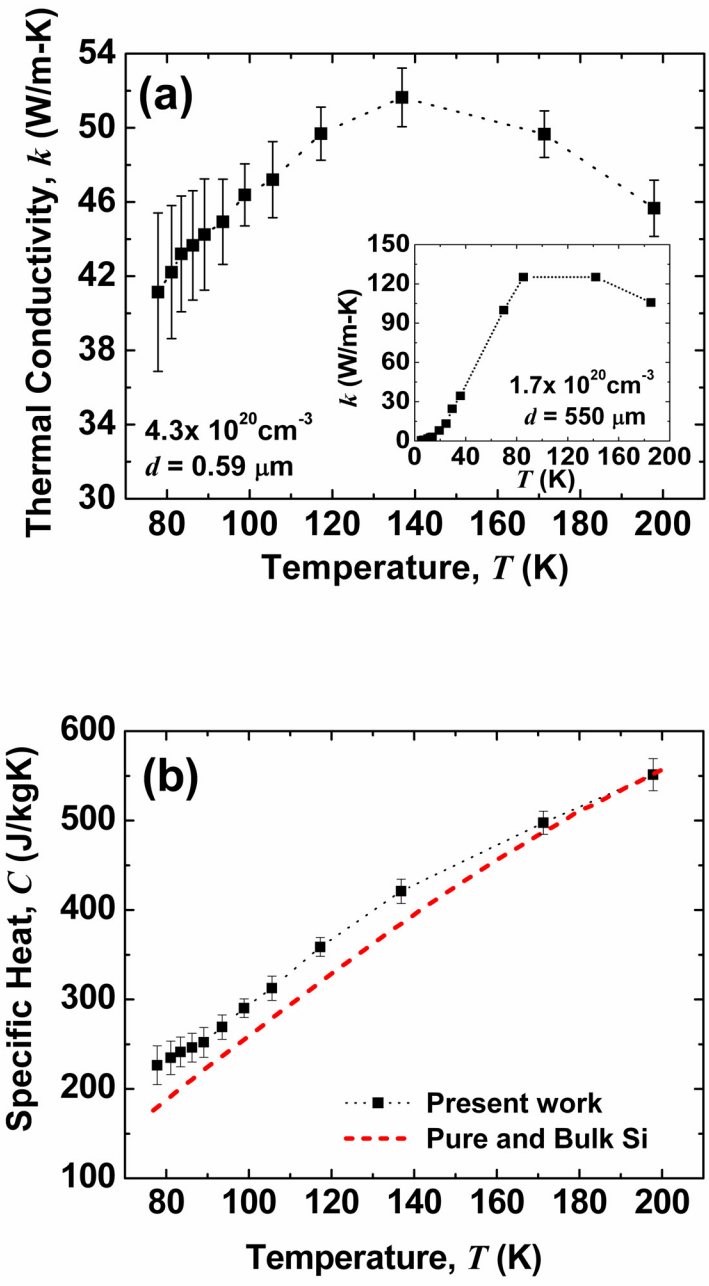

Figure 3.6 Thermophysical properties extracted from the 3ω cantilever voltage measurement. (a) The thermal conductivity and (b) the specific heat of the leg region are plotted as a function of temperature. For comparison, the thermal conductivity of phosphorus doped silicon with a different doping concentration and thickness, which is measured elsewhere [33], is plotted together in (a). The specific heat of pure and bulk silicon is plotted in (b) for comparison.

for thermophysical property measurements. The cantilever structure could have an advantage over other approaches, since uncertainties associated with the finite thermal conductance of conventional metal-deposited apparatus [28, 32] can be eliminated. Thermal conductance measurements have been previously reported for suspended, doubly-clamped polysilicon beams [38], but this chapter extends the technique to periodic measurements, low temperature, and combines modeling with measurements.

The uncertainties in the property extraction, which are estimated to be ±5.4 % for the thermal conductivity and ±5.2 % for the specific heat on average, are combinations of the uncertainties of the TCR, the thickness of the cantilever, and the measurement of harmonic cantilever voltage and other electrical properties. The relatively large uncertainties at low temperatures are mostly due to the uncertainty of the TCR. The cantilever resistance at low temperature varies dramatically with temperature, changing the TCR significantly even with a small uncertainty of 0.1 % in the resistance measurement. Another source of uncertainty lies in the extraction procedure, as the modeled transfer functions devastate from the measurement.

From the obtained thermophyscial properties, the thermal diffusion time can be determined from $\tau = 4L^2/\alpha$, where $2L$ is the whole cantilever length: since the anchor region experiences little temperature rise during heating, only heater, thermal constriction, and leg regions are considered as the cantilever. Figure 3.7 shows the diffusion time for different temperatures. The increase of the diffusion time with temperature is attributed to the decreasing thermal diffusivity, shown in the inset. Considering the physical meaning of the diffusion time, which is the time taken for the

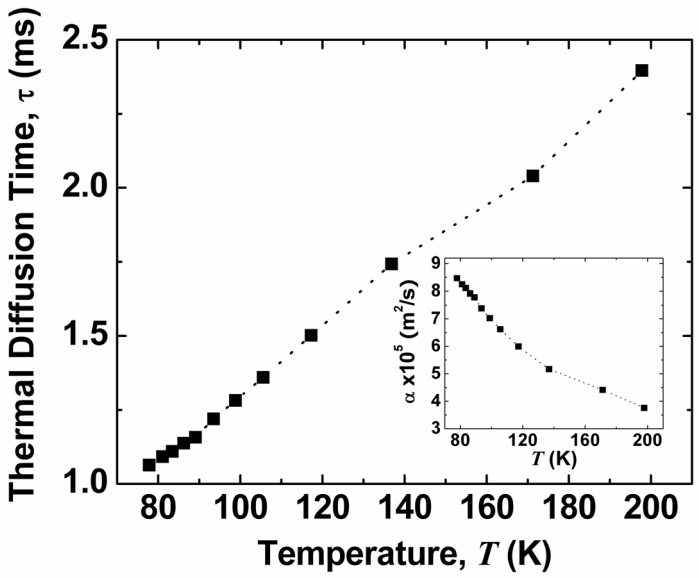

Figure 3.7 Thermal diffusion time as a function of temperature. The inset represents the measured thermal diffusivity.

thermal information to be diffusively delivered throughout the cantilever, the increasing diffusion time with temperature represents that the propagation speed of the thermal information along the cantilever decreases with increasing temperature. The estimated diffusion time is the same order of the settling time constant in Chapter 2, indicating that the diffusion time is also the time needed for the cantilever to reach thermal equilibrium with the environment.

Figures 3.8(a) and (b) show the calculated real and imaginary components of Fourier-transformed temperature oscillation $\Theta_\omega(x,\omega)$, or in-phase and out-of-phase temperature, along the cantilever for different heating frequencies. Θ_ω is nondimensionalized with the magnitude of temperature oscillation at the free end. As shown in Fig. 3.5, the temperature oscillation magnitude decreases with increasing

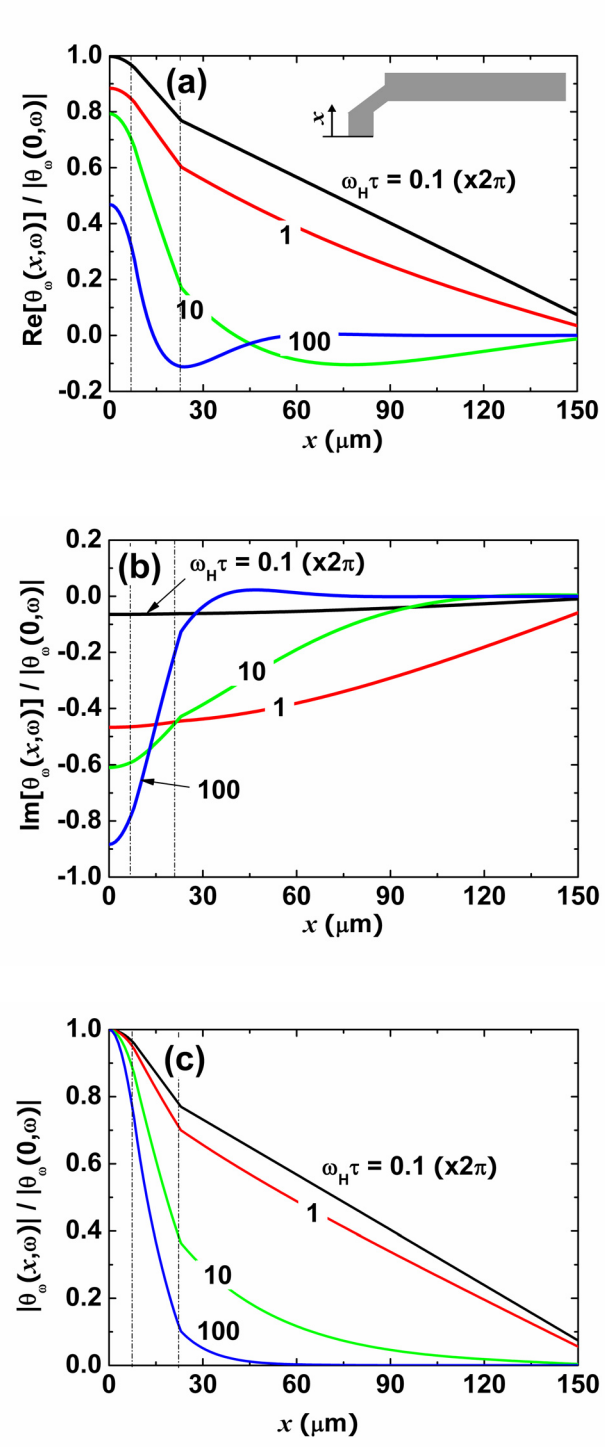

Figure 3.8 Temperature distributions along the cantilever for different frequencies. (a) The in-phase temperature along the cantilever is nondimensionalized with the temperature oscillation amplitude at $x = 0$ and plotted for four different frequencies. Two dash-dot lines distinguish the heater, thermal constriction, and leg region. (b) The out-of-phase temperature is plotted for the same frequencies as (a). (c) The amplitude of temperature oscillation along the cantilever shows the restriction of the thermal behavior within the heater and thermal constriction region at high frequency.

frequency, indicating that the actual temperature oscillation becomes smaller as the frequency increases. The dash-dot lines in the figures distinguish the heater, thermal constriction, and leg regions. When the frequency is slow (i.e., $\omega_H \tau = 0.1$), the temperature distribution is in phase and linear along the leg, because the slow frequency provides enough time for the cantilever to thermally respond to the power oscillation and diffuse the thermal information along the whole cantilever. As the frequency increases and exceeds the diffusion time constant, the cantilever response becomes out of phase and restricted within the heater and thermal constriction regions. This out-of-phase shift represents the considerable phase lag between power oscillation and corresponding cantilever thermal response: the cantilever cannot instantaneously respond to the fast power oscillation. Fast power oscillation beyond the diffusion time constant also prevents the thermal information from propagating to the opposite end of the cantilever. When $\omega_H \tau = 100$, for example, both the in-phase and out-of-phase temperature becomes zero at around $x = 50$ μm, which is only one third of the cantilever length. Moreover, significant temperature change occurs at the thermal restriction region, suggesting that optimum design of the thermal constriction region can restrict the high frequency thermal behavior of the cantilever within a small region. The restriction of the cantilever thermal response is reconfirmed in Fig. 3.8(c), which shows the distribution of temperature oscillation magnitude along the cantilever for different frequencies.

3.5 Conclusion

This work investigates the electrical and thermal responses of a heated microcantilever at low temperatures to extend its use in a cryogenic environment. The

cantilever resistance increases for decreasing cantilever temperature, due to carrier freezing and the decrease of the mobility. The steady-heating cantilever characterization reveals that the cantilever heater temperature can increase above 300 K when the environment is still at liquid nitrogen temperature. Under periodic-heating operation, the electrical impedance of the cantilever significantly distorts the 1ω cantilever voltage at high frequencies and complicates the thermal analysis. To ease the thermal analysis, electrical and thermal transfer functions of the cantilever were developed. The thermal conductivity and specific heat of the leg region were obtained by comparing the transfer functions with the measurements. The cantilever response at high frequencies becomes out of phase and is restricted within the heater and thermal constriction regions. The results obtained here clearly depict the cantilever electrical and thermal behavior at low temperature, which is critical for a safe and efficient cantilever operation in cryogenic environments.

3.6 References

[1] Z. F. Shao and Y. Y. Zhang, "Biological cryoatomic force microscopy: a brief review," *Ultramicroscopy*, vol. 66, pp. 141-152, 1996.

[2] A. Radenovic, E. Bystrenova, L. Libioulle, M. Taborelli, J. A. DeRose, and G. Dietler, "A low-temperature ultrahigh vacuum atomic force microscope for biological applications," *Review of Scientific Instruments*, vol. 74, pp. 1022-1026, 2003.

[3] A. Radenovic, E. Bystrenova, L. Libioulle, F. Valle, G. T. Shubeita, S. Kasas, and G. Dietler, "Characterization of atomic force microscope probes at low temperatures," *Journal of Applied Physics*, vol. 94, pp. 4210-4214, 2003.

[4] J. C. Bischof, "Quantitative measurement and prediction of biophysical response during freezing in tissues," *Annual Review of Biomedical Engineering*, vol. 2, pp. 257-288, 2000.

[5] J. Lee, T. L. Wright, M. R. Abel, E. O. Sunden, A. Marchenkov, S. Graham, and W. P. King, "Thermal conduction from microcantilever heaters in partial vacuum," *Journal of Applied Physics*, vol. 101, 014906, 2007.

[6] D. G. Cahill, "Thermal conductivity measurement from 30 to 750 K: the 3ω method," *Review of Scientific Instruments*, vol. 61, pp. 802-808, 1990.

[7] J. Lee, T. Beechem, T. L. Wright, B. A. Nelson, S. Graham, and W. P. King, "Electrical, thermal, and mechanical characterization of silicon microcantilever-heaters," *Journal of Microelectromechanical Systems*, vol. 15, pp. 1644-1655, 2006.

[8] M. Finetti, R. Galloni, and A. M. Mazzone, "Influence of impurities and crystalline defects on electron-mobility in heavily doped silicon," *Journal of Applied Physics*, vol. 50, pp. 1381-1385, 1979.

[9] S. S. Li and W. R. Thurber, "Dopant density and temperature-dependence of electron-mobility and resistivity in *n*-type silicon," *Solid-State Electronics*, vol. 20, pp. 609-616, 1977.

[10] N. D. Arora, J. R. Hauser, and D. J. Roulston, "Electron and hole mobilities in silicon as a function of concentration and temperature," *IEEE Transactions on Electron Devices*, vol. 29, pp. 292-295, 1982.

[11] D. B. M. Klaassen, "A unified mobility model for device simulation - I. Model-equations and concentration-dependence," *Solid-State Electronics*, vol. 35, pp. 953-959, 1992.

[12] S. M. Sze, *Physics of Semiconductor Devices*, 2nd ed., New York: Wiley, 1981.

[13] N. W. Ashcroft and N. D. Mermin, *Solid State Physics*, Philadelphia: Saunders College, 1976.

[14] K. F. Brennan, *The Physics of Semiconductors: with Applications to Optoelectronic Devices*, Cambridge ; New York: Cambridge University Press, 1999.

[15] D. B. M. Klaassen, "A unified mobility model for device simulation - II. Temperature-dependence of carrier mobility and lifetime," *Solid-State Electronics*, vol. 35, pp. 961-967, 1992.

[16] F. Mousty, P. Ostoja, and L. Passari, "Relationship between resistivity and phosphorus concentration in silicon," *Journal of Applied Physics*, vol. 45, pp. 4576-4580, 1974.

[17] T. T. Mnatsakanov, M. E. Levinshtein, L. I. Pomortseva, and S. N. Yurkov, "Universal analytical approximation of the carrier mobility in semiconductors for a wide range of temperatures and doping densities," *Semiconductors*, vol. 38, pp. 56-60, 2004.

[18] J. S. Blakemore, *Semiconductor Statistics*, Oxford, New York: Pergamon Press, 1962.

[19] T. K. Gaylord and J. N. Linxwiler, "Method for calculating Fermi energy and carrier concentrations in semiconductors," *American Journal of Physics*, vol. 44, pp. 353-355, 1976.

[20] C. D. Thurmond, "Standard thermodynamic functions for formation of electrons and holes in Ge, Si, GaAs, and GaP," *Journal of the Electrochemical Society*, vol. 122, pp. 1133-1141, 1975.

[21] W. Kuzmicz, "Ionization of impurities in silicon," *Solid-State Electronics*, vol. 29, pp. 1223-1227, 1986.

[22] T. F. Lee and T. C. Mcgill, "Variation of impurity-to-band activation energies with impurity density," *Journal of Applied Physics*, vol. 46, pp. 373-380, 1975.

[23] R. M. Dickstein, S. L. Titcomb, and R. L. Anderson, "Carrier concentration model for *n*-type silicon at low temperatures," *Journal of Applied Physics*, vol. 66, pp. 2437-2441, 1989.

[24] G. L. Pearson and J. Bardeen, "Electrical properties of pure silicon and silicon alloys containing boron and phosphorus," *Physical Review*, vol. 75, pp. 865-883, 1949.

[25] L. Shi, D. Y. Li, C. H. Yu, W. Y. Jang, D. Y. Kim, Z. Yao, P. Kim, and A. Majumdar, "Measuring thermal and thermoelectric properties of one-dimensional

nanostructures using a microfabricated device " *Journal of Heat Transfer*, vol. 125, pp. 881 - 888, 2003.

[26] T. Borca-Tasciuc, A. R. Kumar, and G. Chen, "Data reduction in 3ω method for thin-film thermal conductivity determination," *Review of Scientific Instruments*, vol. 72, pp. 2139-2147, 2001.

[27] A. Jacquot, B. Lenoir, A. Dauscher, M. Stolzer, and J. Meusel, "Numerical simulation of the 3ω method for measuring the thermal conductivity," *Journal of Applied Physics*, vol. 91, pp. 4733-4738, 2002.

[28] L. Lu, W. Yi, and D. L. Zhang, "3ω method for specific heat and thermal conductivity measurements," *Review of Scientific Instruments*, vol. 72, pp. 2996-3003, 2001.

[29] C. Dames and G. Chen, "1ω, 2ω, and 3ω methods for measurements of thermal properties," *Review of Scientific Instruments*, vol. 76, 124902, 2005.

[30] H. S. Carslaw and J. C. Jaeger, *Conduction of Heat in Solids*, 2nd ed., Oxford,: Clarendon Press, 1959.

[31] D. Fortier and K. Suzuki, "Effect of *p*-donors on thermal phonon scattering in Si," *Journal De Physique*, vol. 37, pp. 143-147, 1976.

[32] W. J. Liu and M. Asheghi, "Thermal conductivity measurements of ultra-thin single crystal silicon layers," *Journal of Heat Transfer*, vol. 128, pp. 75-83, 2006.

[33] G. A. Slack, "Thermal conductivity of pure and impure silicon, silicon carbide, and diamond," *Journal of Applied Physics*, vol. 35, pp. 3460-3466, 1964.

[34] M. Asheghi, K. Kurabayashi, R. Kasnavi, and K. E. Goodson, "Thermal conduction in doped single-crystal silicon films," *Journal of Applied Physics*, vol. 91, pp. 5079-5088, 2002.

[35] Y. S. Touloukian and E. H. Buyco, *Specific Heat : Metallic Elements and Alloys*, vol. 4, New York,: IFI/Plenum, 1970.

[36] R. W. Keyes, "Electronic effects in specific heat of silicon," *Physical Review B*, vol. 12, pp. 2539-2540, 1975.

[37] C. L. Tien, A. Majumdar, and F. M. Gerner, *Microscale Energy Transport*, Washington, D.C.: Taylor & Francis, 1998.

[38] Y. C. Tai, C. H. Mastrangelo, and R. S. Muller, "Thermal-conductivity of heavily doped low-pressure chemical vapor-deposited polycrystalline silicon films," *Journal of Applied Physics*, vol. 63, pp. 1442-1447, 1988.

CHAPTER 4

TAPPING-MODE NANOTOPOGRAPHY USING A HEATED MICROCANTILEVER

While previous chapters have focused on the characterization of a heated microcantilever for its possible usage as a cantilever-based thermal sensor, this chapter proposes the application of the heated cantilever as an alternative topographic imaging tool, particularly in tapping-mode AFM operation. The electrical and thermal responses of the cantilever were investigated while the cantilever oscillated in free space or was in intermittent contact with a surface. The cantilever oscillates at its mechanical resonant frequency, 70.36 kHz, which is much faster than its thermal time constant of 300 μs, and so the cantilever operates in thermal steady state. The thermal impedance between the cantilever heater and the sample was measured through the cantilever temperature signal. Topographical imaging was performed on silicon calibration gratings of height 20 and 100 nm. The obtained topography sensitivity is as high as 200 μV/nm and the resolution is as good as 0.5 nm/$Hz^{1/2}$, depending on the cantilever power. The cantilever heating power ranges 0 - 7 mW, which corresponds to a temperature range of 25 - 700 °C. The imaging was performed entirely using the cantilever thermal signal and no laser or other optics was required. As in conventional AFM, the tapping mode operation demonstrated here can suppress imaging artifacts and enable imaging of soft samples.

4.1 Introduction

In most AFM configurations, displacements of a cantilever are optically measured by bouncing a laser off the cantilever. However, laser-deflection based AFM is not feasible in every situation, for example when large arrays of cantilevers are to be operated in parallel or when the system does not permit optical access. Alternative approaches to monitor the cantilever position are required.

One alternative to monitor the cantilever position is to measure heat flow from the probe. The first report of local probes that exploit heat flow to sense topography was performed with a profilometer tip affixed with a thermocouple [1]. The thermocouple temperature signal indicated the amount of heat flow between the tip and the surface, which was modulated by the distance between the tip and the sample. The thermal signal could thus be used as a feedback signal for measuring topography. The same sensing strategy is possible with heated microcantilevers, because the heated cantilever itself is a very sensitive thermometer [2]: in the case of the silicon probe, the temperature sensor was a thermistor rather than a thermocouple. Recent theoretical [3,4] and experimental [5] studies showed that heated AFM cantilevers can be used for imaging nanometer-scale surface topography with sensitivity that greatly exceeds that of the piezoresistive cantilever. The thermally-sensed topography was also suggested by Lee and Gianchandani [6] with a different type of scanning thermal probe. However, these previous studies have been strictly limited to contact-mode operation, and no published report has described the use of the heated cantilever in tapping-mode operation. As in conventional tapping-mode AFM [7-9], the use of a heated cantilever in tapping mode

would allow precise topographic imaging of soft samples while suppressing imaging artifacts.

This chapter explores the resolution and sensitivity of the tapping-mode thermally-sensed topography using a heated microcantilever. The cantilever electrical and thermal characteristics are monitored when the cantilever oscillates either in free space or in intermittent contact with a surface. The cantilever electrical signal is compared to the laser-deflection signal. Several important issues are highlighted regarding cantilever design and operation for tapping mode imaging.

4.2 Experiment

The concept of topography mapping using the cantilever thermal signal has been explained previously [5], and is briefly summarized here. When the heated cantilever is operated near a surface, most of the generated heat flows into the substrate. About half of the heat flows directly across the air gap, while the remainder flows into the cantilever legs, although most of the heat that flows into the legs eventually flows into the air and into the substrate. The heat flow from the cantilever is a strong function of the air gap [5], indicating that the cantilever heater temperature sensitively changes with the change of the air gap. As the heated cantilever scans over a substrate, topographical feature of the substrate changes the vertical displacement of the cantilever relative to the substrate, leading to the change of the cantilever heater temperature and, correspondingly, the cantilever resistance. Thus, monitoring the cantilever voltage as the heated cantilever scans the surface can provide the topographic image as the laser-deflection measurement does.

The experiment was performed in a commercial AFM platform (Asylum MFP-3D). Figure 4.1(a) illustrates the experimental setup of tapping mode topography using a heated microcantilever. The cantilever used in the experiment has the same geometry with that used in Chapters 2 and 3. While the cantilever scanned over a sample in tapping mode, the AFM controller provided a topographic image of the sample by modulating the oscillation amplitude of the cantilever measured with a position-sensitive photodiode detector (PSD) [7-9]. At the same time, the cantilever was operated in a Wheatstone bridge circuit, as shown in Fig. 4.1(b). When the electrical current flows through the bridge circuit, the cantilever dissipates the electrical power and increases the heater temperature. Since the cantilever resistance is dependent upon the heater temperature, measuring the voltage change between A and B, i.e., $\Delta V_{\mathrm{C}} = V_{\mathrm{A}} - V_{\mathrm{B}}$, provides the relative change of the cantilever heater temperature. Measuring ΔV_{C} during the raster scanning can thus provide thermally-sensed topography. In the experiment, 5 kΩ non-inductive resistors were used for the Wheatstone bridge.

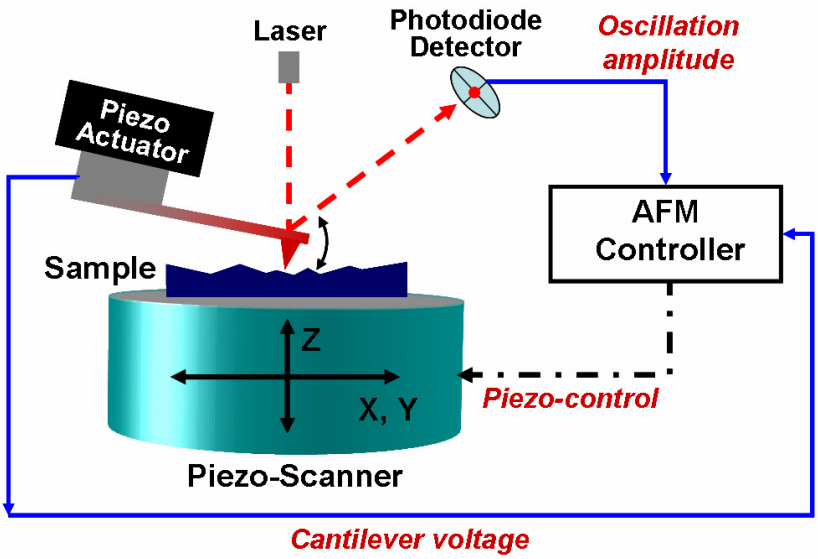

(a) Experimental Setup

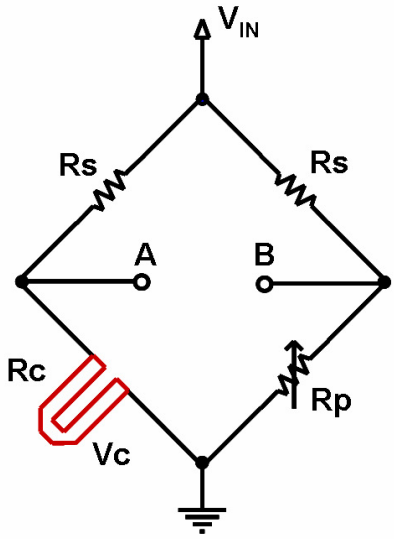

(b) Wheatstone Bridge

Figure 4.1 (a) The experimental setup for tapping mode topographical imaging using a heated microcantilever. While oscillating the cantilever, the AFM controller measures the laser deflection using a position-sensitive photodiode detector (PSD). The temperature-dependant voltage of the cantilever heater is measured simultaneously. (b) The use of Wheatstone bridge enhances the sensitivity of the cantilever voltage measurement. The cantilever voltage change can be obtained with $\Delta V_C = V_A - V_B$.

4.3 Results and Discussion

Before operating the cantilever in tapping mode, the cantilever mechanical properties of the cantilever must be understood. Figure 4.2 shows the thermal noise spectrum of the cantilever, which is the Fourier transformed laser-deflection signal of the unheated, free-standing cantilever far from the substrate. The random movement of air particles and their collisions to the cantilever give rise to the random fluctuation of the cantilever. As shown in the inset of Fig. 4.2, the fundamental resonance frequency can be obtained from the first peak position at 70.36 kHz. The other peaks at higher frequencies are due to higher oscillation modes or different oscillation patterns caused by the "U" shape of the cantilever. Another important property is the inverse optical lever sensitivity

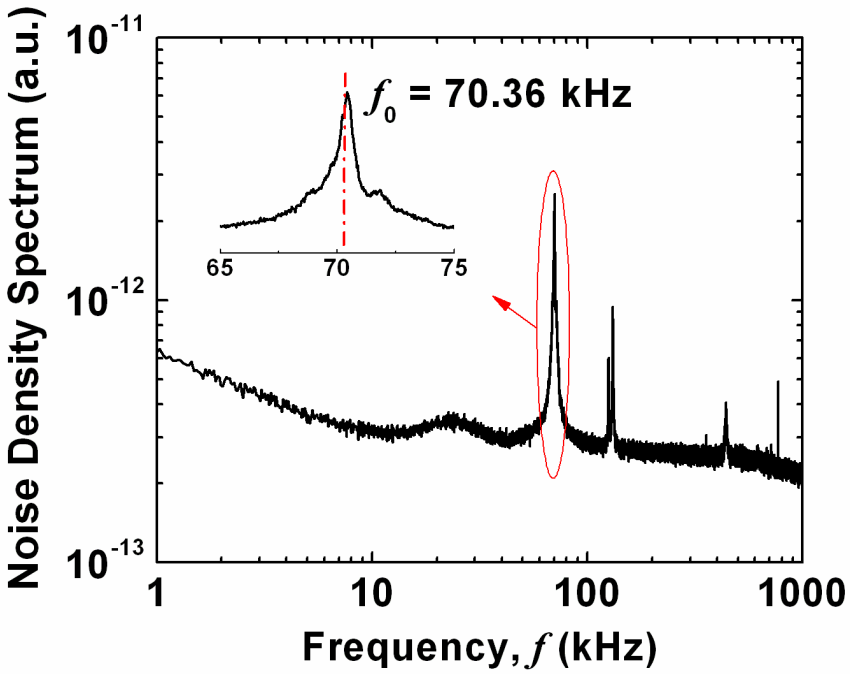

Figure 4.2 The mechanical characteristics of the cantilever when it is suspended in quiescent air, without interacting with the substrate. The noise density spectrum of the cantilever provides the fundamental mechanical resonance frequency of the cantilever.

(InvOLS), which is a parameter that converts laser-deflection signal to the oscillation amplitude. The InvOLS can be obtained from a slope of laser-deflection signal against the change of the *z*-direction piezo-scanner when the cantilever is in contact with the substrate. The InvOLS of the cantilever used in the experiment was 330 nm/V. The driving frequency for tapping mode was chosen as 69.5 kHz, close to the resonance frequency.

Electrical characterization of the cantilever is also necessary for the topography measurement. Figure 4.3(a) shows the cantilever resistance as a function of the total input voltage when the cantilever is suspended in quiescent air, without interacting with the substrate. The cantilever resistance first increases with increasing input voltage because of the decreasing electrical mobility of doped silicon with temperature. At 10 V input voltage, however, the cantilever resistance begins to decrease because the thermally generated intrinsic carriers outnumber the background doped carriers. This decreasing resistance is a characteristic of the thermal runaway behavior, which is typically observed in doped silicon devices [10]. To see any thermal effect on the cantilever due to its oscillation, the cantilever was characterized when it was in oscillation with the frequency of 69.5 kHz, and compared with the characterization result when the cantilever was steady: the two cases are nearly identical. Figure 4.3(b) shows more details of the effect of cantilever oscillation on the cantilever signal with the cantilever voltage spectrum measured with a spectrum analyzer. As shown in the inset of Fig. 4.3(b), there exists a peak in the cantilever voltage spectrum at the driving frequency, indicating that the cantilever voltage oscillates due to the mechanical oscillation of the cantilever. The peak value of 140 μV-rms at zero input voltage suggests that a part of the peak signal is

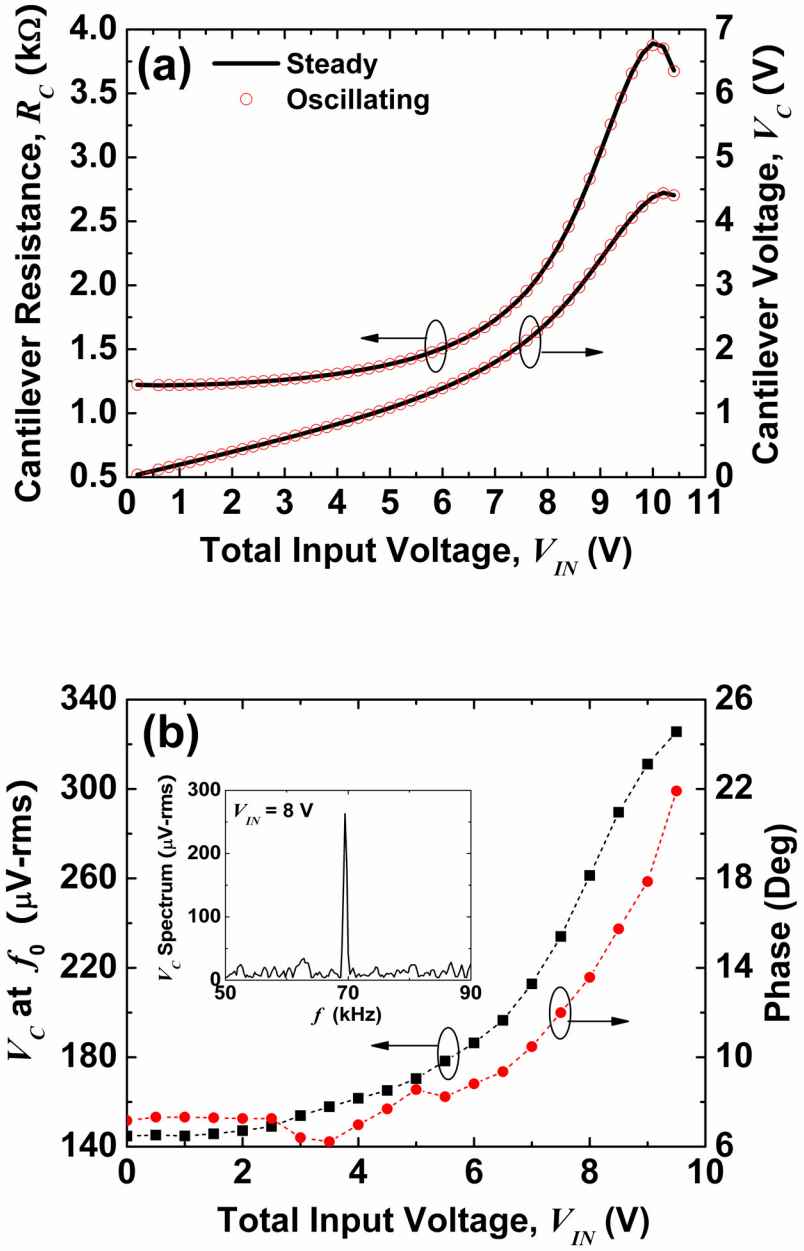

Figure 4.3 The effect of mechanical oscillation of the cantilever on the cantilever thermal response. (a) The cantilever resistance curves as a function of the input voltage when it is suspended in steady and in oscillation. The cantilever resistance nonlinearly increases with the increase of the total input voltage. The DC cantilever thermal response is nearly the same for the case of cantilever oscillation held steady. (b) Due to the cantilever oscillation, the spectrum of the cantilever voltage shows a peak at the dithering frequency at 69.5 kHz. This peak is however less than 0.01 % of the total cantilever voltage.

attributed to the noise pickup from the piezo-actuator that is shaking the cantilever. As the input voltage increases, the peak value increases in a very similar manner to the DC cantilever voltage in Fig. 4.3(a), implying that the cantilever is thermally affected by the cantilever oscillation. However, this thermal effect of the cantilever oscillation can be ignored because the peak value is negligibly small compared to the DC cantilever voltage.

Such a negligible oscillation effect on the cantilever thermal behavior can be explained with two reasons. The first reason is due to the fast cantilever oscillation with small amplitude. During the measurement, the oscillation frequency was 69.5 kHz, and the oscillation amplitude was 1.5 V in laser-deflection signal, or 495 nm from the invOLS. Even though the cantilever oscillation may agitate the surrounding air and thus change the heat transfer rate to the air, such a small and fast oscillation will not have much effect on the cantilever behavior. The second reason is because the cantilever oscillates much faster than its thermal time constant. The thermal time constant of the heated cantilever was measured to be around 300 μs, which corresponds to 3.3 kHz in frequency. This frequency is much lower than the oscillation frequency of the cantilever, suggesting that the cantilever does not have enough time to thermally respond to the disturbance resulting from the cantilever oscillation.

Electrical characterization was performed when the cantilever was engaged to the substrate with different set points, V_{SET}. When the cantilever is operated in tapping mode, the set point defines the oscillation amplitude of the cantilever: a larger set point provides larger oscillation amplitude. Figure 4.4(a) shows the cantilever resistance curves as a function of the power dissipation of the cantilever. When compared to the off-

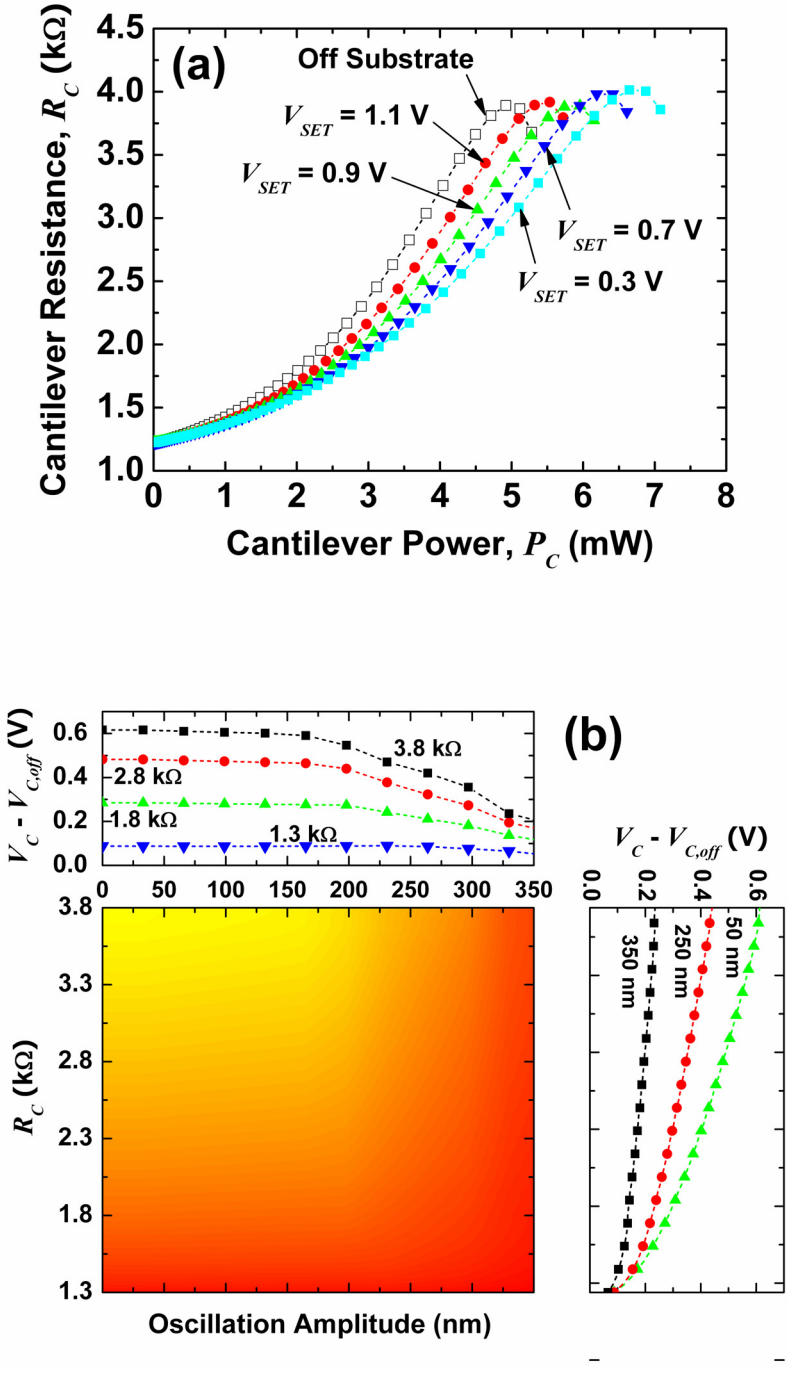

Figure 4.4 The effect of the substrate when approaching the heated cantilever to a silicon substrate. (a) As the cantilever approaches the substrate, more heat is transferred from the cantilever to the substrate. Thus, the DC characteristic curves shifts to the higher cantilever power. (b) The contour of the cantilever voltage as a function of the cantilever resistance and cantilever oscillation amplitude. The cantilever is fully engaged to the substrate when the cantilever amplitude decreases below 150 nm. From that point, the cantilever voltage does not change with further decrease of the oscillation amplitude.

substrate operation, the resistance curve shifts to the large cantilever power as the set point decreases. This shift is because more heat is transferred to the substrate as the cantilever-substrate gap is reduced. Finally, when the set point becomes 0.3 V, the resistance curve does not shift any more as the cantilever tip overcomes the air-damping and touches the substrate: true engagement occurs. Figure 4.4(b) shows the cantilever voltage change relative to that of the off-substrate characterization in Fig. 4.4(a), for various cantilever resistances and oscillation amplitudes. It should be noted that the cantilever oscillation amplitude is obtained from the set point and invOLS. From the horizontal profile in the top plot, it is clear that the cantilever voltage becomes saturated as the oscillation amplitude decreases below around 150 nm, or 0.4 V in set point. Thus, monitoring the cantilever voltage can provide the true engagement point without relying on the laser metrology. The vertical profile at the right plot shows the cantilever voltage as a function of the cantilever resistance for several fixed oscillation amplitudes. As expected, the cantilever voltage increases with increasing cantilever resistance, but the increasing trend is not linear.

Once the heated cantilever is fully engaged to the substrate, the topographic image of the sample can be obtained by monitoring the *z*-direction piezo-scanner that moves to maintain a tapping amplitude, and also by monitoring the cantilever voltage, ΔV_C, that varies due to the relative change of the cantilever-substrate gap. It should be noted that even though the cantilever tip taps the substrate in oscillation, the cantilever is in thermally steady state, not sensing the oscillation, due to its large thermal time constant. Thus, regardless of the operation mode, simply measuring ΔV_C during raster scanning enables the topographic imaging. As a proof of concept demonstration, Figs.

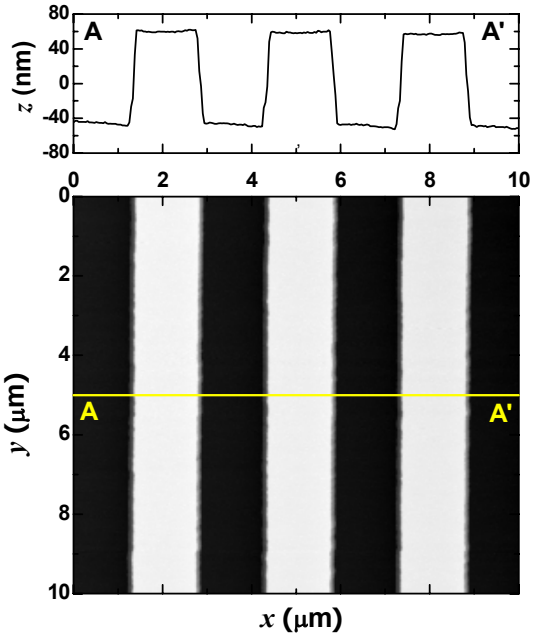

(a) Laser-deflection based topographic image

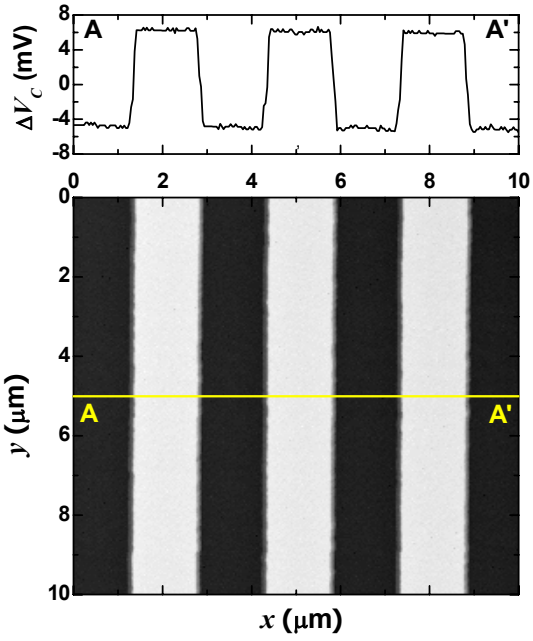

(b) Thermally-sensed topographic image

Figure 4.5 (a) The laser-deflection based topography and (b) the thermally sensed topography of the 100nm high Si gratings under the tapping mode. The total input voltage was 9 V. The thermally-sensed topography was achieved by monitoring the cantilever voltage signal during scanning.

4.5(a) and (b) topographic image of the standard silicon gratings of 100 nm height. While in tapping mode with the set point of 0.3 V, the total input voltage was maintained with 9 V that corresponded to the cantilever resistance of 2.07 kΩ and the cantilever power of 3.35 mW. Qualitatively, the thermally-sensed topographic image is almost the same as the laser-deflection based image except that the thermally-sensed topographic image has a little bit bigger noise, which will be discussed in the following paragraph. Quantitatively, the cantilever voltage changes from –4 mV to 6 mV while the grating height changes from –40 nm to 60 nm, yielding the sensitivity of 100 μV/nm when the sensitivity is defined as [4]

$$S = \frac{|\Delta V_C|}{\Delta z} \tag{4.1}$$

where S is the sensitivity, and Δz is the vertical displacement of the cantilever tip. The estimated sensitivity of 100 μV/nm is at least one order of magnitude better than that of the piezoresistive cantilever [3, 11, 12]. Moreover, when compared to the thermal topographic imaging in contact mode [5], Fig. 4.5(b) does not have artificial peaks at the edge of the gratings that were observed in contact mode images. Through the experiment, we believe that these artificial peaks in contact mode are because the other part of the cantilever besides the tip undesirably touches the grating edge due to the contact force and corresponding deformation of the cantilever, and can be prevented in tapping mode operation.

Since the thermally-sensed topography is based on the cantilever resistance change, the quality of topographic imaging depends on TCR of the cantilever. Figure 4.6(a) shows the cantilever resistance and qualitative change of topographical images for different input voltages when the set point is 0.3 V. It should be noted that only

representative topographic images are shown in the figure although the experiment was performed at many input voltages. Apparently, the nonlinear TCR yields different images for the same gratings. At low power dissipation up to 2.5 mW (i.e., $V_{IN} = 8$ V), obtained images do not represent the true geometry as the TCR is not big enough for good topography. Good images can be obtained only when the slope is greater than $0.6\ \Omega/\mu W$, which is shown with the line in Fig. 4.6(a). Thus, there exists an optimum cantilever operation range for a good thermal topography: for the heated cantilever used in the present study, the operation range is $4\ \text{mW} < P_C < 6.5\ \text{mW}$, or $9.5\ \text{V} < V_{IN} < 11.5$ V. If the cantilever is operated above the thermal runaway point, its negative resistance slope gives rise to the inversed topography.

For the evaluation of the thermally-topographic imaging methodology, Fig. 4.6(b) shows the sensitivity and resolution obtained from topographic images of 100 nm and 20 nm tall gratings. As expressed in Eq. (4.1), The sensitivity is defined as the step change in cantilever voltage for 1 nm vertical displacement of the cantilever. The resolution means the smallest step change that could be measured in a given integration time, and thus can be calculated as the noise divided by the sensitivity [4]. In contact mode, the noise is the combination of thermal noise and Johnson noise under the assumption that there is no artifact in the signal.[3] However, the dominant noise in tapping mode comes from the peak at the tapping frequency, as shown in Fig. 4.3(b). To estimate the noise, power spectral density of the peak at the tapping frequency was measured with a spectrum analyzer when the cantilever was engaged to the substrate. At lower input voltages, poor quality of topography is manifested with low sensitivity and bad resolution. As the input

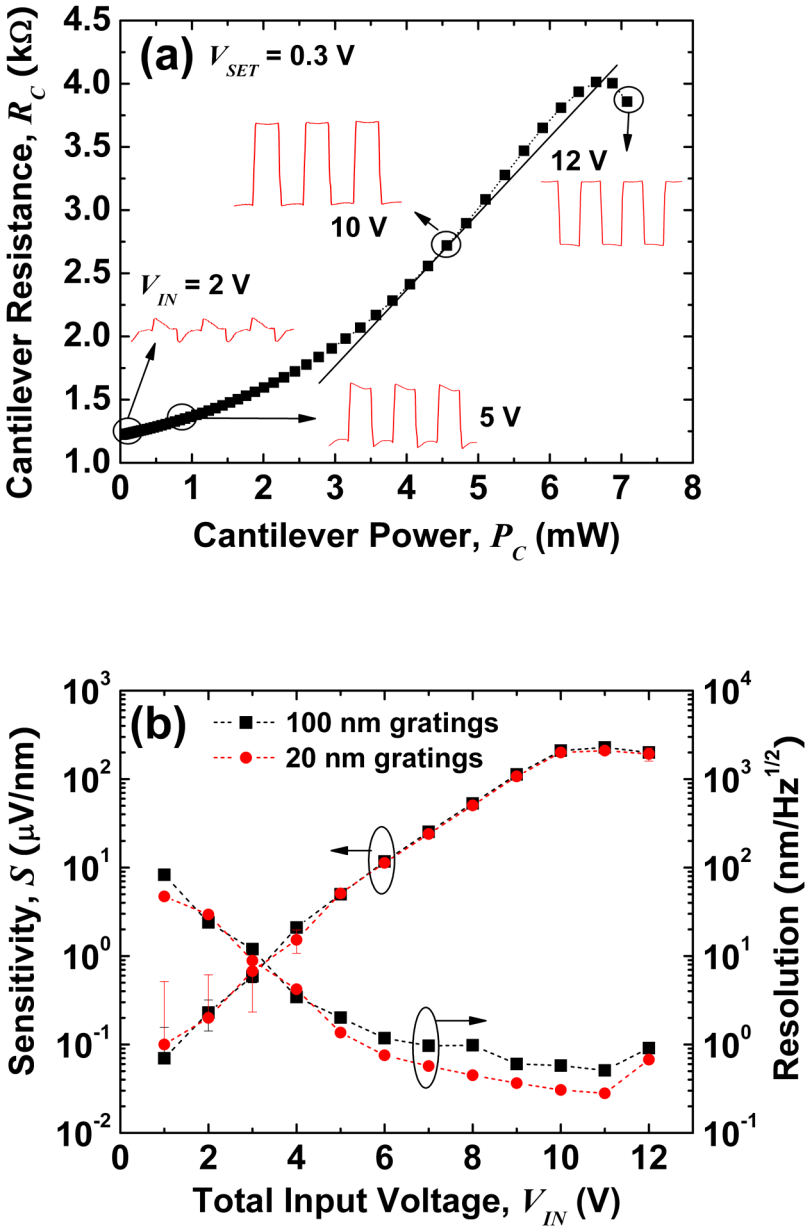

Figure 4.6 The sensitivity and resolution of thermally-sensed topography. (a) The cantilever resistance curve when the cantilever is engaged with the set point of 0.3 V. For lower cantilever power, the topographic image is distorted due to the poor sensitivity. Good images can be obtained at the high TCR region. When the cantilever is operated over the thermal runaway point, the topographic image is inversed due to the negative TCR. (b) The estimated sensitivity and resolution of the thermal topography metrology are obtained by scanning two silicon gratings. The sensitivity can be as high as 200 μV/nm while the resolution is lower than 1 nm/Hz$^{1/2}$.

voltage increases, however, the sensitivity becomes improved and finally saturated with around 200 μV/nm when the cantilever is operated above 10 V, which is consistent with the optimum operation range discussed earlier. This sensitivity curve shows a similar trend with the previous numerical study [4], except the simulated sensitivity has a sharp dip where the cantilever resistance becomes maximal. Comparison with Fig. 4.6(a) suggests that there should be a dip between 11 V and 12 V: it is technically not easy to observe the dip in experiment. The resolution also improves as the input voltage increases, realizing the sub nanometer resolution. However, the overall resolution is one order of magnitude worse than the simulation results performed in contact mode [4], as the peak noise at the tapping frequency is much larger than the thermally-induced intrinsic noises.

The obtained experimental results reveal several important issues that should be considered when designing a heated cantilever as a tapping mode thermally-topographic imaging tool. The first issue is the cantilever heater size. As mentioned earlier, the thermal topography can be realized by the heat transfer to the substrate and its sensitive change with the vertical displacement of the cantilever. Provided that over 90 % of the cantilever power is dissipated in the heater [13], the heater size has a dominant effect on the topographic imaging. If a feature size to be scanned is larger than the heater, the thermally-sensed topography will not be possible because the heater-substrate will not change. The cantilever tip height should be also carefully designed and fabricated. If the tip is too high, the sensitivity would not be good [4]. However, if the cantilever tip height is too small, the cantilever-substrate heat transfer might enter the ballistic regime, in which the heat transfer rate is no more dependent upon the gap width [14]: topographic

imaging could not be thermally obtained. The third issue to be considered is the thermal time constant of the cantilever. The successful thermally-sensed topography in the present study is attributed to the fact that the thermal time constant of the cantilever is larger than the inverse of the resonance frequency. Otherwise, the cantilever voltage would oscillate following the mechanical oscillation during scanning, complicating the accurate topography in tapping mode. The last issue is the doping level of the heater region. Whilst the large input voltage enhances the sensitivity, it also drastically increases the heater temperature and may damage the sample that is vulnerable to heat. This undesirable heating can be prevented by lowering the doping level of the heater region, as the lower doping concentration yields higher resistance slope and thus enhances the sensitivity at lower temperature [4]. However, the resolution will become worse due to its high intrinsic noise. It should be noted that all the design parameters discussed here are strongly coupled together. Their crosstalk complicates the optimum design of the heated cantilever for a thermal topographic tool, and we suggest that this is an important future study.

4.4 Conclusion

This work demonstrates tapping mode thermally-sensed topography imaging with a heated microcantilever. The sensitivity is as high as 200 μV/nm and the resolution is as good as 0.5 nm/$Hz^{1/2}$, which are comparable to or better than other approaches. By characterizing the cantilever with different set points, we showed that the full engagement point can be thermally determined without the aid of the optics. The thermally-sensed AFM can be completely realized from the engagement to the

topographic imaging without optical monitoring of the cantilever. The obtained results in the present study can be applied for the parallel deflection monitoring of cantilever arrays and even the development of portable AFM systems.

4.5 References

[1] C. C. Williams and H. K. Wickramasinghe, "Scanning thermal profiler," *Applied Physics Letters*, vol. 49, pp. 1587-1589, 1986.

[2] G. Binnig, M. Despont, U. Drechsler, W. Haberle, M. Lutwyche, P. Vettiger, H. J. Mamin, B. W. Chui, and T. W. Kenny, "Ultrahigh-density atomic force microscopy data storage with erase capability," *Applied Physics Letters*, vol. 74, pp. 1329-1331, 1999.

[3] W. P. King, T. W. Kenny, and K. E. Goodson, "Comparison of thermal and piezoresistive sensing approaches for atomic force microscopy topography measurements," *Applied Physics Letters*, vol. 85, pp. 2086-2088, 2004.

[4] W. P. King, "Design analysis of heated atomic force microscope cantilevers for nanotopography measurements," *Journal of Micromechanics and Microengineering*, vol. 15, pp. 2441-2448, 2005.

[5] K. J. Kim, K. Park, J. Lee, Z. M. Zhang, and W. P. King, "Nanotopographical imaging using a heated atomic force microscope cantilever probe," *Sensors and Actuators a-Physical*, 2006 (available online, doi:10.1016/j.sna.2006.10.052).

[6] J. H. Lee and Y. B. Gianchandani, "High-resolution scanning thermal probe with servocontrolled interface circuit for microcalorimetry-and other applications," *Review of Scientific Instruments*, vol. 75, pp. 1222-1227, 2004.

[7] Y. Martin, C. C. Williams, and H. K. Wickramasinghe, "Atomic force microscope force mapping and profiling on a sub 100-Å scale," *Journal of Applied Physics*, vol. 61, pp. 4723-4729, 1987.

[8] Q. Zhong, D. Inniss, K. Kjoller, and V. B. Elings, "Fractured polymer silica fiber surface studied by tapping mode atomic force microscopy," *Surface Science*, vol. 290, pp. L688-L692, 1993.

[9] R. Garcia and R. Perez, "Dynamic atomic force microscopy methods," *Surface Science Reports*, vol. 47, pp. 197-301, 2002.

[10] B. W. Chui, M. Asheghi, Y. S. Ju, K. E. Goodson, T. W. Kenny, and H. J. Mamin, "Intrinsic-carrier thermal runaway in silicon microcantilevers," *Microscale Thermophysical Engineering*, vol. 3, pp. 217-228, 1999.

[11] T. Gotszalk, P. B. Grabiec, and I. W. Rangelow, "A novel piezoresistive microprobe for atomic and lateral force microscopy," *Sensors and Actuators a-Physical*, vol. 123-24, pp. 370-378, 2005.

[12] I. Shiraki, Y. Miyatake, T. Nagamura, and K. Miki, "Demonstration of low-temperature atomic force microscope with atomic resolution using piezoresistive cantilevers," *Review of Scientific Instruments*, vol. 77, pp. 1-4, 2006.

[13] J. Lee, T. Beechem, T. L. Wright, B. A. Nelson, S. Graham, and W. P. King, "Electrical, thermal, and mechanical characterization of silicon microcantilever-heaters," *Journal of Microelectromechanical Systems*, vol. 15, pp. 1644-1655, 2006.

[14] J. B. Xu, K. Lauger, R. Moller, K. Dransfeld, and I. H. Wilson, "Heat transfer between two metallic surfaces at small distances," *Journal of Applied Physics*, vol. 76, pp. 7209-7216, 1994.

CHAPTER 5

HEAT TRANSFER BETWEEN A HEATED MICROCANTILEVER AND THE SUBSTRATE

In this chapter, heat transfer from a heated microcantilever to the substrate and the resultant temperature distributions are investigated. To this end, a four-point probe platinum resistive thermometer having a 140 nm spatial resolution has been fabricated on the SiO_2-coated silicon substrate. Estimated TCR of the thermometer is 0.0011 K^{-1}, approximately one third of the bulk value. When the heated cantilever scans over the thermometer, up to 70 % of the cantilever power is transferred to the substrate through the air, heating up the substrate. The maximum substrate temperature rise measured with the thermometer is around 7 K. From the force-displacement experiment, the cantilever-substrate effective contact conductance was estimated to be around 40 nW/K. The obtained results will help further understanding of thermal behavior of the heated cantilever during scanning and its effect on the substrate.

5.1 Introduction

As mentioned earlier in Chapter 1, applications of a heated microcantilever have diverged to a number of fields, such as data storage, nanolithography, nanoscale thermal analysis, and aforementioned thermally-sensed nanotopography. Since most of these applications make use of the thermal interaction between the heated cantilever and substrate, heat transfer between them should be well understood to further improve the

heated cantilever-based technology. Previously, many efforts have been made to understand the thermal, electrical, and mechanical behaviors of the heated cantilever in various operation conditions [1,2] and environments [3,4]. However, these studies have been limited to only the cantilever itself without taking into account the presence of the substrate. Even though some studies have investigated the heat transfer between the cantilever and substrate to improve the cantilever design for thermomechanical data storage [5] or nanotopography [6,7], no experimental investigation on the cantilever-to-substrate heat transfer has been reported.

Thermal energy transport at the very small length scale has been intensively studied along with the progress of the scanning thermal microscopy (SThM) [8]. SThM has realized nanoscale thermal metrology, for which microcantilevers having a temperature-sensitive tip have been developed and used in an AFM platform [9-11]. With a help of SThM, remarkable progress has been made on understanding complicated heat transfer at nanoscale contact and elucidating predominant heat transfer mechanisms and their thermal conductances [9,12-14]. However, accumulated knowledge from SThM cannot be directly applied to the heated cantilever-to-substrate heat transfer for several reasons. Compared to SThM microcantilevers, the most apparent difference is the presence of a relatively large heater, i.e., 8 μm × 16 μm. Thus, substantial amount of heat will be transferred from the heater to the substrate via air conduction [6]. Moreover, the heated cantilever is typically operated at high heater temperatures up to 1,000 K, which will significantly alter the involved heat transfer mechanisms. Thus, experimental investigation of the heat transfer between the heated cantilever and the substrate should be performed.

The objective of this work is to elucidate the heat transfer between the heated cantilever and the substrate. To this end, an on-substrate resistive thermometer having a sub-micron spatial resolution was fabricated. Section 5.2 describes the fabrication procedure of the thermometer, along with the detailed explanation of the experimental procedure. In Section 5.3, a semi-analytical modeling for the substrate temperature distribution is explained. Experimental results and the comparison with the calculation comprise the next section, which provides a detailed discussion of heat transfer from the cantilever to the substrate and the resultant temperature changes.

5.2 Experiment

In order to measure the substrate temperature, a thermometer that has a sub-micron spatial resolution should be fabricated. Recently, a gold/nickel thin film thermocouple with a sub-micron junction size has been fabricated to measure the substrate temperature rise due to electron-beam resist heating [15,16]. Although a thermocouple can achieve a very small spatial resolution, low sensitivity is a serious drawback of the thermocouple measurement. For example, the Seebeck coefficient of the thermocouple in Ref. [16] is only 6 to 7 μV/nm with around 10 % uncertainty: it will be very challenging to measure the temperature increase less than 10 K. Another disadvantage is the difficulty of the characterization. To the contrary, a resistive thermometer provides relatively high sensitivity and easiness of the characterization. Despite the sacrifice of the spatial resolution, the use of a resistive thermometer will thus mitigate practical difficulties in substrate temperature measurement.

In the present experiment, a thin-film platinum thermometer having a sub-micron sensing probe was fabricated. After growth of a 1 μm SiO_2 layer on a Si substrate of 500 μm thickness, platinum was e-beam evaporation deposited to make a thermometer pattern having the thickness of around 35 nm. A 5 nm alumina (Al_2O_3) layer was then deposited to electrically insulate the thermometer. A sub-micron sized thermometer probe was fabricated with a focused ion beam (FIB) milling process. Figure 5.1(a) shows a SEM image of the fabricated thermometer. The thermometer has a four wire configuration, with which the electrical resistance of the sensing probe can be measured with high accuracy. The width of each lead is 20 μm. Figure 5.1(b) and (c) also show SEM images of the sensing probe that are magnified from the top images. The length of the sensing probe is 29 μm, and the width is approximately 140 nm. Due to its negligibly small thermal resistance compared to the substrate and environment, the thermometer will not disturb the substrate temperature.

The experiment was performed in a commercial AFM platform (Asylum MFP-3D). The heated cantilever used in the experiment looks almost the same as that in Fig. 2.1(a), except its shorter leg length, i.e., 85 μm, and wider thermal constriction, i.e., 6.5 μm. Figure 5.2(a) illustrates the schematic diagram of the experimental setup. The AFM operation mode was chosen as tapping mode, or ac mode, since the thermometer is easily damaged by the contact force of the cantilever tip. While the cantilever scanned the thermometer sample in tapping mode, the AFM provided a topographical image of the sample from the optical signal from a position-sensitive photodiode detector (PSD). At the same time, the cantilever voltage was monitored. The mechanical resonance frequency of the cantilever used in this experiment was measured to be 75.6 kHz, which

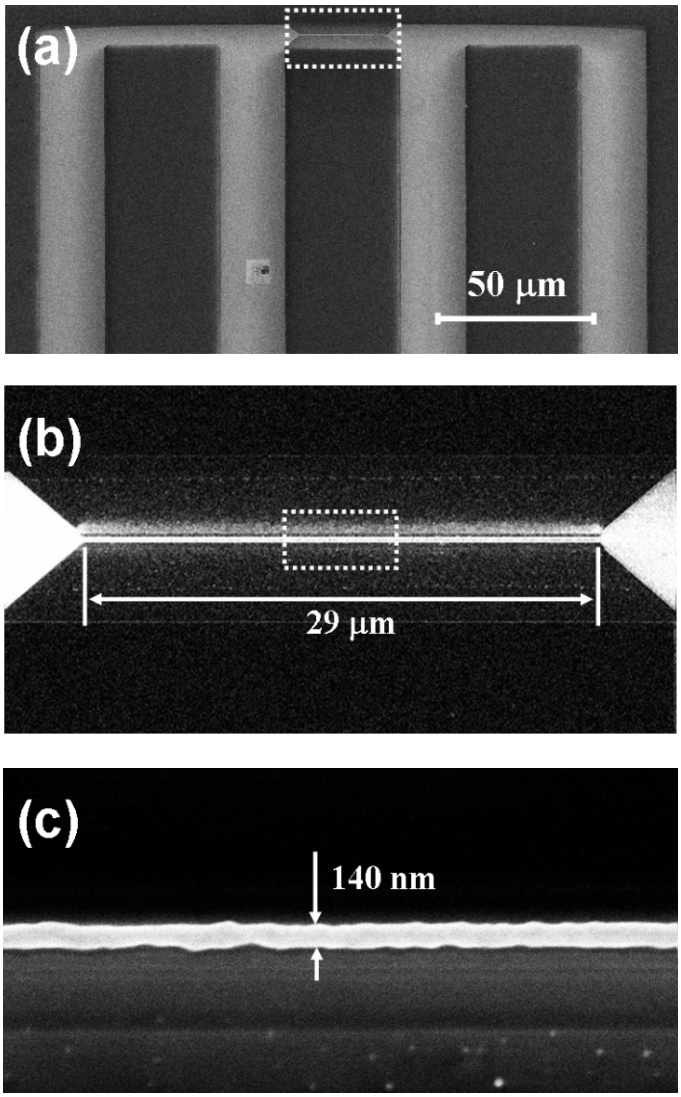

Figure 5.1 SEM image of the fabricated nanoscale platinum thermometer. (a) whole area of the thermometer sensing probe. Four legs denote the electrical leads: the electrical current flows through the outer two legs while the voltage drop across the inner legs is measured. (b) Magnified image of the rectangular mark of (a). The sensing probe length is measured to be 29 μm. (c) Magnified image of the rectangular mark of (b). The sensing probe width is measured to be 140 nm.

is much faster than its thermal time constant of around 300 μs. Thus, even in tapping mode, the cantilever voltage is steady [17] and can be easily measured without any frequency-domain instrumentation. The thermometer voltage was also simultaneously measured during the scanning, providing the thermometer resistance change. For the simultaneous measurement of the three signals, we used a multichannel analog-to-digital converter (ADC) embedded in the AFM controller that has a 16-bit resolution and input voltage range from -10 to 10 V.

Both the cantilever and thermometer signal were measured in bridge circuits to remove the DC-offset signals, which are approximately 1,000 times larger than the relative signal change. By removing the DC-offset, much higher resolution can be obtained in the measurement. Figure 5.2(b) illustrates the bridge circuits used in the experiment. The cantilever was operated in the Wheatstone bridge, in which the voltage of the cantilever was measured from the voltage difference between A and B, i.e., $\Delta V_C = V_B - V_A$. In order to simplify the post-analysis of the experimental results, total input voltage V_{IN} was feedback-controlled to maintain the cantilever resistance with a set value. A PCI-6052 data acquisition (DAQ) system was used to measure the voltage drops across the cantilever and the sense resistor while a Labview software was used to control V_{IN}. The data sampling rate was set to 2 kilosamples per second, considering the DAQ and computing speed in real-time control. The thermometer bridge circuit was modified from the Wheatstone bridge to be compatible with its four wire configuration. The voltage change of the sensing probe can be expressed from the voltage difference between C and D as $\Delta V_{TH} = 1.94(V_C - V_D)$ after the lead resistances are compensated. The resistance change of the sensing probe can thus be obtained from

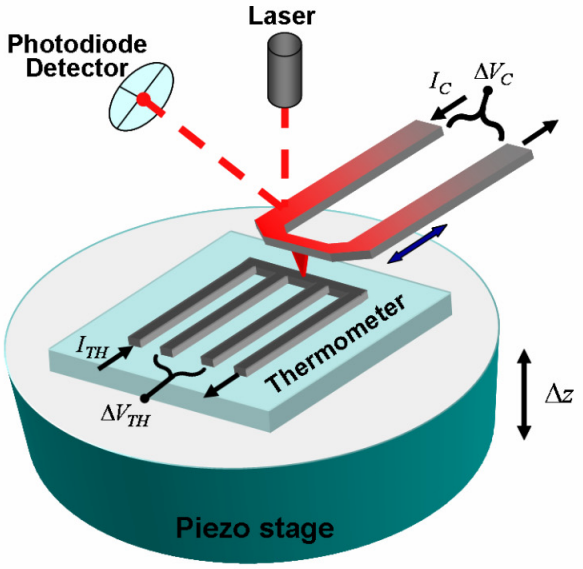

(a) Experimental Setup

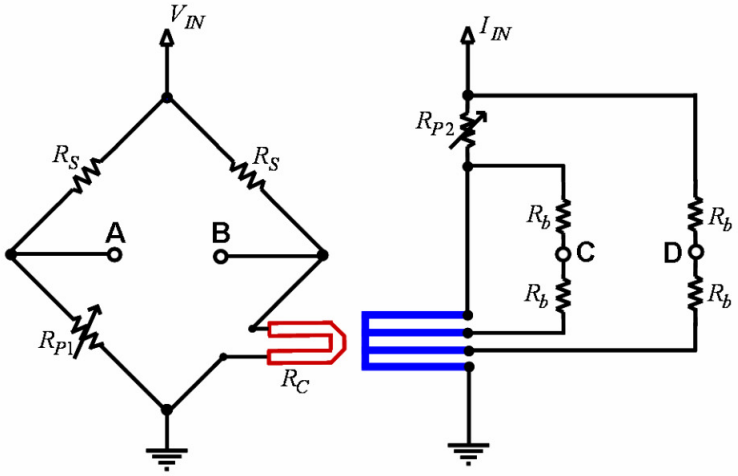

(b) Bridge Circuits

Figure 5.2 (a) The experimental setup in an AFM platform. While the cantilever scans the thermometer, the AFM controller simultaneously measures the thermometer topography, the cantilever voltage change, and the thermometer resistance change. (b) The use of bridge circuits enhances the measurement sensitivity by canceling out the large DC-offset. The cantilever voltage change can be obtained with $\Delta V_C = V_B - V_A$, whilst the thermometer voltage change can be obtained by $\Delta V_{TH} = 1.94(V_C - V_D)$.

$\Delta R_{TH} = \Delta V_{TH}(R_{P2}/V_{P2})$, where R_{P2} is the potentiometer resistance and V_{P2} is the voltage drop across the potentiometer. In the experiment, 1 kΩ and 5.16 kΩ resistors with 1 % tolerance were used for the cantilever and thermometer bridge circuits, respectively. In order to further enhance the ADC resolution of the thermometer voltage measurement, a differential amplifier was employed with $100\times$ gain.

5.3 Numerical Modeling

The coupling between the thermal and electrical responses of the heated cantilever and thermometer complicates the analysis of the experimental results, which can be substantially relieved by the appropriate numerical modeling. Previously, the thermal and electrical behaviors of the heated cantilever have been numerically studied when it is under the steady heating [1,3,18] and periodic heating [2]. However, all of them considered the heated cantilever only, assuming no thermal interaction with the substrate. Although some works included the heat transfer from the heated cantilever to the substrate [7,19], the assumption that the substrate maintains at room temperature has prevented further insight into the heat transfer to the substrate.

This section describes the calculation of the temperature distribution along the cantilever as well as the substrate when the cantilever is placed above the substrate with a small gap, as illustrated in Fig. 5.3. As for the cantilever, the present analysis adopts a steady one-dimensional (1-D) heat conduction model. The thermal resistance across the cantilever thickness and width is very small compared to that along or from the cantilever, validating the 1-D steady thermal modeling given by

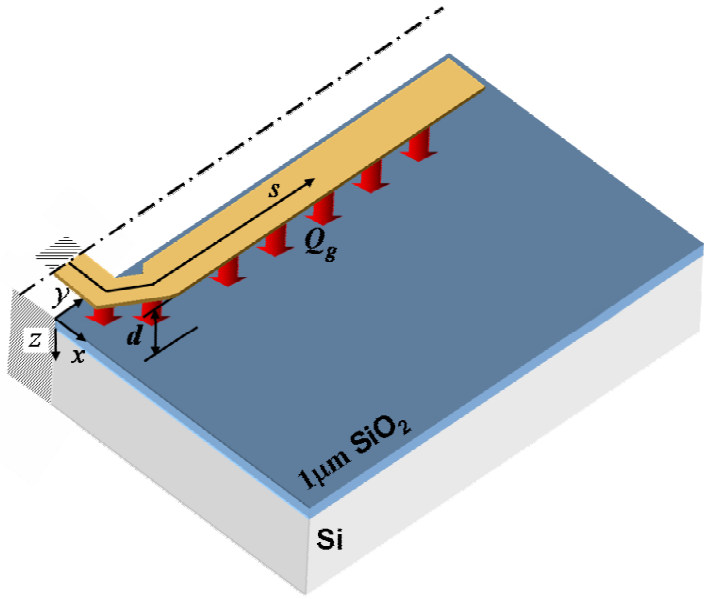

Figure 5.3 The schematic diagram of the cantilever and the substrate in the calculation. The cantilever-substrate gap is assumed to be in parallel, through which Q_g is transferred to the substrate. Temperature distributions of both the cantilever and the substrate are iteratively calculated until the calculation matches with the measurement.

$$\frac{d}{ds}\left(k_C A_C \frac{dT_C}{ds}\right) + g''' A_C - \sigma_a (T_C - T_\infty) - \sigma_g (T_C - T_S) = 0 \qquad (5.1)$$

where s is the axis along the cantilever, k_C is the thermal conductivity, A_C the cross sectional area, g''' the volume density of heat generation, σ_a and σ_g respectively the thermal conductance to the surrounding air and to the substrate, T_∞ the surrounding temperature, and T_S the substrate temperature. Due to the symmetry, only half of the cantilever was modeled with the adiabatic boundary condition at the free end. The opposite end was assumed to be fixed with the room temperature as the silicon base can be taken as a heat sink. σ_a was calculated from the heat transfer coefficient using $\sigma_a = h_a(w + 2\delta)$, where w is the cantilever width and δ is the cantilever thickness. The estimated heat transfer coefficient can be up to around 5,000 W/m^{2}K, depending on

temperature [2]. Since the cantilever-substrate gap is in the transition regime between the continuum and free molecular flow, σ_g is written as a function of the gap [20],

$$\sigma_g = \frac{w}{d}\frac{\bar{k}}{\Lambda}\left(\frac{1}{\Lambda}+\frac{C}{d}\right)^{-1} \tag{5.2}$$

where $\bar{k}$ is the effective thermal conductivity of a continuum gas bounded by parallel surfaces, Λ is the mean free path of air, C is the coefficient on the order of 1 that is estimated from rarefied gas dynamics for free molecular flow. The near-field thermal radiation was not considered here because the heat transfer rate due to the near-field radiation is less than 1 % of the air conduction at the cantilever-substrate gap in concern, i.e., around 1μm [21]. It should be noted that all the variables in Eq. (5.1) are position-dependent, necessitating a finite-difference numerical method for its calculation.

Computing the substrate temperature distribution is complicated because of its three-dimensional feature and the heat transfer from the "U" shaped cantilever. The best way to deal with these geometric complications might be the use of a finite-element numerical method. However, this method is computationally expensive, particularly when the iteration is involved in the calculation. The present analysis adopts a semi-analytical approach using a Green's function,

$$T_b(x,y,z) = T_\infty + \sum_i \frac{q''_{g,i}}{k_b}\iint_{A_i} G(x,y,z \mid x_i', y_i', 0)\,dx_i'\,dy_i' \tag{5.3}$$

Here, the index i denotes each node of the cantilever in the finite-difference scheme, k_b is the thermal conductivity of the substrate, $q''_{g,i} = \left[\sigma_g (T_C - T_S)/A\right]_i$ where T_S is the substrate surface temperature and A_i are respectively the heat flux and heat transfer area from the cantilever to the substrate at the i-th node, and G is a Green's function that

represents the heat transfer from point sources at $(x_i', y_i', 0)$ and $(-x_i', y_i', 0)$ to a semi-infinite medium [22]: two point sources are embedded due to the adiabatic condition at $x = 0$. The total thermometer sample size is 1 cm × 1 cm × 500 μm, big enough for a semi-infinite approximation. The calculated temperature rise at $z = 500$ μm is only around 0.02 K in the maximum heat transfer case, validating the semi-infinite assumption. The presence of 1 μm SiO_2 film was considered in the calculation, assuming that the film is thin enough to allow the 1-D approximation: only the area under the cantilever has the temperature increase due to the film, yielding

$$T_S(x, y) = T_b(x, y, 0) + q_g'' \frac{d_f}{k_f} \tag{5.4}$$

where d_f is the film thickness and k_f is the thermal conductivity of the film. From the temperature distribution of the substrate, the mean temperature that the thermometer measures can be calculated with the following equation:

$$T_{TH} = \frac{1}{L} \int_L T_S(x, y) dl \tag{5.5}$$

where L is the length of the thermometer and dl is either dx or dy depending on the thermometer direction. Even though Eq. (5.4) ignores the in-plane heat spread along the film and thus overestimates of the substrate temperature under the cantilever and underestimates the temperature elsewhere, the integration in Eq. (5.5) will compensate these discrepancies to allow the reasonable prediction of the thermometer mean temperature.

5.4 Results and Discussion

The heated cantilever was first electrically and thermally characterized when the cantilever is off the substrate and on the substrate. It should be noted that the cantilever was not controlled for the characterization: the potentiometer was set to zero, and ΔV_C was measured to obtain the voltage drop across the cantilever. Figure 5.4(a) shows the cantilever resistance as a function of the cantilever heater temperature measured with a Raman spectroscope. TCR of the cantilever is nonlinear and even becomes negative at $T_H = 900$ K. This negative TCR occurs because, with increasing temperature, thermally generated intrinsic carriers eventually outnumber the fixed number of doping carriers [18]. In Fig. 5.4(b), the cantilever resistance is plotted against the cantilever power dissipation. Compared to when the cantilever is off the substrate, the on-substrate case shifts the resistance curves to the larger power dissipation up to 10 mW, indicating that heat transfer to the substrate becomes an important heat transfer mechanism.

Solid curves in Fig. 5.4(b) represent the calculation results. The calculation was performed based on the measured cantilever resistance-temperature relation in Fig. 5.4(a), under the assumption that 90% of the cantilever power is dissipated in the heater region. For the off-substrate calculation, the cantilever thickness was used as a fitting parameter. As shown in Fig. 5.4(b), the agreement between the calculation and the measurement for the off-substrate case is excellent within 0.5 % relative standard error. The estimated cantilever thickness is 745 nm, which is a little smaller than the designed thickness. However, the estimated thickness is a reasonable value when considering a rather large uncertainty in the etching procedure [1]. When the cantilever is on the substrate, Eqs. (5.1) to (5.4), which are coupled together, should be simultaneously

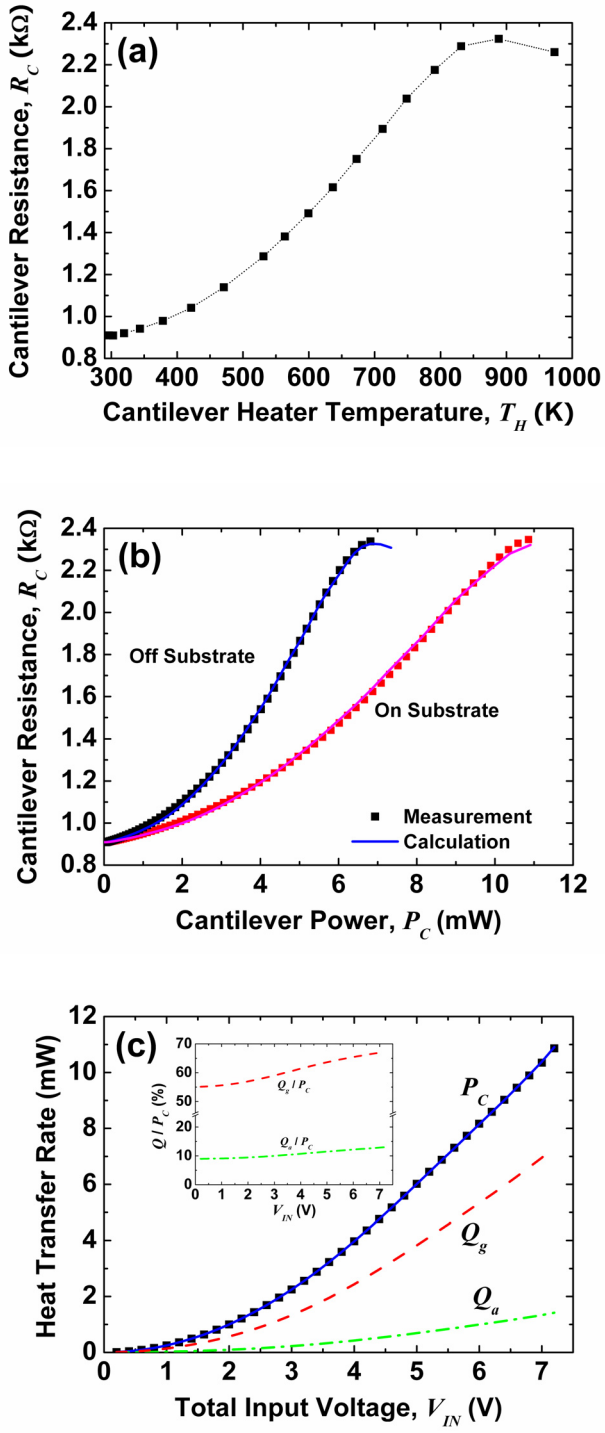

Figure 5.4 The characteristics of the heated cantilever when it is off the substrate and on the subsrate. (a) The cantilever resistance is related with the cantilever heater temperature, which was measured with a micro-Raman spectroscope. (b) The cantilever DC characteristic curves are compared for the off-substrate and on-substrate cases. When the cantilever is engaged on the substrate, more heat is transferred from the cantilever to the susbstrate, moving the characteristic curve to the larger cantilever power. (c) The calculation reveals that up to 70 % of the cantilever power is transferred to the substrate, making a dominant heat transfer mechanism.

calculated to take into account the thermal interaction between the cantilever and substrate. Temperature distribution along the cantilever and that of the substrate right below the cantilever were iteratively calculated until heat flow to the substrate converges within 0.1 %. By using the cantilever-substrate gap as a fitting parameter, the calculation of the cantilever resistance was compared with the measurements in Fig. 5.4(b), which shows a good agreement within 1.0 % relative standard error. The estimated cantilever-substrate gap is 1.4 μm. It should be noted that this gap does not represent a true cantilever-substrate gap, or the true cantilever tip height, as in the calculation the cantilever was assumed to be in parallel with the substrate. In fact, the cantilever is tilted by 11° to the substrate, substantially changing the cantilever-substrate gap: for example, opposite edges of the cantilever heater, i.e., 8 μm in width, makes 1.5 μm height difference, which is already comparable to the estimated effective gap.

Figure 5.4(c) shows measured and calculated cantilever power dissipation as a function of the total input voltage, together with the calculated heat transfer rate to the air as well as to the substrate. The calculation and measurement are in nearly perfect agreement. As clearly shown in the inset, the heat transfer to the substrate Q_g is a dominant heat transfer mechanism, being responsible for up to 70 % of the cantilever power dissipation. The heat transfer to the air Q_a takes around 10 to 15 %, depending on the input voltage. The heat transfer rate along the cantilever leg occupies around 35 % of the power dissipation when the input voltage is small, but decreases down to 15 % at the maximum input voltage. This decrease of the leg conduction may be attributed to the decreasing thermal conductivity with temperature.

Before characterizing the thermometer, operation condition and electrical transport properties of the thermometer were first examined. During the experiment, the driving current I_{IN} was set to 0.2 mA, providing the base thermometer resistance of 3.58 kΩ. The power dissipation was 70.3 μW, from which the temperature rise is estimated less than 0.03 K. The resistivity of the thermometer can be estimated from the measured resistance and the sensing probe geometry, 35 nm × 140 nm in cross sectional area and 29 μm in length. The estimated resistivity is 5.63×10^{-5} Ω-cm, around five times larger than the bulk resistivity of platinum, 1.06×10^{-5} Ω-cm. Previous study on platinum nanowires [23] revealed that the resistivity of an electrodeposited 70-nm-diameter Pt nanowire is three times of the bulk resistivity, indicating that the estimated thermometer resistivity is reasonable. We believe that besides the size effect, rough boundaries formed during the FIB-milling process also contribute to the increase of boundary scattering, giving rise to the large thermometer resistivity: see Fig. 5.1(c).

The thermometer was characterized by placing the heated cantilever on the thermometer with two different directions. Figure 5.5(a) shows the increasing thermometer resistances as the cantilever power increases. As expected, the thermometer resistance increases more steeply when the cantilever is aligned in parallel with the thermometer sensing probe than when the cantilever is aligned perpendicular; That is, more area of the thermometer is covered by the cantilever in the former case. In order to estimate TCR of the thermometer, Fig. 5.5(b) compares the measured thermometer resistance with the calculated thermometer temperature with Eq. (5.5). TCR is estimated as 0.0011 K^{-1} for the parallel alignment and 0.0012 K^{-1} for the perpendicular alignment, less than a third of the TCR of bulk platinum, 0.0039 K^{-1}. The size-dependent

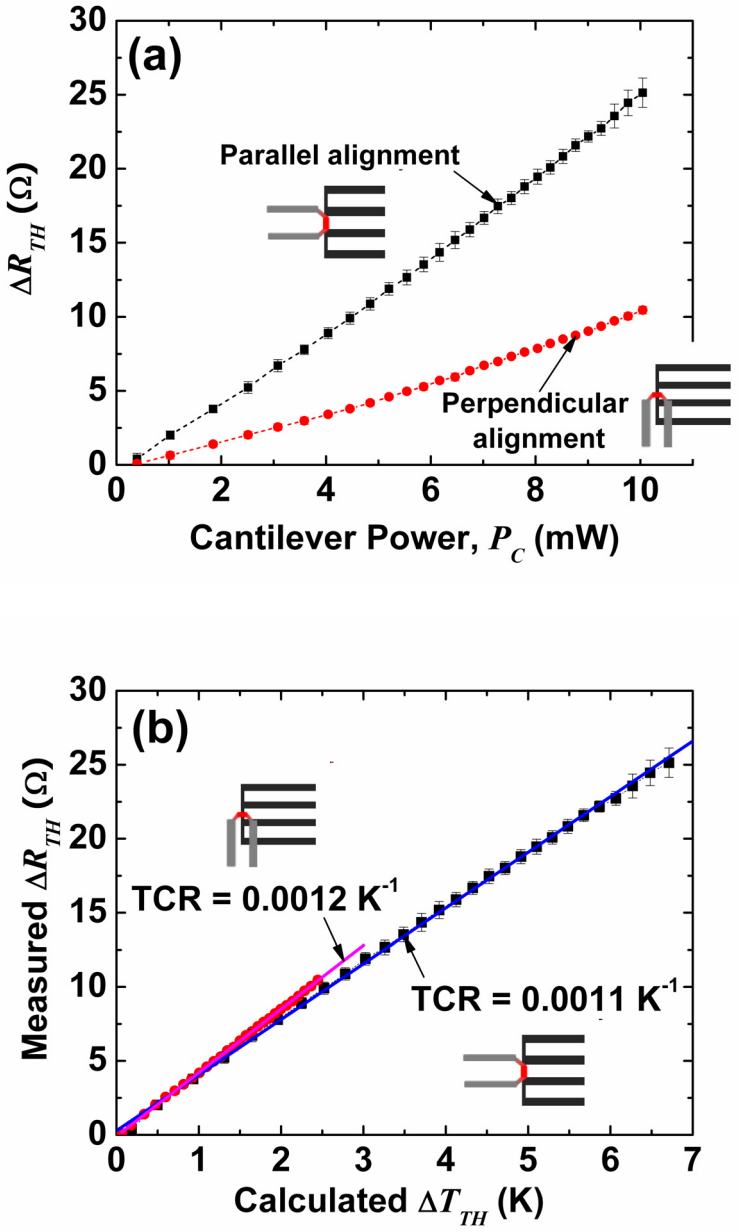

Figure 5.5 The characteristics of the thermometer. (a) The thermometer resistance change is linearly proportional to the cantilever power. The slope difference between parallel and perpendicular alignments is attributed to the effective heat transfer area. (b) By comparison of the measurement and the calculation, TCR of the thermometer is estimated to be between 0.0011 K^{-1} and 0.0012 K^{-1}.

TCR of platinum has been reported by several research groups. Marzi et al. [23] estimated 0.0014 K^{-1} as the TCR of an electrodeposited platinum nanowire of 70 nm diameter, and Zhang et al. [24] measured the TCR of a polycrystalline platinum nanofilm of 62 nm thickness to be 0.0013 K^{-1}. When comparing with these values and considering rather large uncertainties related with the nanoscale measurement, obtained thermometer TCR values can be taken as a reasonable value. In fact, the TCR of a nanofabricated platinum structure may depend on the characteristic length as well as on the fabrication method. The difference of the thermometer TCR for the two alignments may be attributed to the misalignment of the cantilever. Particularly in the perpendicular case, oblique alignment of the cantilever will cover a relatively larger area of the sensing probe and thus yield a bigger TCR than what would be obtained under the perfect alignment.

The determined thermometer TCR allows the measurement of the temperature distribution of the substrate while the heated cantilever raster scans over the thermometer. Figure 5.6(a) is the topographic image formed around the thermometer sensing probe, which was obtained in tapping mode. The thermometer is associated with the sharp peak in the middle. Around the peak has a trench of 60 nm in depth, indicating that the FIB overetched the sample. In fact, the overetching is unavoidable to guarantee the complete removal of the platinum residue and its adverse effect on the thermometer measurement. The platinum strip to the left was for another purpose and not used in the current experiment. Figure 5.6(b) shows the cantilever voltage change during the scanning while the cantilever resistance is maintained at 1.75 kΩ. The cantilever voltage image is inverse to the topographic image, because more power is needed as the cantilever moves closer to the substrate. The estimated sensitivity of the voltage signal change is approximately 130

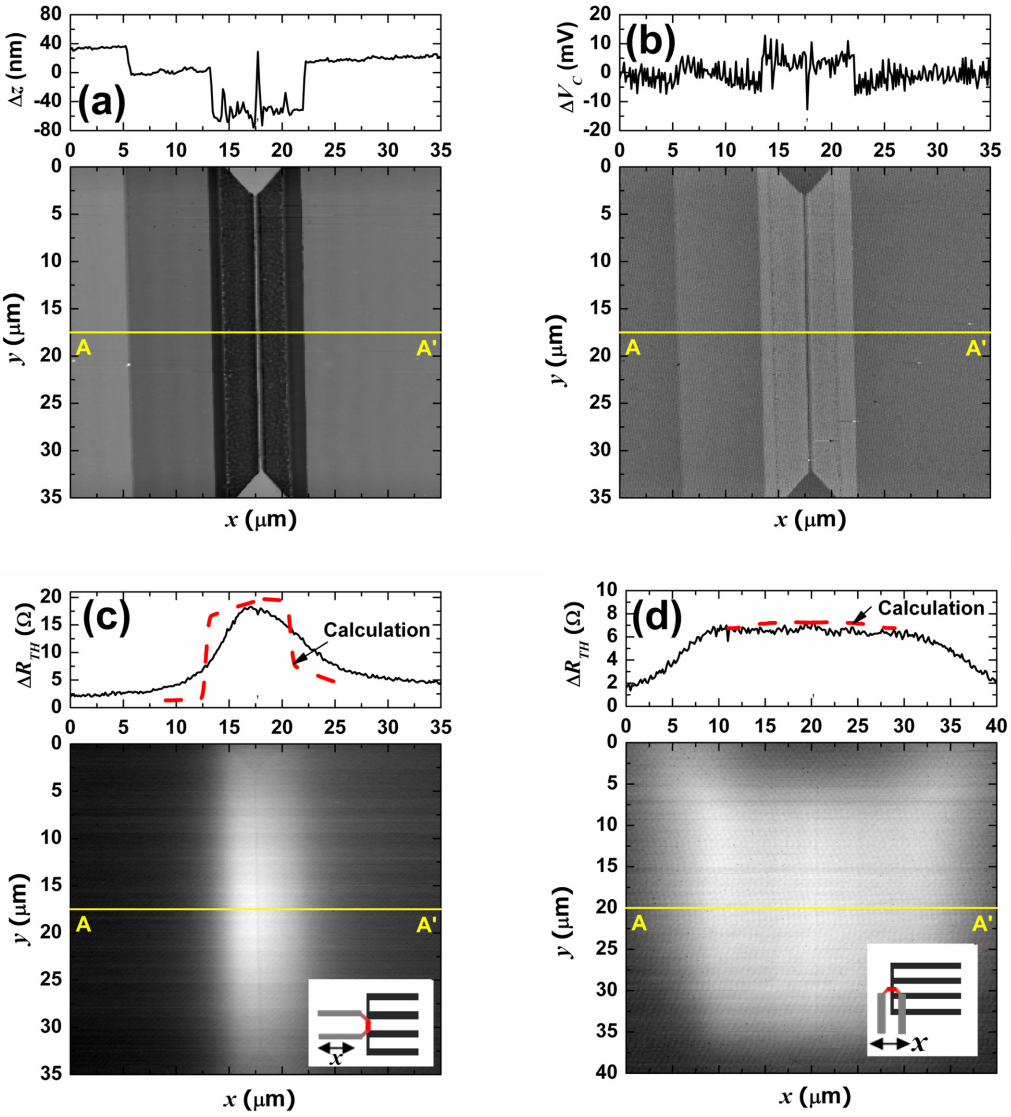

Figure 5.6 AFM images when the cantilever controlled with 1.75 kΩ resistance scans over the thermometer in parallel and perpendicular directions: (a) The topography image of the thermometer sensing probe, (b) cantilever voltage image, (c) thermometer resistance image in parallel scanning, and (d) thermometer resistance image in perpendicular scanning. The calculation results of the thermometer resistance are shown together in (c) and (d).

μV/nm, which is similar to the results in Chapter 4. However, when compared to Chapter 4 that did not use the feedback control, Fig. 5.6(b) has significant noises. The reason may be found from the data sampling rate and its relation with the thermal time constant. Due to the limited computation speed of the real-time control using Labview, the sampling rate was set to 2 kilosamples per second, leaving 500 μs interval between adjacent data points. This interval is comparable to the thermal time constant of the cantilever and thus cannot perfectly control the cantilever resistance; In future, a more sophisticated and faster control can be anticipated for better results.

Thermometer signals are imaged in Figs. 5.6(c) and (d), which respectively represent the parallel scanning and perpendicular scanning cases. The scanning speed was set to 0.5 Hz for 35 μm scanning with 256 point-measurement, taking around 3 ms for the cantilever to move to the adjacent point being 137 nm apart. If the substrate is assumed as a semi-infinite system with a point heat source, the approximated thermal time constant of the substrate over the scanned range is around 10 μs, indicating that the scanning speed is slow enough to satisfy the steady state condition. When the cantilever approaches the thermometer in parallel as in Fig. 5.6(c), the thermometer signal gradually increases, having a maximum value when the middle of the cantilever heater passes through the sensing probe. The maximum resistance increase is around 18 Ω, or 4.7 K temperature increase. Although the cantilever heater maintains its temperature of around 670 K and provides 4.8 mW to the substrate, a small substrate temperature increase is observed because the heat spreads out through the silicon substrate due to its large thermal conductivity. After the cantilever passes the thermometer, the thermometer signal gradually decreases and maintains a small resistance. Heat transfer from the cantilever

leg affects the substrate temperature, resulting in the asymmetric shape of the thermometer resistance curve. For comparison, the calculated thermometer resistance is shown together in Fig. 5.6(c). As expected, the calculation has a very steep change in temperature distribution, as the current model used 1-D approximation for the film. Nevertheless, the calculation predicts the maximum thermometer resistance quite well. Moreover, the calculation also shows the asymmetric shape due to the heat transfer from the leg region. Figure 5.6(d) shows the thermometer resistance image when the cantilever is in perpendicular alignment with the sensing probe. It should be noted that the scanned range was increased to 40 μm to observe the tails of the resistance curve. Compared to Fig. 5.6(c), the thermometer resistance profile becomes more flat because the thermometer is exposed to the cantilever heater longer than the parallel case. However, the thermometer area covered by the cantilever heater is only around half of the parallel scanning experiment, resulting in smaller resistance increase; around half of the resistance increase in Fig. 5.6(c). The calculation result is nearly the same as the measurements, confirming the flat profile along the cantilever heater length.

Figure 5.7 shows single-line scanned cantilever and thermometer voltage profiles while changing the controlled cantilever resistances from 1.0 kΩ to 2.0 kΩ. The measurement was performed 128 times on the same scan line, and only the averaged curves are plotted. Figure 5.7(a) shows the cantilever voltage curves. It should be noted that DC-offsets were ignored in the figure to plot different cases together. As the cantilever is operated with higher resistances, the cantilever voltage change becomes more prominent because the TCR of the cantilever is larger at the higher cantilever resistance. The sensitivity of the cantilever voltage change at $R_C = 2.0$ kΩ is around 200

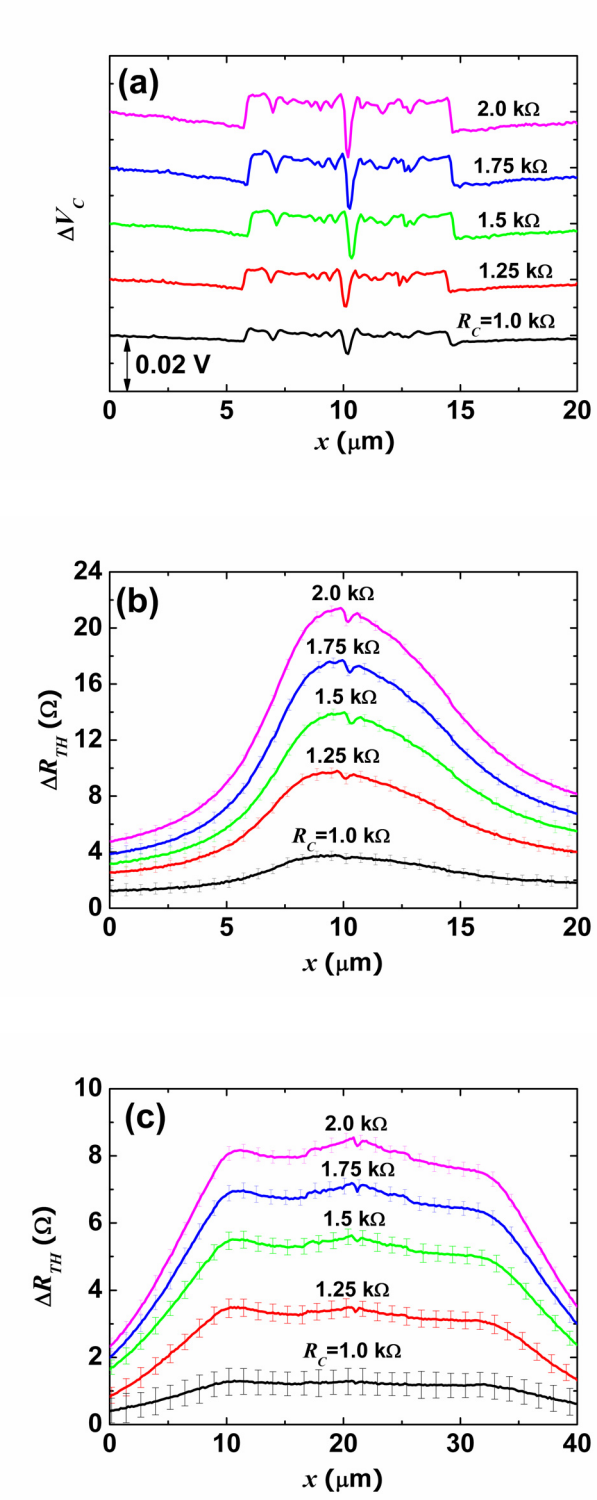

Figure 5.7 Single-line scanned cantilever and thermometer signal profiles when the cantilever resistance is controlled with different values. As the cantilever resistance increases, more heat is transferred from the cantilever and substrate, resulting in (a) increase of ΔV_C, (b) increase of ΔR_{TH} for parallel scanning, and (c) increase of ΔR_{TH} for perpendicular scanning.

μV/nm. Figure 5.7(b) has the thermometer resistance curves for the parallel scanning. The uncertainty is estimated to be around $\pm 0.4\ \Omega$ regardless of the cantilever resistances, which is largely due to the fluctuations of the cantilever voltage shown in Fig. 5.6(b). The small dips near the resistance maxima are attributed to the increasing cantilever-substrate gap when the cantilever tip passes through the thermometer sensing probe that is higher than the trench ground by around 95 nm. A dip depth for $R_C = 2.0\ \text{k}\Omega$ is around 1.0 Ω, corresponding to 0.25 K temperature decrease. The magnitude of this temperature decrease suggests that even though the nanoscale heat transfer near the tip may be important for local heating of the substrate [5], the air gap is a dominant factor in the cantilever-to-substrate heat transfer. The uneven topography of our thermometer prevents the measurement of the possible temperature rise due to the heat transfer near the tip. This localized temperature rise could be measured only with a thermometer that has a spatial resolution comparable to the tip radius, a milli-Kelvin temperature resolution, and a flat profile to decouple the gap-changing effect from the measurement. The dip position is a little off the summit, indicating that the tip is not located at the center of the heater.

The perpendicular scanning results are shown in Fig. 5.7(c), with the uncertainty of around ± 0.2 Ω. As already observed in Fig. 5.6(d), there exists a flat region corresponding to the heater length. The resistance curves experience a small jump around the middle, which is associated with the presence of the trench. The thermometer senses the increased heat transfer when the cantilever tip falls into the trench. Another interesting feature is that the curves are asymmetric: there is a small side peak at the left. Since the side peak position coincides with the thermal constriction region, the side peak may result from the asymmetric fabrication of the constriction regions. Another

possibility is that a hot spot may exist only at one boundary of the heater. Recent study on an IBM Millipede heated cantilever revealed that a hot spot switches its position from one boundary of the heater to the other when the electrical current direction is reversed, which may be due to the Peltier thermoelectric effect [25]. More study should be followed to clarify the origin of the asymmetry in the thermometer resistance.

To observe the heat transfer rate varying with a different cantilever-substrate gap, the cantilever deflection, cantilever voltage, and thermometer resistance were simultaneously recorded while the heated cantilever approached and then retracted from the thermometer probe aligned in parallel with the cantilever. Figure 5.8(a) shows the cantilever deflection for different cantilever resistances. As in Fig. 5.7(a), the original data were modified to plot all the cases in one figure: only the relative change will be meaningful. When the cantilever approaches the substrate with $R_C = 1.0$ kΩ, the cantilever deflection signal remains nearly unchanged until the cantilever contacts the thermometer. The cantilever then "jumps" to contact with the thermometer due to the attractive force between the tip and thermometer. This attractive force is also responsible for the "snapping" out of contact when the cantilever retracts from the thermometer. Since the cantilever tip temperature is close to room temperature when $R_C = 1.0$ kΩ, the attractive force in this case most likely originates from the capillary effect of the water film formed between the cantilever tip and thermometer [12,13]. When the higher cantilever resistance is large (e.g., $R_C = 2.0$ kΩ), the cantilever deflection changes during the approach and retract, suggesting that another type of attractive force is involved. In fact, high cantilever heater temperature at $R_C = 2.0$ kΩ evaporates the water film, removing the capillary effect. We believe that the attractive force at high cantilever

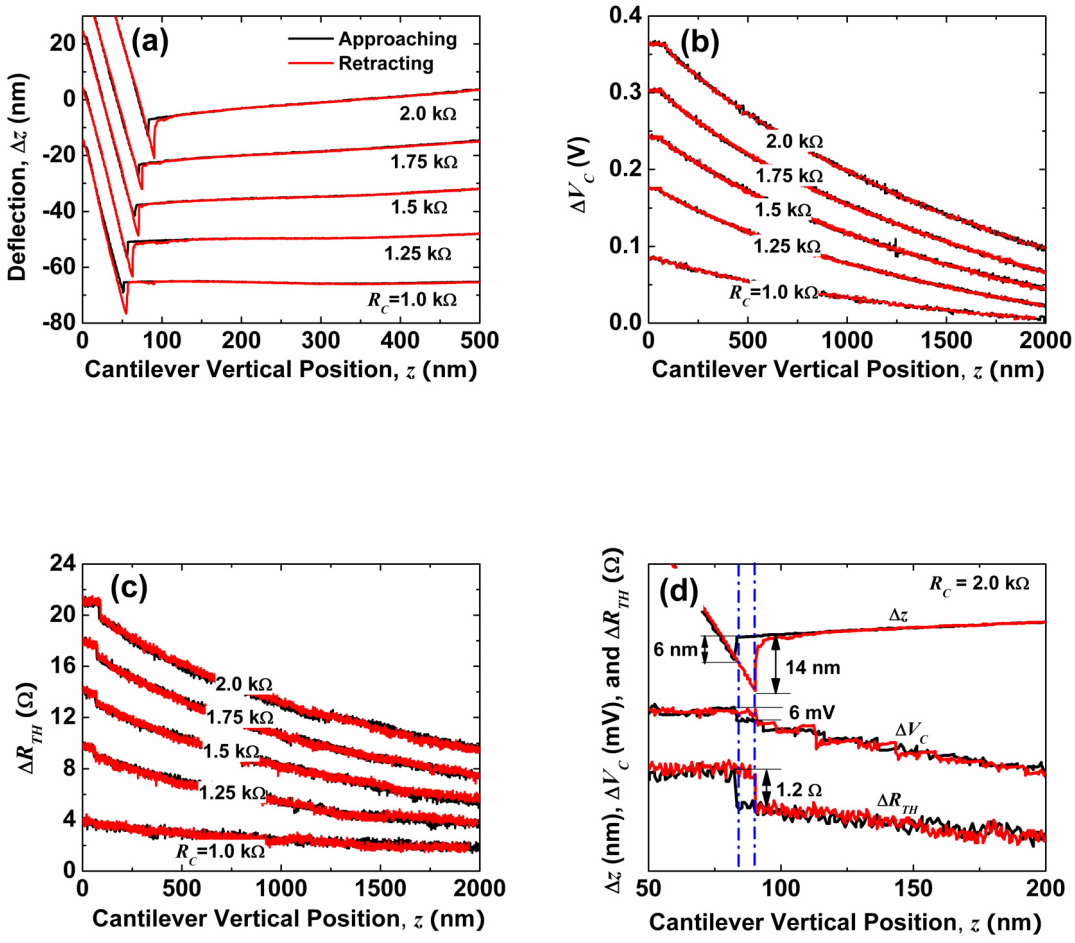

Figure 5.8 The force-displacement experiment results when the cantilever is aligned with the nanothermometer in parallel and controlled with the cantilever resistance. (a) The deflection signal shows that as the cantilever resistance is higher, the cantilever is bended down due to electrostatic and thermal forces. (b) The cantilever voltage increases as the cantilever approaches the substrate to maintain the temperature. (c) As a result, the thermometer resistance increases as the cantilever approaches the substrate. (d) Interestingly, there is jump on the cantilever and thermometer signals when the cantilever contacts the substrate, from which the effective contact conductance can be estimated to be around 40 nW/K.

resistances is the combination of the electrostatic force and thermal force [26].

Figures 5.8(b) and (c) respectively show the cantilever voltage and thermometer resistance changes. When the cantilever approaches, both the cantilever and thermometer signals increase because more heat is transferred to the substrate due to decreasing cantilever-substrate gap. After contact, however, the air gap does not change any more, and both signals remain constant. Interesting results can be observed at the moment of contact and out of contact, which can be more clearly observed in Fig. 5.8(d). At the very moment when the cantilever of $R_C = 2.0$ kΩ contacts the thermometer, the thermometer signal jumps up by around 1.2 Ω, which corresponds to 0.3 K temperature increase. The cantilever voltage change is around 6 mV while the vertical displacement changes around 6 nm. When considering the measured sensitivity of the cantilever voltage signal, i.e., 200 μV/nm at $R_C = 2.0$ kΩ, the cantilever snap-in and resultant change of its vertical displacement would correspond to only a 1.2 mV jump in the cantilever voltage. Thus, these stepwise changes of cantilever and thermometer signals may be mainly attributed to the cantilever contact with the thermometer. The effective contact conductance can be estimated, yielding around $\bar{\sigma}_C = 40$ nW/K. The estimated contact conductance is close to what was suggested by previous work [9,13,27]: they estimated the solid-solid contact conductance to be between 10 and 100 nW/K. The estimated contact thermal conductance may include other thermal resistances such as tip resistance and spread resistance in the substrate [27]. It should be noted that the estimated gap conductance from the cantilever heater is around 13.3 μW/K at $R_C = 2.0$ kΩ, which is still two orders of magnitude larger than the contact conductance.

5.5 Conclusion

This study elucidates the heat transfer between the heated microcantilever and the substrate by measuring the substrate temperature rise. To this end, a platinum resistive thermometer whose spatial resolution is around 140 nm in lateral direction has been fabricated on the 1 μm SiO_2-coated silicon substrate. TCR of the thermometer is estimated to be 0.0011 K^{-1}, approximately one third of the bulk value. In an AFM platform, the heated cantilever scanned over the thermometer with various cantilever resistances in control, simultaneously providing the topography of the thermometer, cantilever voltage change, and the thermometer resistance change. When the cantilever scans in parallel direction with the thermometer sensing probe, up to 70 % of the cantilever power is transferred to the substrate to increase the substrate temperature by around 7 K. From the force-displacement experiment, the effective contact conductance was estimated to be around 40 nW/K, which is much smaller than the air gap conductance, indicating that the air conduction through the gap is a dominant heat transfer mechanism. The obtained results will facilitate further understanding on the thermal behavior of the heated cantilever during the scanning and its thermal effect on the substrate.

5.6 References

[1] J. Lee, T. Beechem, T. L. Wright, B. A. Nelson, S. Graham, and W. P. King, "Electrical, thermal, and mechanical characterization of silicon microcantilever-heaters," *Journal of Microelectromechanical Systems*, vol. 15, pp. 1644-1655, 2006.

[2] This work, *Chapter 2*.

[3] J. Lee, T. L. Wright, M. R. Abel, E. O. Sunden, A. Marchenkov, S. Graham, and W. P. King, "Thermal conduction from microcantilever heaters in partial vacuum," *Journal of Applied Physics*, vol. 101, 014906, 2007.

[4] This work, *Chapter 3*.

[5] W. P. King, T. W. Kenny, K. E. Goodson, G. L. W. Cross, M. Despont, U. T. Dürig, H. Rothuizen, G. Binnig, and P. Vettiger, "Design of atomic force microscope cantilevers for combined thermomechanical writing and thermal reading in array operation," *Journal of Microelectromechanical Systems*, vol. 11, pp. 765-774, 2002.

[6] W. P. King, T. W. Kenny, and K. E. Goodson, "Comparison of thermal and piezoresistive sensing approaches for atomic force microscopy topography measurements," *Applied Physics Letters*, vol. 85, pp. 2086-2088, 2004.

[7] W. P. King, "Design analysis of heated atomic force microscope cantilevers for nanotopography measurements," *Journal of Micromechanics and Microengineering*, vol. 15, pp. 2441-2448, 2005.

[8] A. Majumdar, "Scanning thermal microscopy," *Annual Review of Materials Science*, vol. 29, pp. 505-585, 1999.

[9] K. Luo, Z. Shi, J. Varesi, and A. Majumdar, "Sensor nanofabrication, performance, and conduction mechanisms in scanning thermal microscopy," *Journal of Vacuum Science & Technology B*, vol. 15, pp. 349-360, 1997.

[10] L. Shi, O. Kwon, A. C. Miner, and A. Majumdar, "Design and batch fabrication of probes for sub-100 nm scanning thermal microscopy," *Journal of Microelectromechanical Systems*, vol. 10, pp. 370-378, 2001.

[11] D. W. Lee, T. Ono, and M. Esashi, "Fabrication of thermal microprobes with a sub-100 nm metal-to-metal junction," *Nanotechnology*, vol. 13, pp. 29-32, 2002.

[12] S. Gomes, N. Trannoy, and P. Grossel, "DC thermal microscopy: study of the thermal exchange between a probe and a sample," *Measurement Science & Technology*, vol. 10, pp. 805-811, 1999.

[13] L. Shi and A. Majumdar, "Thermal transport mechanisms at nanoscale point contacts," *Journal of Heat Transfer*, vol. 124, pp. 329-337, 2002.

[14] S. Lefevre, S. Volz, and P. O. Chapuis, "Nanoscale heat transfer at contact between a hot tip and a substrate," *International Journal of Heat and Mass Transfer*, vol. 49, pp. 251-258, 2006.

[15] D. Chu, D. T. Bilir, R. F. W. Pease, and K. E. Goodson, "Submicron thermocouple measurements of electron-beam resist heating," *Journal of Vacuum Science & Technology B*, vol. 20, pp. 3044-3046, 2002.

[16] D. Chu, W.-K. Wong, K. E. Goodson, and R. F. W. Pease, "Transient temperature measurements of resist heating using nanothermocouples," *Journal of Vacuum Science & Technology B*, vol. 21, pp. 2985-2989, 2003.

[17] This work, *Chapter 4*.

[18] B. W. Chui, M. Asheghi, Y. S. Ju, K. E. Goodson, T. W. Kenny, and H. J. Mamin, "Intrinsic-carrier thermal runaway in silicon microcantilevers," *Microscale Thermophysical Engineering*, vol. 3, pp. 217-228, 1999.

[19] U. Dürig, "Fundamentals of micromechanical thermoelectric sensors," *Journal of Applied Physics*, vol. 98, 044906, 2005.

[20] N. Masters, W. Ye, and W. P. King, "The impact of sub-continuum gas conduction on the sensitivity of heated atomic force microscope cantilevers," *Physics of Fluids*, vol. 17, 100615, 2005.

[21] C. J. Fu and Z. M. Zhang, "Nanoscale radiation heat transfer for silicon at different doping levels," *International Journal of Heat and Mass Transfer*, vol. 49, pp. 1703-1718, 2006.

[22] J. V. Beck, *Heat Conduction Using Green's Functions*, New York: Hemisphere Pub. Corp., 1992.

[23] G. D. Marzi, D. Iacopino, A. J. Quinn, and G. Redmond, "Probing intrinsic transport properties of single metal nanowires: direct-write contact formation using a focused ion beam," *Journal of Applied Physics*, vol. 96, pp. 3458-3462, 2004.

[24] Q. G. Zhang, B. Y. Cao, X. Zhang, M. Fujii, and K. Takahashi, "Size effects on the thermal conductivity of polycrystalline platinum nanofilms," *Journal of Physics-Condensed Matter*, vol. 18, pp. 7937-7950, 2006.

[25] H. F. Hamann, *private communication*, unpublished (2006).

[26] B. Gotsmann and U. Dürig, "Experimental observation of attractive and repulsive thermal forces on microcantilevers," *Applied Physics Letters*, vol. 87, 194102, 2005.

[27] B. A. Nelson and W. P. King, "Measuring material softening with nanoscale spatial resoultion using heated silicon probes," *Review of Scientific Instruments*, vol. 78, 023702, 2007.

CHAPTER 6

STUDY OF THE SURFACE AND BULK POLARITONS WITH A NEGATIVE INDEX METAMATERIAL

Previous chapters so far have focused on the applications of a heated microcantilever, particularly its feasibility as a thermal metrology tool, which mainly utilizes thermal conduction at the micro/nanometer scale. From this chapter, a focus moves to thermal radiation at the extremely small length-scale, so-called near-field thermal radiation, and its promising application to sustainable energy conversion. To better understand the near-field effect on the thermal radiation, this chapter focuses on surface and bulk polaritons in a multilayer structure and their impact towards the radiative properties, especially the reflectance. Particularly, a three-layer structure where a negative index metamaterial (NIM) sandwiched between different dielectric layers is investigated. A Regime map is developed to describe the polariton dispersion relations and to help understand the effect of the NIM layer thickness on the polariton resonance frequencies. For an NIM layer, the dispersion curves of a surface polariton and a bulk polariton are smoothly connected, suggesting that a surface mode can be converted into a bulk mode, and *vice versa*. In an attenuated total reflection (ATR) configuration, the gap between the prism and the NIM layer has a strong influence on the location and magnitude of the reflectance minimum. Furthermore, surface polaritons may exist at a single boundary and enhance the energy transmission via photon tunneling. These results demonstrate that surface and bulk polaritons significantly affect the radiative properties

in a layered structure, and an NIM is a good candidate to effectively "tune" the thermal radiation between objects.

6.1 Introduction

A polariton is an elementary excitation that occurs when a plasmon or a phonon is resonantly coupled with the incident electromagnetic (EM) wave [1]. A surface polariton (also known as a surface wave) is associated with the EM waves that propagate along the interface and decay exponentially into both media. The excitation of surface polaritons causes a resonance transfer of the photon energy to a surface wave and is manifested in an attenuated total reflectance (ATR) configuration as a sharp drop in the reflectance. This strong coupling of energy is a unique characteristic of polaritons and has been intensively studied for various applications, such as high-speed electro-optic modulators [2], terahertz quantum-cascade lasers [3], and near-field microscopes [4,5]. Besides the optical applications, surface polaritons also play an important role in radiative heat transfer [6]. In fact, many applications using surface polaritons have been proposed: for example, wavelength-selective thermal emitter [7], spectrally and directionally coherent thermal emission source [8,9], and near-field thermophotovoltaics [10,11]. A surface polariton can occur only when either the electric permittivities (for *p*-polarization or TM wave) or the magnetic permeabilities (for *s*-polarization or TE wave) of the two adjacent media have opposite signs.

Recent advances in materials research have made it possible to synthesize a metamaterial that exhibits simultaneously negative permittivity and permeability in the microwave region [12, 13], resulting in a negative index of refraction. The so-called

negative index material (NIM), or the left-handed material, has generated tremendous interest because NIMs introduced some counterintuitive phenomena such as negative refraction, focusing light by a flat slab, and the amplification of evanescent waves [14-21]. Pendry [19] showed that an evanescent wave could be amplified by an NIM layer and went further to hypothesize that an NIM slab could make a perfect lens, whose resolution is not diffraction limited. Zhang and Fu [20,21] predicted that the growing evanescent wave in the presence of an NIM layer could enhance the photon tunneling and energy transmission through a multilayer structure. In essence, the amplification of evanescent waves in the above-mentioned applications is attributed to the excitation of surface polaritons.

Ruppin [22] first noted that surface polaritons could be excited not only for *p*-polarization but also for *s*-polarization at the interface between an NIM and a dielectric, by utilizing its property of negative permittivity and negative permeability. Generally speaking, there are three polariton dispersion curves: two for *p*-polarization and one for *s*-polarization. Darmanyan et al. [23] provided a detailed investigation on the frequency domain of existence for surface polaritons between an NIM and a conventional material. As pointed out by Ruppin in another publication [24], when the thickness of the NIM medium is finite, the polariton dispersion curves split into four branches for *p*-polarization and two branches for *s*-polarization. However, his study dealt only with the symmetric case, in which both sides of the NIM layer are made of the same material, and paid little attention to bulk polaritons, which are standing EM waves inside a thin slab and decay exponentially outside the slab [25].

A thorough understanding of the polariton phenomena in an NIM layer is required to facilitate its applications in imaging optics and energy conversion. In the present work, both surface and bulk polaritons are investigated for an NIM layer sandwiched between dissimilar dielectrics for *p*- and *s*-polarizations. The optical properties are calculated in an ATR setup, as illustrated in Fig. 6.1, where radiation is incident from a prism through a vacuum gap onto a planer NIM layer, located above a semi-infinite dielectric medium. The effects of NIM layer thickness and the vacuum gap width on the behavior of polaritons are examined. The result is presented in generalized dimensionless forms, making it useful not only in the microwave region but also in other frequency regions if suitable NIMs can be realized someday.

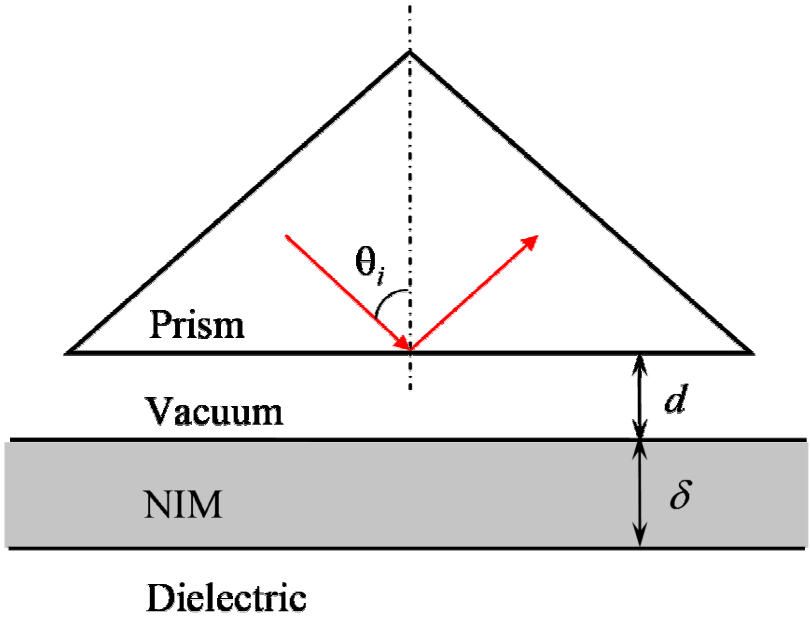

Figure 6.1 The geometry of attenuated total reflection (ATR) configuration used for the calculation of optical properties with an NIM layer.

6.2 Polariton Dispersion Relation

The polariton dispersion relations (or criteria) for a slab of thickness d between two semi-infinite media, as shown in Fig. 6.2, can be derived following the same procedure as in the work of Ruppin [24]. It is assumed here that each medium is isotropic and can be characterized by a relative permittivity ε and a relative permeability μ, which generally depend on the frequency. For *s*-polarization, the time harmonic electric field can be expressed as follows:

$$\mathbf{E} = \hat{\mathbf{y}} \begin{cases} Ae^{\beta_1 z}\ e^{jk_x x}, & z < 0 \\ \left(Be^{-\beta_2 z} + Ce^{\beta_2 z}\right)\ e^{jk_x x}, & 0 < z < \delta \\ De^{-\beta_3 (z-\delta)}\ e^{jk_x x}, & z > \delta \end{cases} \tag{6.1}$$

where $j = \sqrt{-1}$, $\hat{\mathbf{y}}$ is the unit vector in the *y*-direction; coefficients A, B, C, and D are determined by the boundary conditions; k_x is the tangential wavevector component, which is identical in all media to satisfy the phase-matching requirement; and

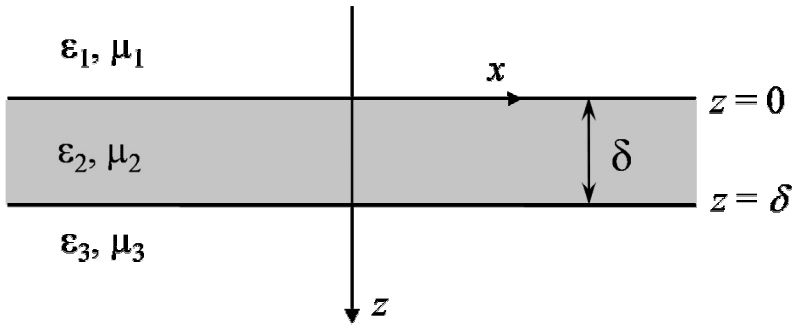

Figure 6.2 Illustration of a slab between two semi-infinite media for the study of the polariton dispersion relations.

β_i $(i = 1, 2, 3)$ is related to the normal wavevector component $k_{z,i}$ by $\beta_i = -jk_{z,i}$. An evanescent wave in the *i*-th medium is characterized by a purely imaginary $k_{z,i}$ or a purely real (positive) β_i. For surface polaritons to occur at both boundaries, evanescent waves must exist in all three media. From $k_i{}^2 = k_x{}^2 + k_{z,i}^2 = \varepsilon_i \mu_i \omega^2 / c^2$, where ω the angular frequency and c the speed of light in vacuum, one obtains

$$\beta_i = \sqrt{k_x{}^2 - \varepsilon_i \mu_i \omega^2 / c^2}, \qquad i = 1, 2, \text{and } 3 \tag{6.2}$$

The tangential components of the magnetic fields can be obtained using Maxwell's equations as

$$H_x = \begin{cases} \dfrac{-j\beta_1}{\omega\mu_0\mu_1} A e^{\beta_1 z} e^{jk_x x}, & z < 0 \\ \dfrac{j\beta_2}{\omega\mu_0\mu_2}\left(B e^{-\beta_2 z} - C e^{\beta_2 z}\right) e^{jk_x x}, & 0 < z < \delta \\ \dfrac{j\beta_3}{\omega\mu_0\mu_3} D e^{-\beta_3 (z-\delta)} e^{jk_x x}, & z > \delta \end{cases} \tag{6.3}$$

where μ_0 is the magnetic permeability of the free space.

The boundary conditions require the tangential components of the electric field and the magnetic field to be continuous at $z = 0$ and $z = \delta$, yielding a system of homogeneous linear equations for coefficients *A*, *B*, *C*, and *D*. The determinant of this system must be zero for nontrivial solutions to exist. After some manipulations, the following equation, which is the surface polariton dispersion relation for *s*-polarization, is obtained.

$$\left(\frac{\beta_2}{\mu_2}\right)^2 + \coth(\beta_2 \delta)\left(\frac{\beta_1}{\mu_1} + \frac{\beta_3}{\mu_3}\right)\frac{\beta_2}{\mu_2} + \frac{\beta_1 \beta_3}{\mu_1 \mu_3} = 0 \tag{6.4}$$

In the symmetric case, $\varepsilon_1 = \varepsilon_3$ and $\mu_1 = \mu_3$, Eq. (6.4) is reduced to the dispersion relations derived by Ruppin [24].

A bulk polariton occurs when both $k_{z,1}$ and $k_{z,3}$ are purely imaginary, but $k_{z,2}$ is real. The bulk polariton relation can be obtained by substituting $-jk_{z,2}$ for β_2 in Eq. (6.4) such that

$$\left(\frac{k_{z,2}}{\mu_2}\right)^2 - \cot(k_{z,2}\delta)\left(\frac{\beta_1}{\mu_1} + \frac{\beta_3}{\mu_3}\right)\frac{k_{z,2}}{\mu_2} - \frac{\beta_1\beta_3}{\mu_1\mu_3} = 0 \tag{6.5}$$

Notice that Eq. (6.5) is the same as the dispersion equation of the waveguide, whose solutions exist only when the sum of all the phase shifts that the guided wave undergoes becomes a multiple of 2π [26]. In the case of a bulk polariton, the electromagnetic fields are oscillatory as a stationary wave inside the slab. The polariton relations for *p*-polarization can be obtained by replacing μ_1, μ_2, and μ_3 in Eqs. (6.4) and (6.5) with ε_1, ε_2, and ε_3, respectively.

In order to illustrate the polariton dispersion relations for an NIM layer, the frequency-dependent complex ε_2 and μ_2 are calculated from the following expressions, as for a wire-strip/split-ring metamaterial [27],

$$\varepsilon_2(\omega) = 1 - \frac{\omega_p^2}{\omega^2 + j\gamma\omega} \tag{6.6}$$

and

$$\mu_2(\omega) = 1 - \frac{F\omega^2}{\omega^2 - \omega_0^2 + j\gamma\omega} \tag{6.7}$$

where ω_p is the plasma frequency, ω_0 is the resonance frequency, γ ($<< \omega_p$ and ω_0) is the electron scattering rate, and F is the fractional area of the unit cell occupied by the split ring. Although NIMs have been demonstrated only in the microwave region,

researchers around the world are attempting to realize NIMs in the infrared and even visible spectral regions. A numerical simulation suggested that novel NIMs in the nearinfrared and visible might be achievable by nanowire composites [28]. Shvets [29] predicted that SiC photonic crystals could exhibit a negative index of refraction in the midinfrared.

Figure 6.3 depicts a regime map in a $k_x - \omega$ space, illustrating the regions where surface or bulk polaritons may exist. Here, media 1 and 3 are assumed to be lossless and nondispersive dielectrics with $\varepsilon_1 < \varepsilon_3$. For the NIM layer, the parameters in Eqs. (6.6) and (6.7) are chosen such that $\omega_0 / \omega_p = 0.4$, $F = 0.56$, and $\gamma = 0$ (lossless) [27]. The effect of γ on the optical properties will be discussed later. The regimes are shown using dimensionless frequency ω / ω_p and wavevector (tangential component) $k_x c / \omega_p$, so that the results are not limited to any specific frequency region. Four dotted lines (i), (ii), (iii), and $\omega = \omega_0$ separate nine different regions. Lines (i), (ii), and (iii) correspond to $\omega = k_x c / \sqrt{\varepsilon\mu}$ for media 1, 2, and 3, respectively. Because the dielectric media are assumed to be nondispersive, (i) and (iii) are straight lines. Notice that the condition for $\omega = k_x c / \sqrt{\varepsilon\mu}$ corresponds to $k_z = 0$ in any given medium. Based on Eq. (6.2), in the regions on the left of line (i), k_x is too small to excite any evanescent waves in media 1 and 3 and thus no polaritons can exist in regions R1, R2, and R3. In the regions between lines (i) and (iii), an evanescent wave appears in medium 1 whilst a propagating wave occurs in medium 3. A surface polariton may exist only at the interface between media 1 and 2. In the regions on the right of line (iii), evanescent waves emerge in both media 1 and 3; hence, surface polaritons may exist on dual boundaries as well as bulk polaritons.

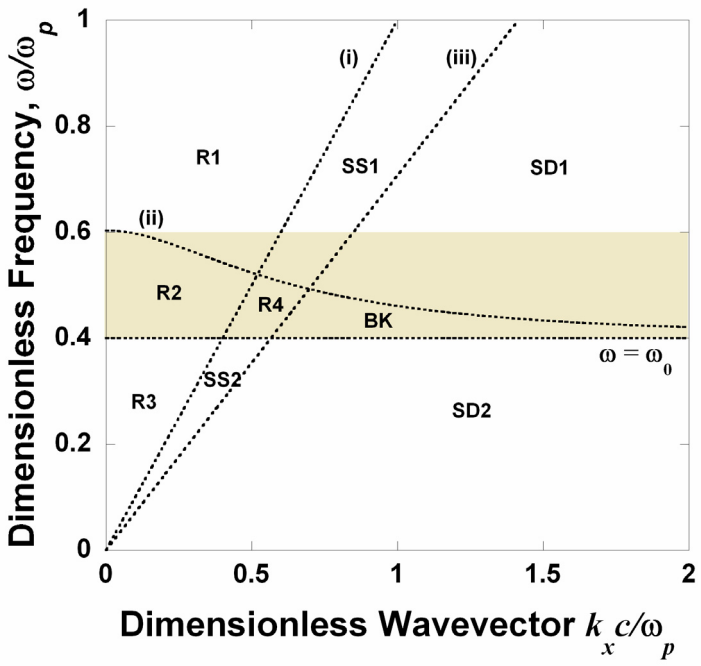

Figure 6.3 The polariton regime map in $k_x - \omega$ space. Here, media 1 and 3 are dielectric with $\varepsilon_1 < \varepsilon_3$, and medium 2 is an NIM with $\omega_0 / \omega_p = 0.4$, $F = 0.56$, and $\gamma = 0$. Lines (i), (ii), and (iii) correspond to $k_z = 0$ in media 1, 2, and 3, respectively. In the shaded area, $0.4\omega_p < \omega < 0.6\omega_p$, the refractive index of medium 2 is negative. No polaritons exist in regions R1 through R4; in regions SS1 and SS2, surface polaritons can occur at a single boundary; in regions SD1 and SD2, surface polaritons may occur at dual boundaries; in BK region, several bulk polaritons may occur.

The shaded area indicates the frequency interval $0.4\omega_p < \omega < 0.6\omega_p$, where both ε_2 and μ_2 are simultaneously negative. Note that the discussion in the present work is limited to frequencies below the plasma frequency, i.e., $\omega < \omega_p$. In the upper regions of line (ii), evanescent waves exist in the NIM layer. In the shaded area, surface polaritons may be observed in region SS1 at a single boundary and in region SD1 at dual boundaries of the NIM slab, for both *p*- and *s*-polarizations. Surface polaritons may also exist in regions SS1 and SD1 above the shaded area for *p*-polarization only (because $\varepsilon_2 < 0$ for $\omega < \omega_p$). On the other hand, in the regions between the line $\omega = \omega_0$ and line (ii), only propagating

waves exist in the NIM layer because $k_{z,2} > 0$. Therefore, no polaritons exist in region R4, whereas bulk polaritons may occur in region BK. Attention is now paid to the regions below the line $\omega = \omega_0$, where $\varepsilon_2 < 0$ and $\mu_2 > 0$. Because $k_{z,2}$ is purely imaginary, surface polaritons may occur at a single boundary in region SS2 and dual boundaries in region SD2, for *p*-polarization only.

It should be noted that regions between lines (i) and (iii) exist only when the two dielectric media are different. In the symmetric case, $\varepsilon_1 = \varepsilon_3$, the two lines will merge into one and the results will be identical to those presented by Ruppin [24]. Since there may exist surface polaritons at a single boundary in regions SS1 and SS2, the polariton dispersion relation in those regions is simplified to that for two semi-infinite media [22, 23], i.e.,

$$\frac{\beta_1}{\mu_1} + \frac{\beta_2}{\mu_2} = 0, \quad \text{for } s\text{-polarization} \tag{6.8}$$

and

$$\frac{\beta_1}{\varepsilon_1} + \frac{\beta_2}{\varepsilon_2} = 0, \quad \text{for } p\text{-polarization} \tag{6.9}$$

The polariton dispersion relations for *s*-polarization are shown in Fig. 4 with different NIM thicknesses: $\delta / \lambda_p = 0.5$ and $\delta / \lambda_p = 0.1$, where $\lambda_p = c / \omega_p$ is the wavelength associated with the plasma frequency. For the dielectric media, it is assumed that $\varepsilon_1 = 1$ (i.e., vacuum) and $\varepsilon_3 = 2$. The dotted lines are the same as the corresponding ones in Fig. 3. Two dash-dotted lines, (I) and (II), are drawn to facilitate the discussion in the next session on the optical properties in an ATR setup shown in Fig. 6.1. Line (I), between lines (i) and (iii), denotes a smaller angle of incidence (θ_i) that can excite evanescent

waves in medium 1 but not in medium 3. Line (II), on the right of line (iii), denotes a larger θ_i that can excite evanescent waves in both media 1 and 3.

The thin solid curves represent surface polariton relations obtained from Eq. (6.4) for finite δ. The two surface polariton curves become more separated as the NIM thickness is reduced. A large separation between the two dispersion curves is an indication of a strong coupling between the associated electromagnetic fields of the two surface polaritons. In the limit when the thickness approaches infinity, $\delta/\lambda_p >> 1$, the polaritons are completely decoupled, resulting in two thick solid curves describing the surface polariton relation between media 1 and 2 and that between media 3 and 2. Note that Eq. (6.4) breaks into two simple surface polariton relations, $\beta_1/\mu_1 + \beta_2/\mu_2 = 0$ and $\beta_2/\mu_2 + \beta_3/\mu_3 = 0$, because $\coth(\beta_2\delta) = 1$ as $\delta \to \infty$. The thick curves are close to each other, indicating that there is no coupling between the two surface polaritons. Only one surface polariton exists in region SS1 at the interface between media 1 and 2. In the symmetric situation when $\varepsilon_1 = \varepsilon_3$, the two thick curves become identical [22,23].

The dashed curves in Fig. 6.4 illustrate the bulk polariton dispersion relations. When compared with bulk polaritons in a slab of conventional material [25,30], bulk polaritons of the NIM layer show a distinct feature. The dispersion curves of a surface polariton and a bulk polariton meet at line (ii), the boundary between regions SD1 and BK (identified in Fig. 6.3). This suggests that the surface polariton of the lower frequency can be converted to the first-order bulk polariton, by reducing the angle of incidence or by decreasing the NIM thickness. The convertibility of polariton modes is a unique feature because only an NIM can possess surface polaritons within the pass band, in which both the permittivity and the permeability are simultaneously negative [22-24,27].

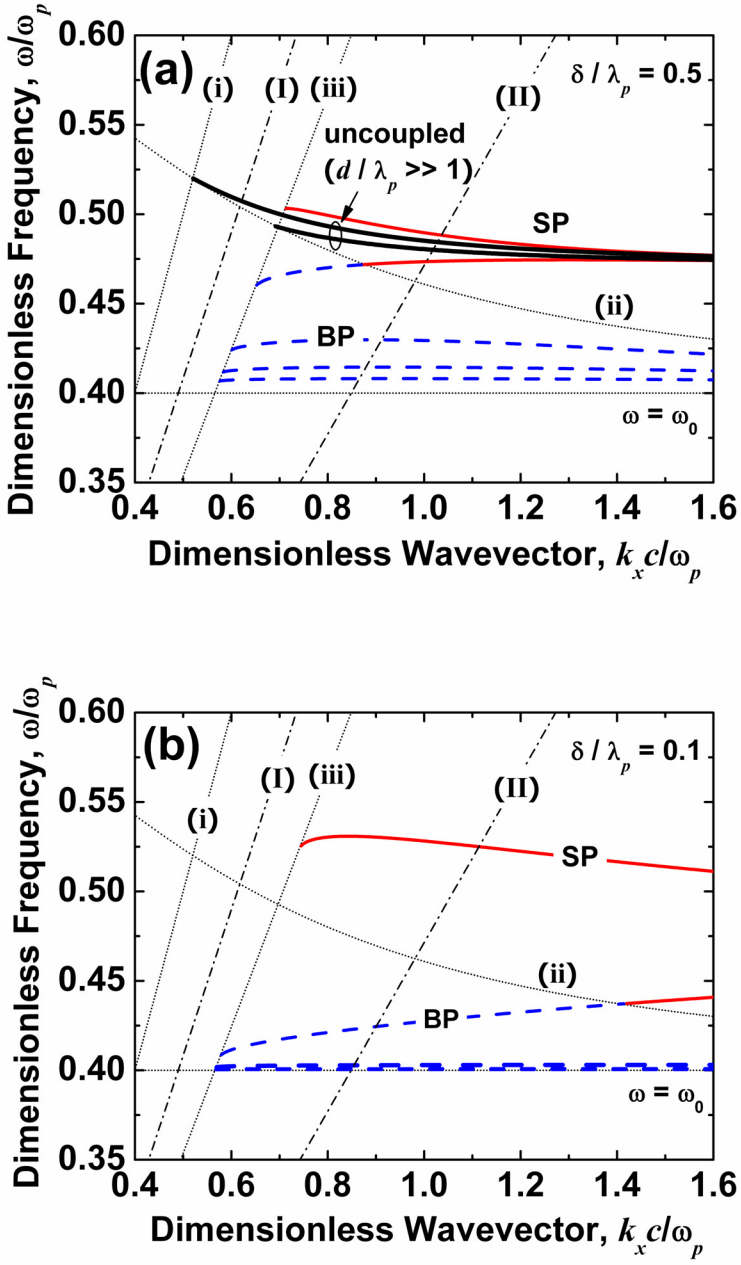

Figure 6.4 Surface and bulk polariton dispersion curves for *s*-polarization with different NIM thicknesses: (a) $\delta/\lambda_p = 0.5$ and (b) $\delta/\lambda_p = 0.1$. Dotted lines are the same as the corresponding ones in Fig. 6.3, with $\varepsilon_1 = 1$ and $\varepsilon_3 = 2$. The dash-dotted lines (I) and (II) represent different angles of incidence. The thin solid curves are for surface polaritons, dashed curves for bulk polaritons, and thick solid curves for uncoupled surface polaritons ($\delta \to \infty$).

In contrast, in a slab of conventional material, surface polaritons exist only in the frequency region of the stop band, in which bulk polaritons are not permitted since they are propagating modes [25]. The thickness of the NIM layer can affect the distribution of bulk polariton modes. For a thick NIM layer, as shown in Fig. 6.4(a), the polariton dispersion curves extend over the frequency range in region BK. When the NIM layer is thin, on the other hand, the dispersion curves except one are crowded near $\omega = \omega_0$, as seen from Fig. 6.4(b). Another feature worthy of mentioning is that the slope of a polariton dispersion curve, $d\omega / dk_x$, represents the group velocity along the *x*-direction. The surface polariton of the higher frequency has a negative group velocity while that of the lower frequency has a positive one. Since the group velocity is equivalent to the energy velocity (or the signal velocity) in the lossless NIM [18], energy propagates along the surface in opposite directions for different surface polariton modes. However, notice that this behavior changes with different layer thicknesses: both modes have negative group velocities under the uncoupled condition (thick curves), and for $\delta = 0.1\lambda_p$, the higher frequency mode has a positive group velocity near line (iii). Bulk polaritons, except that of the first order, have nearly zero group velocity, indicating that most of the bulk polariton modes in the NIM slab do not transmit signal like those in conventional waveguides.

Polaritons for *s*-polarization are observable only within the pass band ($0.4\omega_p < \omega < 0.6\omega_p$). On the contrary, polaritons for *p*-polarization can be excited in the frequency regions $0 < \omega < \omega_0$ and $\omega_0 < \omega < \omega_p$ with different branches, as shown in Fig. 6.5. In general, the dispersion curves for surface polaritons in the low frequency regions (SS2 and SD2 in Fig. 6.3) look similar to those with a metal slab [30]. Nevertheless, an

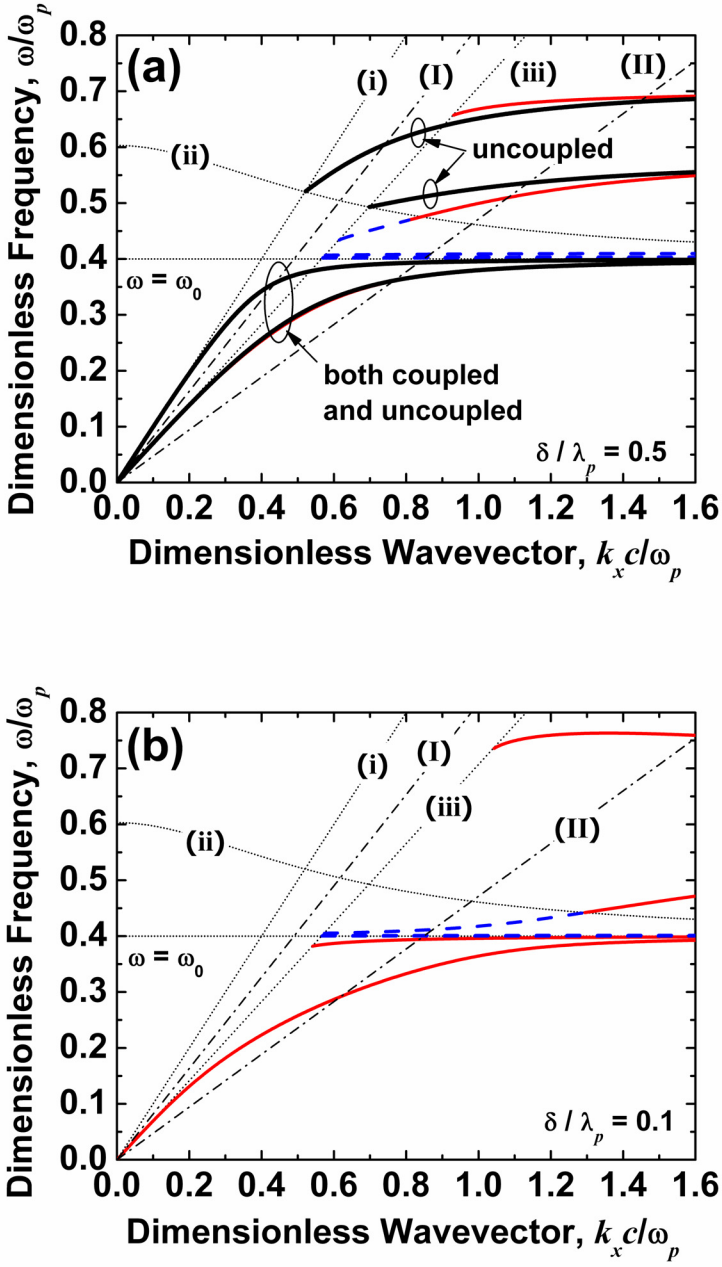

Figure 6.5 Surface and bulk polariton dispersion curves for *p*-polarization: (a) $\delta/\lambda_p = 0.25$ and (b) $\delta/\lambda_p = 0.1$. All other conditions are the same as in Fig. 6.4. Note that in 5(a) below $\omega = \omega_0$, the coupled and uncoupled curves are indistinguishable.

NIM possesses two more surface polariton curves in the high frequency regions (SS1 and SD1), in which the lower frequency curve extends to the boundary between regions SD1 and BK to meet with the first-order bulk polariton curve, similar to the case for *s*-polarization. Figure 5 also shows the change of dispersion curves as *d* is varied. Even though the case of $\delta/\lambda_p = 0.25$ is used instead of $\delta/\lambda_p = 0.5$ as in Fig. 6.4(a), surface polariton dispersion curves in regions SS2 and SD2 are indistinguishable with their uncoupled counterparts (thick solid curves), indicating that surface polaritons for *p*-polarization are not so sensitive to the thickness unless $\delta < 0.25\lambda_p$. From the slopes of polariton dispersion curves in Fig. 6.5, the group velocities of surface polaritons are positive for *p*-polarization.

6.3 Radiative Properties

The ATR configuration is a typical surface polariton coupler. Figure 6.1 illustrates the setup used in the present study. When the incidence angle θ_i is greater than the critical angle $\theta_{cr} = \sin^{-1}(\varepsilon_1/\varepsilon_{prism})^{1/2}$, where ε_{prism} is the relative permittivity of the prism, $k_{z,1}$ becomes purely imaginary and an evanescent wave emerges in the vacuum gap (medium 1 in Fig. 6.2). If the gap width *d* approaches infinity, the evanescent wave will decay exponentially away from the prism and total internal reflection will occur. For a finite *d*, however, the incident photon energy can be coupled to the surface waves (polaritons), causing a reduction in the reflectance, especially near the polariton resonance frequencies. In this case, there are two evanescent waves in the vacuum layer that decay in opposite directions. The electron scattering rate γ, which was set to zero in

obtaining the dispersion curves, must be set to a finite value to account for the inevitable loss (absorption) of the NIM layer (medium 2). As a matter of fact, the reflectance would be unity without absorption in the regions on the right of line (iii) in Figs. 6.3, 6.4, and 6.5, because no energy could be coupled to the surface wave or transmitted to the bottom dielectric (medium 3).

The calculated reflectance R as a function of the dimensionless frequency is shown in Fig. 6.6 with varying NIM layer thicknesses. The angle of incidence $\theta_i = 60\,^\circ$ and the vacuum gap width $d = 0.25\lambda_p$. It is assumed that $\varepsilon_1 = 1$ (vacuum), $\varepsilon_3 = 2$, and $\varepsilon_{prism} = 6$. The parameters for calculating ε_2 and μ_2 remain the same (i.e., $\omega_0 = 0.4\omega_p$ and $F = 0.56$), except the electron scattering rate $\gamma = 0.012\omega_p$. Here, the reflectance and transmittance are computed using the transfer matrix method, for radiation incident from the prism [20,21]. Recall that the dash-dotted line (I) or (II) in Figs. 6.4 and 6.5 is for a fixed angle of incidence, i.e., $\omega = k_x c/(\sqrt{\varepsilon_{prism}}\sin\theta_i)$. With the parameters given above, lines (I) and (II) in these figures correspond to $\theta_i = 30°$ and $\theta_i = 60°$, respectively. At $\theta_i = 60\,^\circ$, an evanescent wave exists in medium 3 and no energy is transmitted. The absorptance is simply $1 - R$.

The shaded region in Fig. 6.6 corresponds to the frequencies where the refractive index of the NIM is negative. Solid curves are for *p*-polarization and dotted ones for *s*-polarization. Several dips, due to surface and bulk polaritons, can be clearly seen in the reflectance spectra. The shape of the reflectance dip may be approximated using a Lorentzian function as with conventional materials [31]. Marks on the reflectance spectra indicate the polariton resonance frequencies obtained from the polariton dispersion

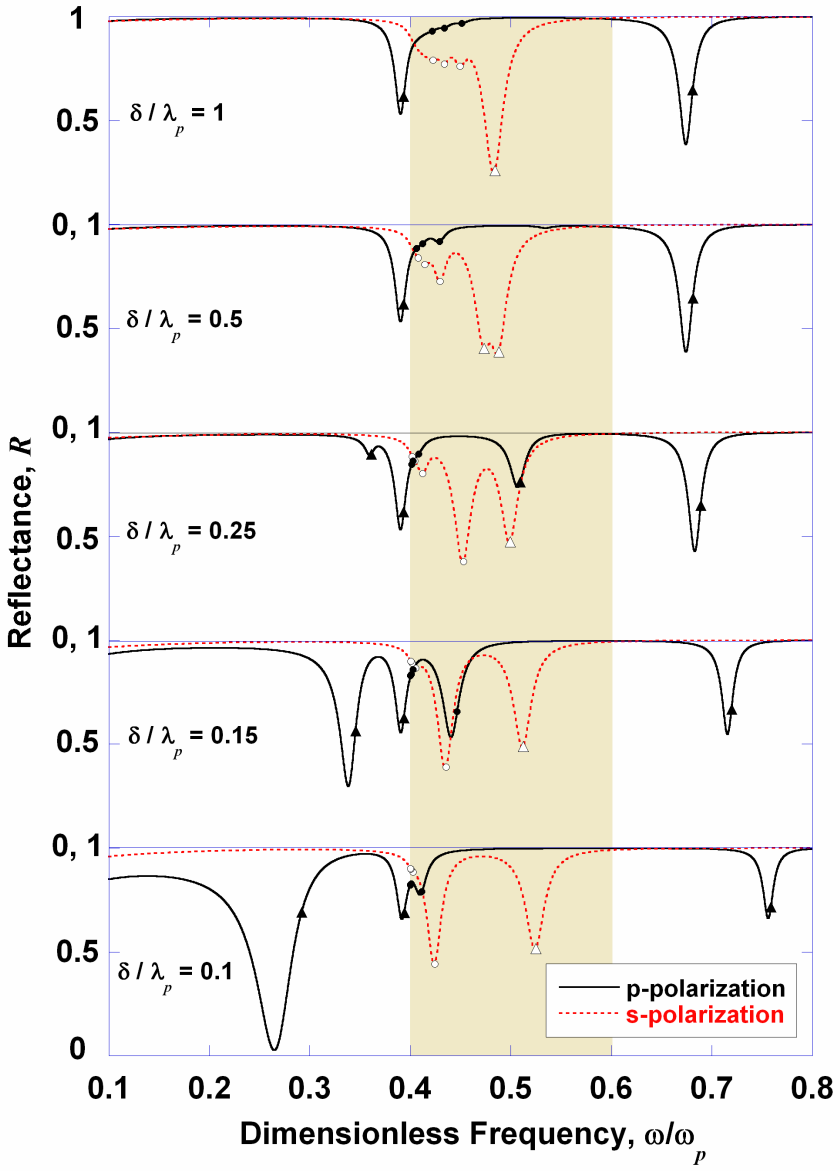

Figure 6.6 The reflectance for different thicknesses of the NIM layer with a vacuum gap width $d = 0.25\lambda_p$. The parameters used for the calculation are $\varepsilon_1 = 1$ (vacuum), $\varepsilon_3 = 2$, $\varepsilon_{prism} = 6$, and $\theta_i = 60°$. For the NIM, $\omega_0 / \omega_p = 0.4$, $F = 0.56$, and $\gamma = 0.012\omega_p$. In the shaded region, the refractive index of the NIM is negative. Solid curves are for *p*-polarization and dotted ones for *s*-polarization. The triangular and circular marks represent, respectively, surface and bulk polariton resonance frequencies obtained from the polariton dispersion relations for $\gamma = 0$.

relations, Eqs. (6.4) and (6.5), for the prescribed conditions (with the exception that $\gamma = 0$). Surface and bulk polaritons are identified with triangular and circular marks (filled for *p*-polarization and unfilled for *s*-polarization), respectively. The solutions from the dispersion relations are illustrated in Figs. 6.4 and 6.5 as the intersections of line (II) with the polariton dispersion curves. Take $\delta/\lambda_p = 0.5$ for *s*-polarization as an example. It can be seen in Fig. 6.4(a) that line (II) intersects with three bulk polariton curves for $0.4 < \omega/\omega_p < 0.45$ and two surface polariton curves for $0.45 < \omega/\omega_p < 0.5$. These frequencies are marked clearly on the dotted curve in Fig. 6.6 (the second panel from the top). When the NIM layer thickness is reduced, the surface polariton of the lower frequency, in the pass band, is converted into a bulk polariton, while the other bulk polaritons are compressed to the vicinity of ω_0 and have little effect on the reflectance. The transition from a surface polariton to a bulk polariton happens at δ/λ_p between 0.25 and 0.5 for *s*-polarization, and between 0.15 and 0.25 for *p*-polarization. Since the electron scattering rate determines the internal damping that is manifested in the reflectance curve as the FWHM (full width at half minimum) of the reflectance dip [32], the finite γ smears the dips at $\omega \approx \omega_0$ into a smooth shoulder for *s*-polarization and a peak for *p*-polarization (bottom panel of Fig. 6.6). If γ is very small, however, the reflectance dips due to bulk polaritons will appear near ω_0.

It should be noted that the polariton dispersion relations presented in the previous section were based on zero γ and infinite *d*; and therefore, they may not predict the exact locations of the reflectance dip. Although the value of γ will affect the magnitude and width of the reflectance dip, it has little influence on the location of the polariton

resonance frequency as long as the associated damping is small [24]. On the other hand, the value of *d* can significantly influence the resonance frequency. As shown in Fig. 6.6, although the predicted polariton resonance frequencies are in excellent agreement with the locations of the reflectance minima for *s*-polarization, there appear to be large discrepancies for *p*-polarization. Usually, the polariton dispersion relations predict a higher frequency than the frequency at which the reflectance reaches a minimum. This deviation suggests that the electromagnetic fields have been perturbed by the presence of the prism and the effect is stronger for *p*-polarization than for *s*-polarization. If the NIM slab is very thick, surface polaritons at the interface between the NIM and the lower dielectric cannot be excited by the incident EM waves. This is the case for $\delta/\lambda_p = 1$, when only polaritons at the upper interface of the NIM are excited. For *p*-polarization even with $\delta/\lambda_p = 0.5$, surface polaritons at the lower interface of the NIM slab are hardly noticeable in the reflectance spectrum.

The reflectance dip, associated with the surface polariton of the lowest frequency ($\omega < \omega_0$), becomes much deeper and broader as δ/λ_p is reduced from 0.25 to 0.1. Furthermore, the frequency at the reflectance minimum is shifted to a much lower frequency than that obtained from the polariton dispersion relations (triangular marks). Since the internal damping due to the nonzero scattering rate γ remains the same, this indicates there is a considerable increase of radiation damping as the NIM layer thickness is reduced. Due to the presence of the prism, the backward evanescent wave in the vacuum layer is coupled into a propagating wave at the bottom of the prism. The back-coupled wave destructively interferes with the reflected wave in the prism to yield a radiation damping effect [1]. As the thickness of a thin metallic film decreases, radiation

damping of the lower-frequency surface polariton mode (symmetric type) increases while that of the higher-frequency surface polariton mode (asymmetric type) decreases [33, 34]. Since the surface polaritons of the NIM layer in region SD2 (i.e., $\omega < \omega_0$) are similar to those for a metallic film, the enhanced radiation damping is therefore responsible for the dramatic changes in the reflectance minimum at the lowest surface polariton resonance (SPR) frequency.

The reflectance spectra for different vacuum gap widths is shown in Fig. 6.7, where the NIM layer thickness is fixed to $\delta = 0.25\lambda_p$ and all other parameters remain the same as in Fig. 6.6. When d is equal to $0.5\lambda_p$ or larger, polaritons do not have much effect on the reflectance because the evanescent wave in the vacuum layer decays exponentially and is only weakly coupled to the polaritons. The second panel of Fig. 6.7 is basically the same as the third panel of Fig. 6.6, except that ω/ω_p is from 0.2 to 0.7 in Fig. 6.7. Reducing the vacuum gap enhances the effectiveness of coupling and results in deeper reflectance dips. For *s*-polarization, when $d/\lambda_p < 0.1$, the SPR frequency starts to shift left, and bulk polariton with higher frequency tends to disappear. When $d/\lambda_p = 0.01$, the reflectance spectra are almost the same as those without the vacuum gap. The change of the reflectance spectrum for *p*-polarization is more apparent. As the vacuum gap width decreases, two reflectance minima at $\omega < \omega_0$ are merged to form one dip with a large width when $d/\lambda_p = 0.1$. As d is further reduced, reflectance in the dip goes up and the dip becomes shallower. One the other hand, the two surface polaritons at higher frequencies shift left, especially the one in the stop band will eventually shift to the pass band (shaded area). The widths of these reflectance dips become broader, due to

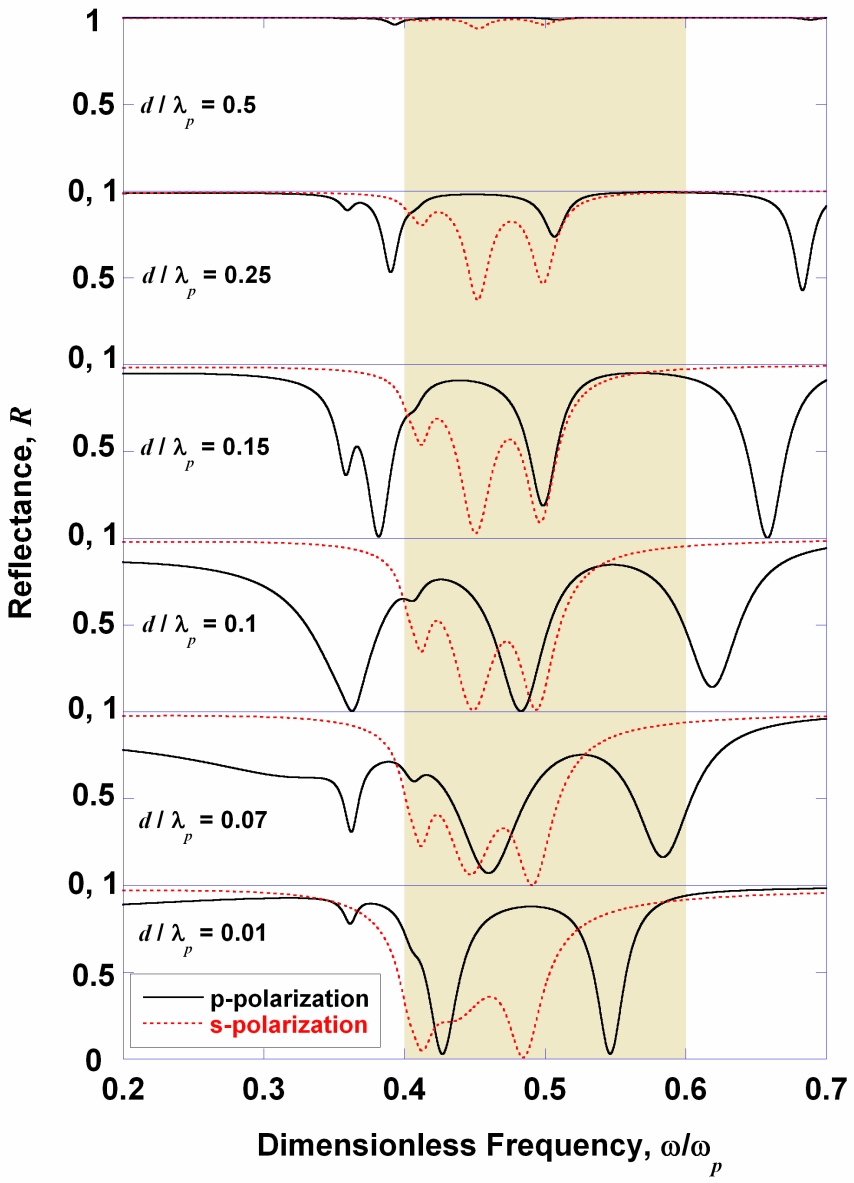

Figure 6.7 Effects of the vacuum gap width on the reflectance for $\delta/\lambda_p = 0.25$. All other parameters used for the calculation remain the same as those for Fig. 6.6.

radiation damping, until $d/\lambda_p = 0.07$. At very small *d*, surface polariton at the upper boundary of the NIM layer has negligible effect on the EM fields as compared to that at the lower boundary, resulting in a weak back-coupled radiation. This is the reason why the width of the reflectance dips becomes smaller at $d/\lambda_p = 0.01$.

Figure 6.8 shows the reflectance, transmittance, and absorptance for *s*-polarization at an angle of incidence of $\theta_i = 30°$ for (a) $\delta = 0.1\lambda_p$ and (b) $\delta = \lambda_p$. All other conditions are the same as in Fig. 6.6. This case is illustrated in Fig. 6.4 as line (I), when evanescent waves exist in the vacuum layer and a propagating wave exists in the bottom dielectric layer. Therefore, energy can be transmitted through the vacuum and the NIM layers via evanescent modes, or photon tunneling [20,21]. The reflectance dip near ω_0 is caused by resonant absorption. For $\delta = \lambda_p$, the reflectance oscillates within $0.4\omega_p < \omega < 0.5\omega_p$, which corresponds to region R4 in Fig. 6.3, due to the wave interference in the NIM layer. The reflectance minimum at $\omega > 0.5\omega_p$ falls in region SS1 in Fig. 6.3, because evanescent waves exist in the NIM layer. Therefore, surface polariton may play a role for this reflectance dip. The diamond marks on the reflectance spectra represent the frequency at the intersection between line (I) and the thick curve in Fig. 6.4. The SPR frequency obtained from the polariton dispersion relation is based on infinite δ and *d*; hence, may deviate from the exact location of the reflectance minimum, because the evanescent fields in the vacuum layer and the NIM layer are strongly perturbed by interfaces between the prism and the vacuum gap and between the NIM layer and the bottom dielectric. Moreover, the frequency corresponding to the reflectance minimum is different from those at the absorptance maximum and the transmittance maximum.

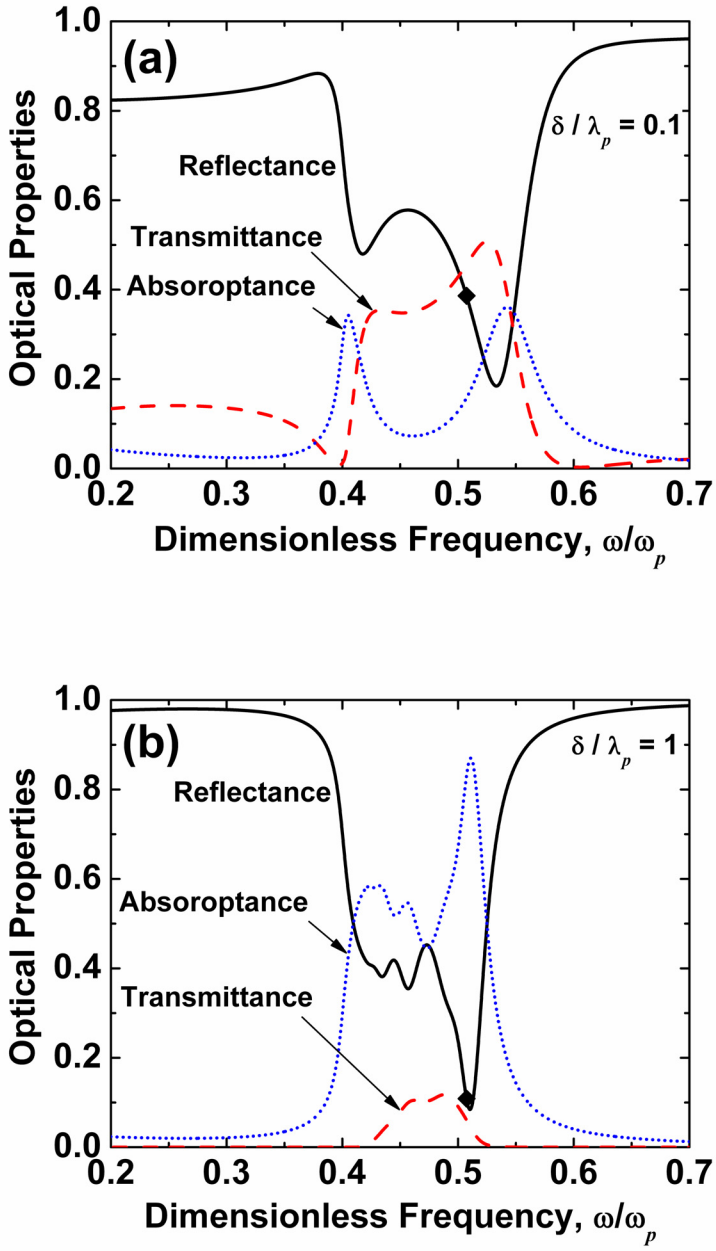

Figure 6.8 Optical properties (i.e., reflectance, transmittance, and absorptance) when (a) $\delta/\lambda_p = 0.1$ and (b) $\delta/\lambda_p = 1$. All the parameters are the same as those used in Fig. 6.6, except that the angle of incidence is changed to $\theta_i = 30°$. Vacuum gap is fixed at $d/\lambda_p = 0.25$. The diamond mark corresponds to the single SPR frequency predicted from the dispersion relations for semi-infinite media.

Nevertheless, it can be evidenced that the surface polariton, together with the geometric parameters, can be used to effectively manipulate the optical properties. For example, a transmittance peak as high as 0.5 can be observed when $\delta/\lambda_p = 0.25$, with the nonzero γ. As pointed out by Zhang and Fu [20,21], the enhancement of transmission through evanescent waves may be applied to microscale thermophotovoltaic energy conversion devices. Similar features can also be observed for *p*-polarization, not shown here, with two dips in the reflectance and two peaks in the transmittance, associated with the single surface polaritons in regions SS1 and SS2 as shown in Fig. 6.3.

6.4 Conclusion

The polariton dispersion relations for surface and bulk polaritons in an NIM layer surrounded by different dielectric media are obtained and presented in a regime map, allowing the identification of different polariton modes. The polariton dispersion curves reveal a unique phenomenon with an NIM slab, that is, a surface polariton can be converted to a bulk polariton, and *vice versa*. The calculated reflectance spectra in an ATR configuration involving an NIM layer show that the thickness of the NIM layer and the vacuum gap width are important parameters that can change the polariton resonance frequency, the reflectance minimum, and width of the reflectance dip. Furthermore, a region in which a surface polariton can be excited only at a single interface of the NIM slab is recognized. In this case, the surface polariton can enhance the transmittance of energy via photon tunneling. The modifications of the radiative properties for multilayer structures using an NIM slab with the assistance of polariton phenomena may have practical applications such as optical imaging and energy transport enhancement.

6.5 References

[1] H. Raether, *Surface Plasmons on Smooth and Rough Surfaces and on Gratings*, Berlin ; New York: Springer-Verlag, 1988.

[2] N. A. Janunts and K. V. Nerkararyan, "Modulation of light radiation during input into waveguide by resonance excitation of surface plasmons," *Applied Physics Letters*, vol. 79, pp. 299-301, 2001.

[3] R. Kohler, A. Tredicucci, F. Beltram, H. E. Beere, E. H. Linfield, G. Davies, D. A. Ritchie, R. C. Iotti, and F. Rossi, "Terahertz semiconductor heterostructure laser," *Physics of Semiconductors 2002, Proceedings*, vol. 171, pp. 145-152, 2003.

[4] T. Tanaka and S. Yamamoto, "Laser-scanning surface plasmon polariton resonance microscopy with multiple photodetectors," *Applied Optics*, vol. 42, pp. 4002-4007, 2003.

[5] A. V. Zayats and I. I. Smolyaninov, "Near-field photonics: surface plasmon polaritons and localized surface plasmons," *Journal of Optics a-Pure and Applied Optics*, vol. 5, pp. S16-S50, 2003.

[6] K. Joulain, J. P. Mulet, F. Marquier, R. Carminati, and J. J. Greffet, "Surface electromagnetic waves thermally excited: Radiative heat transfer, coherence properties and Casimir forces revisited in the near field," *Surface Science Reports*, vol. 57, pp. 59-112, 2005.

[7] A. Narayanaswamy and G. Chen, "Thermal emission control with one-dimensional metallodielectric photonic crystals," *Physical Review B*, vol. 70, 125101, 2004.

[8] B. J. Lee and Z. M. Zhang, "Design and fabrication of planar multilayer structures with coherent thermal emission characteristics," *Journal of Applied Physics*, vol. 100, 063529, 2006.

[9] B. J. Lee and Z. M. Zhang, "Coherent thermal emission from modified periodic multilayer structures," *Journal of Heat Transfer*, vol. 129, pp. 17-26, 2007.

[10] A. Narayanaswamy and G. Chen, "Surface modes for near field thermophotovoltaics," *Applied Physics Letters*, vol. 82, pp. 3544-3546, 2003.

[11] M. Laroche, R. Carminati, and J. J. Greffet, "Near-field thermophotovoltaic energy conversion," *Journal of Applied Physics*, vol. 100, 063704, 2006.

[12] R. A. Shelby, D. R. Smith, and S. Schultz, "Experimental verification of a negative index of refraction," *Science*, vol. 292, pp. 77-79, 2001.

[13] A. A. Houck, J. B. Brock, and I. L. Chuang, "Experimental observations of a left-handed material that obeys Snell's law," *Physical Review Letters*, vol. 90, 137401, 2003.

[14] V. G. Veselago, "Electrodynamics of substances with simultaneously negative values of ε and μ," *Soviet Physics Uspekhi-Ussr*, vol. 10, pp. 509-514, 1968.

[15] R. W. Ziolkowski and E. Heyman, "Wave propagation in media having negative permittivity and permeability," *Physical Review E*, vol. 64, 056625, 2001.

[16] D. R. Smith, D. Schurig, and J. B. Pendry, "Negative refraction of modulated electromagnetic waves," *Applied Physics Letters*, vol. 81, pp. 2713-2715, 2002.

[17] S. Foteinopoulou, E. N. Economou, and C. M. Soukoulis, "Refraction in media with a negative refractive index," *Physical Review Letters*, vol. 90, pp. -, 2003.

[18] Z. M. Zhang and K. Park, "On the group front and group velocity in a dispersive medium upon refraction from a nondispersive medium," *Journal of Heat Transfer*, vol. 126, pp. 244-249, 2004.

[19] J. B. Pendry, "Negative refraction makes a perfect lens," *Physical Review Letters*, vol. 85, pp. 3966-3969, 2000.

[20] Z. M. Zhang and C. J. Fu, "Unusual photon tunneling in the presence of a layer with a negative refractive index," *Applied Physics Letters*, vol. 80, pp. 1097-1099, 2002.

[21] C. J. Fu and Z. M. Zhang, "Transmission enhancement using a negative-refraction layer," *Microscale Thermophysical Engineering*, vol. 7, pp. 221-234, 2003.

[22] R. Ruppin, "Surface polaritons of a left-handed medium," *Physics Letters A*, vol. 277, pp. 61-64, 2000.

[23] S. A. Darmanyan, M. Neviere, and A. A. Zakhidov, "Surface modes at the interface of conventional and left-handed media," *Optics Communications*, vol. 225, pp. 233-240, 2003.

[24] R. Ruppin, "Surface polaritons of a left-handed material slab," *Journal of Physics-Condensed Matter*, vol. 13, pp. 1811-1818, 2001.

[25] K. L. Kliewer and R. Fuchs, "Optical modes of vibration in an ionic crystal slab including retardation - I. Nonradiative region," *Physical Review*, vol. 144, pp. 495-503, 1966.

[26] A. B. Buckman, *Guided Wave Photonics*, Fort Worth: Saunders College Pub., 1992.

[27] D. R. Smith, W. J. Padilla, D. C. Vier, S. C. Nemat-Nasser, and S. Schultz, "Composite medium with simultaneously negative permeability and permittivity," *Physical Review Letters*, vol. 84, pp. 4184-4187, 2000.

[28] V. A. Podolskiy, A. K. Sarychev, and V. M. Shalaev, "Plasmon modes in metal nanowires and left-handed materials," *Journal of Nonlinear Optical Physics & Materials*, vol. 11, pp. 65-74, 2002.

[29] G. Shvets, "Photonic approach to making a material with a negative index of refraction," *Physical Review B*, vol. 67, 035109, 2003.

[30] K. L. Kliewer and R. Fuchs, "Collective electronic motion in a metallic slab," *Physical Review*, vol. 153, pp. 498-512, 1967.

[31] K. L. Kliewer and R. Fuchs, "Theory of dynamical properties of dielectric surfaces," *Advanced Chemical Physics*, vol. 27, pp. 355-541, 1974.

[32] G. S. Kovener, R. W. Alexander, and R. J. Bell, "Surface electromagnetic-waves with damping - I. Isotropic media," *Physical Review B*, vol. 14, pp. 1458-1464, 1976.

[33] D. Sarid, "Long-range surface-plasma waves on very thin metal-films," *Physical Review Letters*, vol. 47, pp. 1927-1930, 1981.

[34] J. J. Burke, G. I. Stegeman, and T. Tamir, "Surface-polariton-like waves guided by thin, lossy metal-films," *Physical Review B*, vol. 33, pp. 5186-5201, 1986.

CHAPTER 7

PERFORMANCE ANALYSIS OF NEAR-FIELD THERMOPHOTOVOLTAIC DEVICES CONSIDERING ABSORPTION DISTRIBUTION

Through this chapter, the radiative energy transfer and conversion processes in near-field thermophotovoltaic (TPV) systems are rigorously investigated by considering local radiation absorption and photocurrent generation in the TPV cell. Radiation heat transfer was modeled using the fluctuation-dissipation theorem in a multilayered structure, and the electric current generation was evaluated based on the photogeneration and recombination of electron-hole pairs in different regions of the TPV cell. The effects of near-field radiation on the photon penetration depth, photocurrent generation, and quantum efficiency were examined in the spectral region of interest. Contrary to previous studies, the rigorous analysis performed in the present work demonstrates that, while the near-field operation can enhance the power throughput, the conversion efficiency is not much improved and may even be reduced. Subsequently, we envisage a modified design of near-field TPV systems that could significantly improve the efficiency.

7.1 Introduction

Along with increasing global concerns on the energy and environment issues, thermophotovoltaics has recently become a promising sustainable energy conversion method [1,2]. Thermophotovoltaic (TPV) devices are energy conversion systems that

generate electric power directly from thermal radiation. Compared to other candidates, TPV devices provide high power density, portability, and silent operation, being attractive in space, military, and microelectronics applications. However, relatively poor conversion efficiency and power throughput should be overcome for wider usage of TPV systems.

To enhance the power throughput and conversion efficiency, a new type of TPV system utilizing the principle of near-field thermal radiation has been recently proposed. Due to near-field effects such as wave interference, photon tunneling, and surface polaritons, the thermal radiation can be enhanced several orders of magnitude larger than the blackbody radiation [3-5]. Thus, locating a TPV cell in the proximity of a thermal emitter would tremendously enhance the photon energy into the cell, resulting in the increase of electric power generation. This so-called near-field TPV system has been intensively studied by several research groups [6-9]. It was Pan et al. [6] that first analyzed the performance of near-field TPV systems. However, they used same dielectric materials for both the emitter and TPV to calculate the near-field energy enhancement, which is not only too simplified but also impractical. Whale and Cravalho [7] considered a more realistic system by using a fictitious Drude material as a thermal emitter and InGaAs as a TPV cell. Narayanaswamy and Chen [8] theoretically demonstrated the effect of surface polaritons in improving the performance of near-field TPV systems. However, their work was focused only on the thermal radiation enhancement, leaving questions about the near-field effect on the photocurrent generation unanswered. Even though Laroche et al. [9] recently provided a detailed analysis on the performance and efficiency of near-field TPV systems, their assumption of 100 % quantum efficiency in

calculating the photocurrent generation ended up with the overestimation of the performance. Indeed, there has been no work that rigorously investigated the performance and efficiency of near-field TPV systems based on the realistic mechanisms of photocurrent generations.

The primary objective of this chapter is to better understand the mechanisms of a near-field TPV system. To this end, absorbed radiative energy distribution and photocurrent generation inside the TPV cell are considered. A direct calculation scheme using the fluctuation-dissipation theorem and dyadic Green's functions for multilayer structures are used to calculate the near-field thermal radiation and its absorption in the TPV cell. Photocurrent generations are calculated by taking into account the photogeneration and recombination of electron-hole pairs in the TPV cell. Through this chapter, near-field effects on thermal radiation absorption, electrical current generation, and resultant quantum efficiency will be thoroughly investigated. The overall energy conversion efficiency as a function of the vacuum gap width will be discussed in detail, through which a better design of the near-field TPV system can be proposed.

7.2 Theory of Near-Field Thermophotovoltaics

7.2.1 Near-field thermal radiation in multilayer

A near-field TPV energy conversion system consists of a TPV cell, a *p*-*n* junction of semiconductor, and a thermal source that are separated with a very small vacuum gap. Figure 7.1(a) illustrates the configuration of a near-field TPV device considered in this work: a thermal source is assumed to be made of tungsten and maintained at $T_H = 2000$ K,

so that the characteristic wavelength of radiation is approximately 1.5 μm. $In_{0.18}Ga_{0.82}Sb$, an alloy of InSb and GaSb, is considered as a TPV cell because it is optimized for the thermophotovoltaic energy conversion due to its low energy bandgap (0.56 eV). For the analysis, the TPV cell is assumed to be maintained with $T_{\mathrm{L}} = 300$ K.

The radiative power absorption inside the TPV cell is elucidated by a direct calculation scheme using the fluctuation-dissipation theorem and the dyadic Green's function of Maxwell's equations for a multilayered structure, as shown in Fig. 7.1(a). Since the direct calculation scheme can calculate the incoming radiative heat flux of individual layers, dividing the TPV cell into discrete thin layers can provide the power absorption in each layer. The whole TPV system is thus configured with (N+1) layers, where the first and second layers are respectively the semi-infinite tungsten emitter and the vacuum gap, and the last layer is the semi-infinite $In_{0.18}Ga_{0.82}Sb$ substrate: the *p*-*n* junction part of the TPV cell is divided into (N-2) layers.

The Fourier components of the electrical and magnetic fields for a non-magnetic material can be expressed in terms of the dyadic Green's function as a volume integration [10]:

$$\begin{aligned} \mathbf{E}(\mathbf{x},\omega) &= j\omega\mu_0 \int_V \overline{\overline{\mathbf{G}}}_e(\mathbf{x},\mathbf{x}',\omega)\cdot\mathbf{J}(\mathbf{x}',\omega)d\mathbf{x}' \\ \mathbf{H}(\mathbf{x},\omega) &= \int_V \overline{\overline{\mathbf{G}}}_h(\mathbf{x},\mathbf{x}',\omega)\cdot\mathbf{J}(\mathbf{x}',\omega)d\mathbf{x}' \end{aligned} \tag{7.1}$$

where $j=\sqrt{-1}$, μ_0 is the magnetic permeability of free space. In the above equation, $\overline{\overline{\mathbf{G}}}_e(\mathbf{x},\mathbf{x}',\omega)$ and $\overline{\overline{\mathbf{G}}}_h(\mathbf{x},\mathbf{x}',\omega)$ are the electric and magnetic dyadic Green's function due to a delta source positioned at $\mathbf{x}'$ and are related by $\overline{\overline{\mathbf{G}}}_h(\mathbf{x},\mathbf{x}',\omega)=\nabla_{\mathbf{x}}\times\overline{\overline{\mathbf{G}}}_e(\mathbf{x},\mathbf{x}',\omega)$. $\mathbf{J}(\mathbf{x}',\omega)$ is the Fourier component of the space-time dependent electric current density,

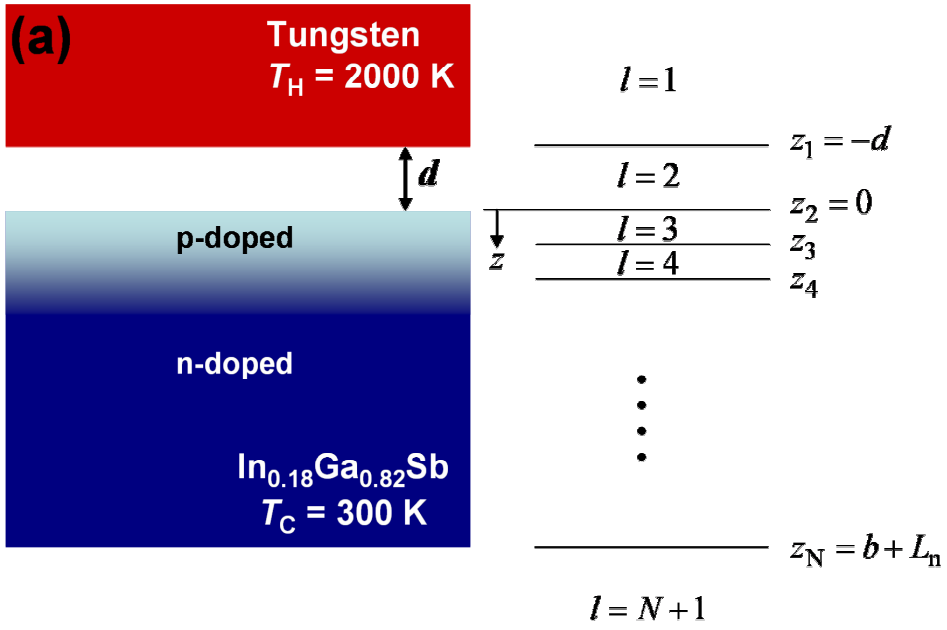

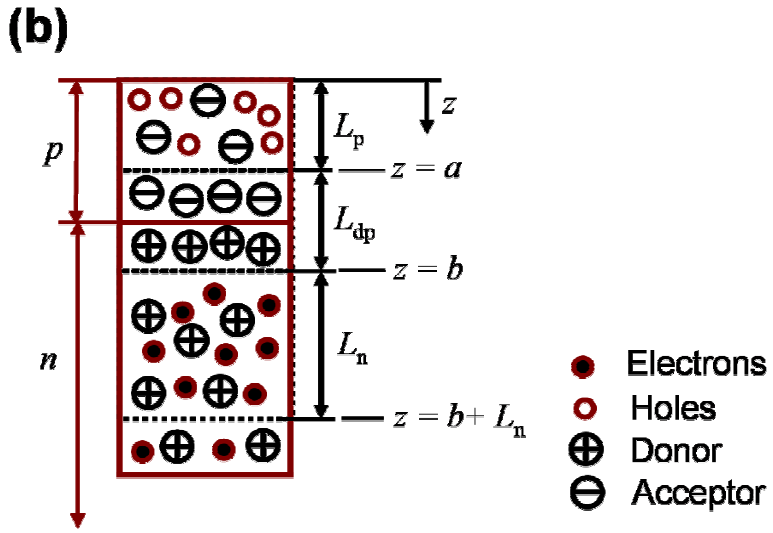

Figure 7.1 (a) Schematic of a near-field TPV system, where $In_{0.18}Ga_{0.82}Sb$ is used as the TPV cell material while plain tungsten is used as the emitter. Both the emitter and the cell material are modeled as semi-infinite media. (b) Illustration of the minority carrier diffusion lengths and depletion region in a *p-n* junction; not to scale.

$\mathbf{J}(\mathbf{x}',t)$, that is produced by the random thermal fluctuations. According to the fluctuation-dissipation theorem, thermal radiation is originated from the random movement of charges or dipoles inside the medium at temperatures over zero Kelvin. More detailed discussion on the fluctuation-dissipation theorem can be found in [4]. The spatial correlation between the fluctuating current densities at two locations $\mathbf{x}'$ and $\mathbf{x}''$ can be expressed as [10]

$$\left\langle J_m(\mathbf{x}',\omega)J_n^*(\mathbf{x}'',\omega)\right\rangle = \frac{4\omega\varepsilon_0\,\mathrm{Im}(\varepsilon_s)\Theta_r(\omega,T)}{\pi}\delta_{mn}\delta(\mathbf{x}'-\mathbf{x}'') \quad (7.2)$$

where * denotes complex conjugate, ε_0 is the electric permittivity of free space, $\mathrm{Im}(\varepsilon_s)$ is the imaginary part of the dielectric function of the source, δ_{mn} is the Kronecker delta function, $\delta(\mathbf{x}'-\mathbf{x}'')$ is the Dirac delta function. $\Theta_r(\omega,T)=\hbar\omega/[\exp(\hbar\omega/k_BT)-1]$, where $\hbar$ is Planck's constant h over 2π and k_B is Boltzmann's constant, is the mean energy of a Planck oscillator at frequency ω in thermal equilibrium. To compute the radiative heat transfer, the time-averaged Poynting vector should be calculated with the following equation:

$$\mathbf{S}_\omega(\mathbf{x},\omega)=\frac{1}{2}\left\langle \mathrm{Re}\left[\mathbf{E}(\mathbf{x},\omega)\times\mathbf{H}^*(\mathbf{x},\omega)\right]\right\rangle \quad (7.3)$$

Note that a factor of four has been included in Eq. (7.2) to be consistent with the conventional definition of the Poynting vector that consideres only positive values of frequencies [11].

Substitution of Eq. (7.1) into Eq. (7.3) yields the Poynting vector equation solely dependent upon the dyadic electrical Green's function. Thus, the problem of determining the radiative heat transfer is converted to a problem of determining the Green's function

for a given case. The Green's function technique for multilayered structures has been extensively studied [12,13] and applied to the calculation of the thermal radiation in one-dimensional (1-D) photonic crystals [14,15]. Since only the homogeneous case, the case that the thermal source does not reside in the layer of concern, is taken into account, the Green's function can be written as

$$\bar{\bar{\mathbf{G}}}_e(\mathbf{x},\mathbf{x}',\omega)=\frac{j}{4\pi}\int\frac{KdK}{\beta_s}F(K)e^{jK(r-r')} \tag{7.4}$$

with $F(K)=Ae^{j(\beta_l z-\beta_s z')}\hat{\mathbf{e}}_l^+\hat{\mathbf{e}}_s^+ + Be^{j(-\beta_l z-\beta_s z')}\hat{\mathbf{e}}_l^-\hat{\mathbf{e}}_s^+ + Ce^{j(\beta_l z+\beta_s z')}\hat{\mathbf{e}}_l^+\hat{\mathbf{e}}_s^- + De^{j(-\beta_l z+\beta_s z')}\hat{\mathbf{e}}_l^-\hat{\mathbf{e}}_s^-$. Here, K is the parallel component of the wavevector. The subscript *s* denotes the source layer (i.e., $l=1$), indicating that $\beta_s=\sqrt{k_s^2-K^2}$ is the *z*-component of the wavevector at the source layer. Note that $\mathbf{k}_l=K\hat{\mathbf{r}}+\beta_l\hat{\mathbf{z}}$ is the wavevector in the *l*-th layer, where $\hat{\mathbf{r}}$ and $\hat{\mathbf{z}}$ are the unit vectors of the cylindrical coordinates. Similarly, $\beta_l=\sqrt{k_l^2-K^2}$ is the *z*-component of the wavevector at the *l*-th layer when $l>2$. The space variables at the *l*-th layer and the source layer can be respectively written as $\mathbf{x}=r\hat{\mathbf{r}}+z\hat{\mathbf{z}}$ and $\mathbf{x}'=r'\hat{\mathbf{r}}+z'\hat{\mathbf{z}}$. Provided that $k_l=\varepsilon_l k_0=\varepsilon_l\omega/c$, where c is the speed of light in free space, the dielectric constants should be determined for the calculation of the wavevector magnitude. The dielectric constant of tungsten, ε_s, was taken from Ref. [16], and that of $In_{0.18}Ga_{0.82}Sb$, ε_l, was taken from Ref. [17]. The unit vectors $\hat{\mathbf{e}}^+$ and $\hat{\mathbf{e}}^-$ are the upward and downward vector, respectively. Note that $\hat{\mathbf{e}}$ can be either a unit vector perpendicular to the plane of incidence (TE) or a unit vector parallel to the plane of incidence (TM), depending on the polarization in consideration: for TE-wave, $\hat{\mathbf{e}}_l^+=\hat{\mathbf{e}}_l^-=\hat{\mathbf{r}}\times\hat{\mathbf{z}}$ and for TM-wave,

$\hat{\mathbf{e}}_l^+ = (K\hat{\mathbf{z}} - \beta_l \hat{\mathbf{r}})/k_l$ and $\hat{\mathbf{e}}_l^- = (K\hat{\mathbf{z}} + \beta_l \hat{\mathbf{r}})/k_l$ [12]. The coefficients A, B, C, and D represent different patterns of the electrical and magnetic field propagation from the source point, and can be determined using the transfer matrix method [18].

The total radiative heat flux propagating to the l-th layer in the TPV cell can be quantified by integrating the Poynting vector in z-direction at the position $z = z_l$ over the entire spectrum,

$$P_R(z_l) = \int_0^\infty S_{z,\omega}(z_l, \omega) d\omega \tag{7.5}$$

or alternatively, $$P_R(z_l) = \int_0^\infty S_{z,\lambda}(z_l, \lambda) d\lambda \tag{7.6}$$

based on the wavelength in free space, λ. The radiative power absorption can thus be obtained by subtracting the radiative heat flux to the (l+1)-th layer from that to the l-th layer. Note that $S_{z,\lambda}$ is the net Poynting vector in which the thermal radiation from the TPV cell to the thermal emitter is taken into account.

7.2.2 Photocurrent generation in TPV cell

Figure 7.1(b) is a schematic of the $In_{0.2}Ga_{0.8}Sb$ TPV cell being considered. For TPV cells, p-on-n configuration is preferred over n-on-p because the annealing of the ohmic contact to the n-type material may result in a short circuit at the junction [19]. A doping concentration of the p-layer is set to 10^{19} cm^{-3} whilst the Tellurium-doped n-layer is set to have a doping concentration of 10^{17} cm^{-3}. The concentration gradient of the majority carriers across the p-n junction diffuses electrons from the n-to p-region and vice versa for the holes. As a result, the depletion region having only ionized dopants is

formed at the junction, as shown in Fig. 1(b) between $z = a$ and $z = b$. The depletion region width, L_{dp}, estimated from the given doping concentrations is 0.1 μm [12].

When thermal radiation is incident on the TPV cell that has energy bandgap E_{g}, photons whose energy is greater than E_{g} generate electron-hole pairs inside the TPV cell. The photogeneration rate of electron-hole pairs in the *l*-th layer can be written as

$$g_l(\lambda) = \frac{Q_{\lambda,l}}{d_l hc/\lambda} \tag{7.7}$$

Here, d_l is the thickness of the *l*-th layer, and $Q_{\lambda,l}$ is the absorbed spectral radiative power in the *l*-th layer, which can be obtained by calculating the Poynting vector in *z*-direction as discussed in the previous section. However, not all the generated electron-hole pairs contribute to the photocurrent: While pairs generated in the depletion region are swept by the built-in electric field and completely contribute to the generation of a drift current without recombination, the electron-hole pairs generated outside the depletion region experience recombination and minority carriers are diffused to the edge of the depletion region. The drift current generated within the depletion region is then simply expressed as

$$J_{dp}(\lambda) = e g_{dp}(\lambda) L_{dp} \tag{7.8}$$

where L_{dp} is the thickness of the depletion region. Note that Eq. (7.7) is used for $g_{dp}(\lambda)$ except d_l is replaced by L_{dp}. In order to compute the photocurrent generated outside the depletion region, minority carrier concentration at *p*- and *n*-region should be first calculated. Due to its diffusive feature, the minority carrier concentration in the *p*-region can be expressed with the following 1-D, steady state continuity equation [20]:

$$D_e \frac{d^2 n_e}{dz^2} - \frac{n_e - n_e^0}{\tau_e} + g(z,\lambda) = 0 \tag{7.9}$$

where D_e is the electron diffusion constant [21]; n_e is the local electron concentration; n_e^0 is the equilibrium electron concentration; and τ_e is the electron relaxation time. Note that the second term of Eq. (9) represents the recombination rate. $g(z,\lambda)$ is the photogeneration rate of electron-hole pairs and can be discretized from the near-field radiative heat transfer calculation. Discretized formulation of $g(z,\lambda)$ to $g_l(\lambda)$ using Eq. (7.7) allows the straightforward application of finite difference method (FDM) in solving Eq. (9). Equation (9) is a second order equation and hence needs two boundary conditions. The boundary condition at the interface of the depletion region (i.e., $z = a$) is $n_e = n_e^0$ because the minority carriers are collected by the electric field [20]. At the surface of the TPV cell (i.e., $z = 0$), strong recombination processes occur due to surface defects and other metallic contacts, providing the following boundary condition:

$$D_e \left. \frac{dn_e}{dz} \right|_{z=0} = S_p [n_e(0) - n_e^0] \tag{7.10}$$

where S_p is the surface recombination velocity. In fact, S_p significantly affects the quantum efficiency especially at high photon energies [22,23], and will be discussed later in more detail. The photocurrent generated in the *p*-region is given by the gradient of the carrier concentration at the edge of the depletion region interface:

$$J_e(\lambda) = eD_e \left. \frac{dn_e}{dz} \right|_{z=a} \tag{7.11}$$

where J_e is the electron diffusion current. The photocurrent in the *n*-region, $J_h(\lambda)$, can be obtained from Eqs. (7.9) and (11) by replacing D_e, n_e, and τ_e with D_h, n_h, and τ_h,

respectively. The boundary condition at the interface of the depletion region (i.e., $z = b$) is $n_h = n_h^0$. At the other edge (i.e., $z = b + L_n$), recombination is not considered because the *n*-region is typically fabricated to be thicker than the hole diffusion length, or $L_n > \sqrt{D_h \tau_h}$. Hence the surface recombination velocity S_n is set to 0 in Eq. (7.10). It should be noted that the electron and hole distributions are dependent upon the incident radiation and hence the diffusion currents are wavelength-dependant quantities. The spectral photocurrent is the summation of the different photogenerated currents, $J_\lambda(\lambda) = J_e(\lambda) + J_h(\lambda) + J_{dp}(\lambda)$. All the parameters used in this work are tabulated in Table 7.1.

Table 7.1 Parameters used for the calculation of photocurrent generation

Parameter	*p*-region	*n*-region
Carrier concentration	$N_A = 10^{19}$ cm^{-3}	$N_D = 10^{17}$ cm^{-3}
Diffusion coefficient [24]	$D_e = 125$ cm^2/s	$D_h = 31.3$ cm^2/s
Relaxation time [17]	$\tau_e = 9.75$ ns	$\tau_h = 30.8$ ns
Surface recombination velocity [23]	$S_p = 7.4 \times 10^4$ m/s	$S_n = 0$ m/s
Region width	$L_p = 0.4$ μm	$L_n = 10$ μm

The performance of TPV systems can be evaluated through two efficiencies: quantum efficiency, η_q, and conversion efficiency, η. The quantum efficiency is defined

as the ratio of the number of useful electron-hole pairs generated to the number of photons absorbed, and can be written as

$$\eta_q(\lambda) = \frac{J_\lambda hc/\lambda}{eS_{z,\lambda}(0,\lambda)} \tag{7.12}$$

under the assumption that the TPV cell is semi-infinite. The conversion efficiency, or simply efficiency, is defined as the ratio of the maximal electric power generated from a TPV cell to the absorbed thermal radiative heat flux. The generated electrical power can be obtained with an open-circuit voltage and the photogenerated current. Due to charge accumulation at the two electrodes of the TPV cell, an open-circuit voltage develops across the terminals of the cell. The open-circuit voltage is expressed as [25]

$$V_{oc} = \frac{k_B T}{e} \ln\left(\frac{J_{ph}}{J_0}\right) \tag{7.13}$$

where J_{ph} is the photocurrent and J_0 is the dark current. The total photocurrent is the integration of $J_\lambda(\lambda)$ over the spectrum, or alternatively,

$$J_{ph} = \frac{e}{hc}\int_0^{\lambda_g} \eta_q(\lambda) S_{z,\lambda}(0,\lambda)\lambda d\lambda \tag{7.14}$$

where λ_g is the bandgap wavelength. Note that the integration is taken over the spectral region having energy greater than the energy bandgap. The expression of the dark current can be easily derived [24],

$$J_0 = e\left(\frac{n_i^2 D_h}{N_D\sqrt{\tau_h}} + \frac{n_i^2 D_e}{N_A\sqrt{\tau_e}}\right) \tag{7.15}$$

It can be shown that the maximal output electric power is written as

$$P_E = J_{ph} V_{oc} \left[1 - \frac{1}{\ln\left(J_{ph}/J_0\right)} \right] \left\{ 1 - \frac{\ln\left[\ln\left(J_{ph}/J_0\right) \right]}{\ln\left(J_{ph}/J_0\right)} \right\} \tag{7.16}$$

by taking into account the current-voltage diode characteristics, $J = J_{ph} - J_0[\exp(eV/k_BT) - 1]$ [24]. Thus, the efficiency can be obtained from the following equation:

$$\eta = \frac{P_E}{P_R(0)} \tag{7.17}$$

7.3 Results and Discussion

In order to accurately predict the performance of the near-field TPV system, the absorption pattern of the near-field thermal radiation inside the TPV cell must be clearly understood. Figure 7.2(a) shows the spectral distribution of the thermal radiation propagating into the TPV cell when the tungsten emitter-TPV cell distance is 10 nm. As expected, the spectral power is maximal at 1.5 μm, which is the characteristic wavelength of the thermal radiation at 2,000 K. The absorption pattern represents the exponential decay out of the surface, which is due to the extinction coefficient of $In_{0.18}Ga_{0.82}Sb$. However, the radiative power whose wavelength is larger than 2.22 μm propagates through without absorption, as the photon energy is smaller than the energy bandgap of $In_{0.18}Ga_{0.82}Sb$. At $z = 5$ μm, the radiative energy greater than the energy bandgap is almost zero whilst the energy smaller than the bandgap remains almost constant. Figure 7.2(b) shows the radiative power distribution against the parallel component of the wavevector when the wavevector is 1.5 μm and the gap width is d = 10 nm. Here, the

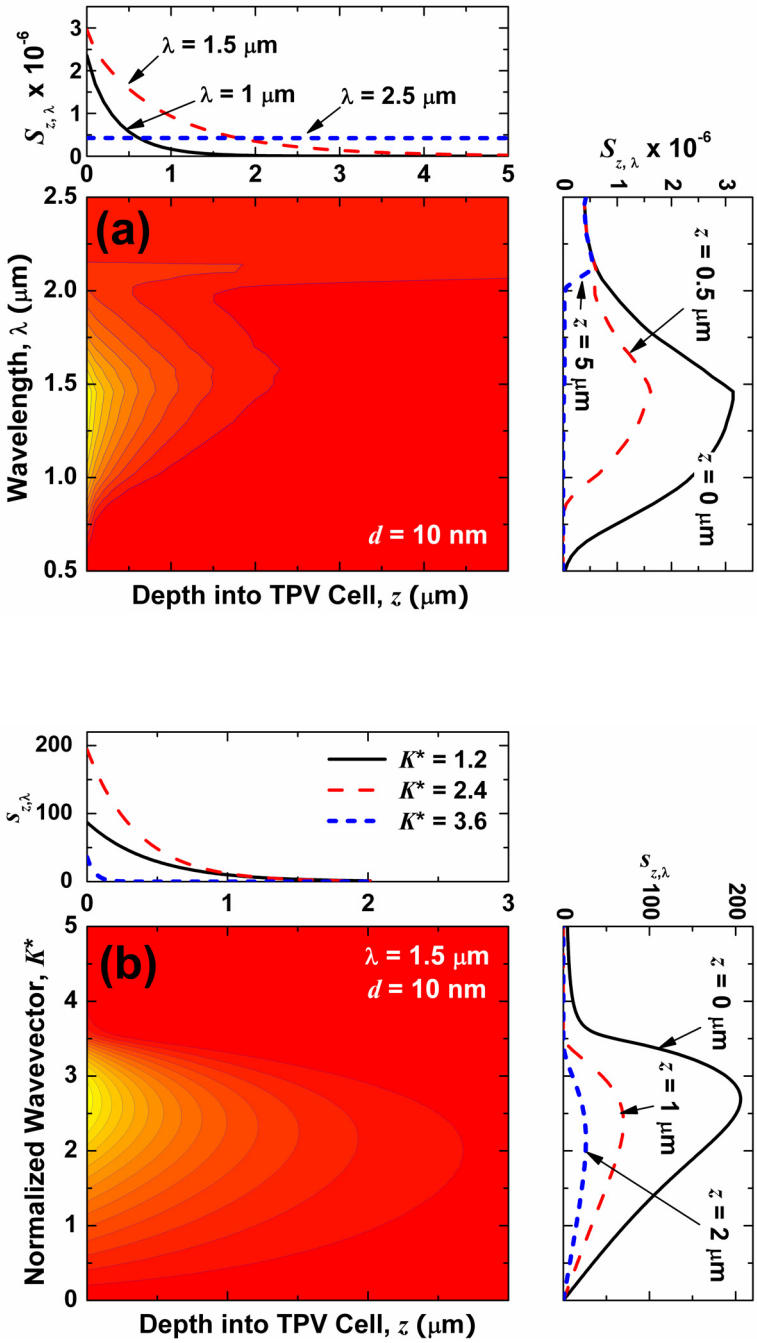

Figure 7.2 (a) Spectral distribution of the incident radiative power when the vacuum gap between the emitter and cell is d = 10 nm. Beyond $\lambda = 2.22$ μm, there is very little absorption, indicating that 2.22 μm is the wavelength corresponding to the energy bandgap. (b) Power distribution at a wavelength of 1.5 μm with respect to K, which is the parallel component of the wavevector, for the same d.

wavevector-based spectral radiative power $s_{z,\lambda}$ is defined such that $S_{z,\lambda}$ is expressed as $S_{z,\lambda} = \int_0^\infty s_{z,\lambda} dK$. Also, the parallel wavevector K is normalized with the wavelength, yielding $K^* = K\lambda / 2\pi$. From the definition of K^* and $\beta_0 = \sqrt{(2\pi/\lambda)^2 - K^2}$, where β_0 is the perpendicular component of the wavevector in vacuum, it is clear that the power distribution above $K^* = 1$ is attributed to the near-field effect due to the photon tunneling [4]. In Fig. 7.2(b), $s_{z,\lambda}$ is the maximum at $K^* \approx 2.7$ when $z = 0$ μm, but the maximum position shifts to a smaller K^* as the radiation propagates into the TPV cell: that is, the penetration depth of $s_{z,\lambda}$ depends on the parallel component of the wavevector. The dependence of the penetration depth on K^* can also be found from the propagation patterns of the radiation for different K^*, as shown in the horizontal profile of Fig. 7.2(b). As K^* increases, the radiation decays faster into the TPV cell, indicating that the penetration depth decreases with K.

More investigation of the penetration depth for near-field thermal radiation will provide a physical insight on the performance of near-field TPV systems. The penetration depth of $s_{z,\lambda}$, δ_K, can be calculated from the electromagnetic description of the thermal radiation. The thermal radiation is proportional to $\exp[-2\,\mathrm{Im}(\gamma)z]$, allowing the definition of δ_K as the depth into the TPV cell for the radiation to be reduced to e^{-1} of the incident radiation: that is, $\delta_K \equiv 1/2\,\mathrm{Im}[(\varepsilon_l k_0^2 - K^2)^{1/2}]$. Figure 7.3(a) shows the calculated δ_K and $s_{z,\lambda}(z = 0)$ when different emitter-cell gaps are considered and the wavelength is fixed at 1.5 μm. In the top figure, the decreasing rate of δ_K is slow until

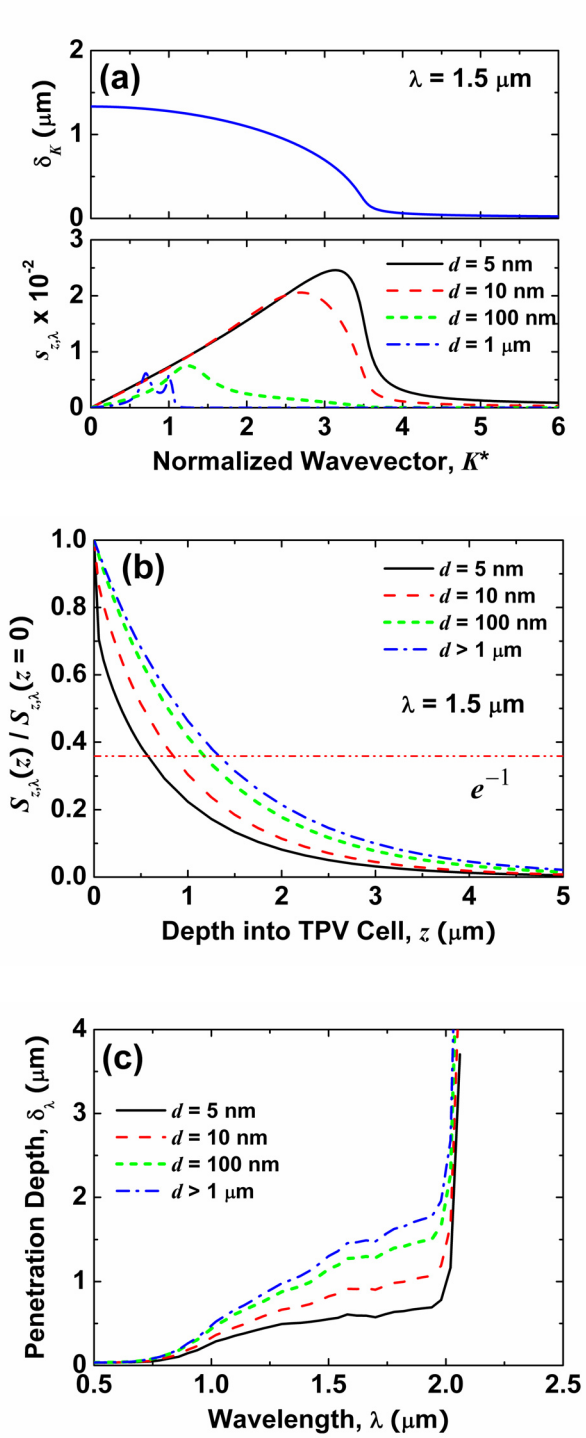

Figure 7.3 (a) The penetration depth and incident radiative power distribution versus K for different values of d at $\lambda = 1.5$ μm. As the gap width decreases, the peak position of thermal radiation shifts to larger K, indicating that a substantial amount of near-field energy enhancement cannot penetrate through the TPV cell. (b) Propagation patterns of thermal radiation for different gap widths for $\lambda = 1.5$ μm. The horizontal dash-dot line at e^{-1} clearly illustrates the dependence of the penetration depth on d. (c) Spectral distribution of the penetration depth for different gap widths. Notice that beyond $\lambda = 2.22$ μm, the penetration depth is very large due to the small absorption coefficient of the cell material.

$K^* \approx 1$ but becomes steeper afterwards, finally leading to negligibly small δ_K at $K^* \approx 4$. On the other hand, the bottom plot clearly shows that as the gap decreases, $s_{z,\lambda}$ is strongly enhanced and its distribution shifts to larger K^*, due to the increasing photon tunneling effect. At $d = 1$ μm, for example, the energy distribution is restricted to nearly $K^* \simeq 1$ and its value is relatively small, indicating weak near-field effects. When the gap width is 5 nm, however, strong near-field effects not only greatly enhance the thermal radiation but also move the peak position to $K^* \approx 3.2$, where the penetration depth is very small. This shift of the peak position to larger K thus suggests that much more thermal radiation should be absorbed near the surface for smaller gaps. This speculation can be verified in Fig. 7.3(b), where the propagation profiles of the spectral thermal radiation, $S_{z,\lambda}$, are plotted against the depth into the TPV cell when the wavelength is fixed at 1.5 μm. Despite similar exponential decaying patterns, the way the thermal radiation is absorbed inside the TPV cell is obviously dominated by the near-field effects: more energy is absorbed near the surface as the gap becomes smaller. Thus, when the energy penetration depth is defined as the depth at which the thermal radiation is reduced to e^{-1} of the incident value, it is clear from the dash-dot line in Fig. 7.3(b) that the penetration depth of the near-field thermal radiation is dependent upon the vacuum gap. Figure 7.3(c) shows the penetration depth as a function of the wavelength for different vacuum gaps. At short wavelength, i.e., $\lambda < 0.75$ μm, the penetration depth is very small and does not depend on the gap width. When the wavelength is larger than the bandgap wavelength, i.e., $\lambda > 2.22$ μm, the penetration depth exceeds the *p*-*n* junction width and does not also depend on the vacuum gap. Huge difference of the penetration depth due to

the near-field effects occurs at $0.75\ \mu m < \lambda < 2.22\ \mu m$, which is the spectrum region that is responsible for the most photocurrent generation in $In_{0.18}Ga_{0.82}Sb$ TPV cell. At $\lambda = 1.5$ μm, for example, the penetration depth for d = 5 nm is approximately 750 nm, less than half of the far-field penetration depth. Since considerable amount of energy is absorbed very near the surface, the electron-hole pairs generated due to the near-field radiation will be more vulnerable to the recombination and thus less contributable to the current generation.

Figure 7.4 shows the spectral distribution of thermal radiation, current generation, and resultant quantum efficiency for various vacuum gaps. In Fig. 7.4(a), the thermal radiation that is incident on the TPV cell is plotted as a function of wavelength. It should be noted that the TPV cell is assumed to be semi-infinite; hence all the incident thermal radiation is absorbed in the TPV cell. The thermal radiation is enhanced more than one order of magnitude as the vacuum gap decreases from far-field to 5 nm. The near-field enhancement can also be found in the photocurrent generation shown in Fig. 7.4(b). Since the current generation is proportional to the photogeneration rate of electron-hole pairs expressed in Eq. (7.7), the photocurrent enhancement at smaller gaps is attributed to the near-field enhancement of the thermal radiation. However, the thermal radiation beyond the bandgap wavelength does not contribute to the current generation. Figure 7.4(c) compares the quantum efficiencies for different vacuum gaps. Until the gap is reduced to 100 nm, the quantum efficiency remains almost the same with far-field quantum efficiency. The lower quantum efficiency at short wavelength region is mainly due to strong surface recombination. It is known that the surface recombination velocity has a profound effect on the quantum efficiency at high photon energies [22]: higher surface

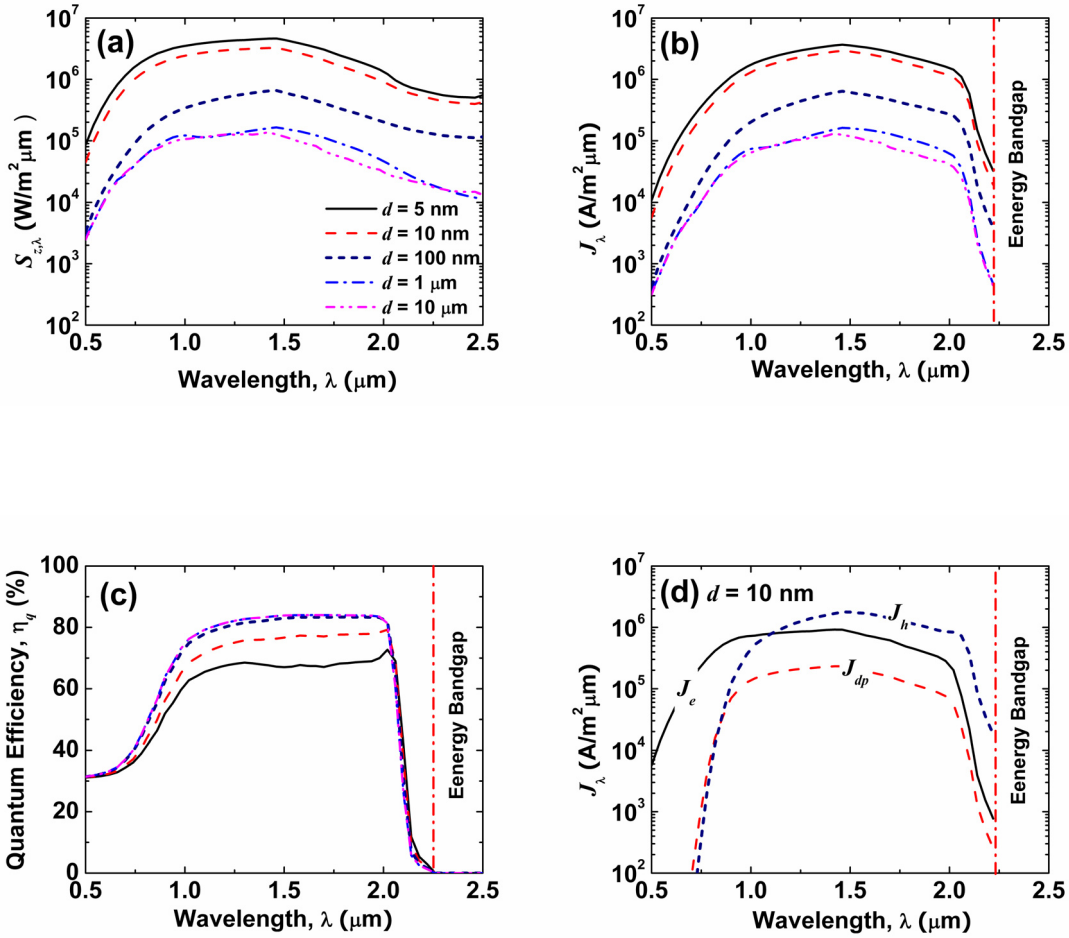

Figure 7.4 Spectral distribution of (a) the radiative power incident on the TPV cell, (b) photocurrent density, (c) quantum efficiency, and (d) current densities generated in the *p*-, *n*-, and depletion regions for different gap widths. Note that the photocurrent and quantum efficiency in (b) and (c) are zero at wavelengths longer than the bandgap wavelength.

recombination velocity resulting from surface defects and metallic contacts induces strong recombination of electron-hole pairs at the surface, degrading the quantum efficiency at short wavelength region having a strong absorption coefficient. The same reason can be applied to the drastic decrease of the quantum efficiency at vacuum gaps smaller than 100 nm. Strong absorption near the surface leads to the strong surface recombination and, correspondingly, lower quantum frequency. For large wavelength, the quantum efficiency drops to zero, representing no contribution of thermal radiation beyond the bandgap wavelength to the photocurrent generation. Figure 7.4(d) shows the spectral distribution of photocurrents generated at each region of the TPV cell when the vacuum gap is maintained with d = 10 nm. As expected from the above discussion, J_e at *n*-region is a dominant photocurrent mode at short wavelength because of the strong radiation absorption near the surface. As the wavelength increases, J_h at *p*-region starts dominating over J_e because the radiation can penetrate further to *p*-region, whose width is much larger than that of *n*-region and thus have more chance of photocurrent generation. On the other hand, although electron-hole pairs in the depletion region do not experience recombination, the small thickness of the depletion region makes it the least responsible for current generation.

From the calculated photocurrent and near-field thermal radiation, the conversion efficiency of the near-field TPV system can be obtained. Figure 7.5(a) shows the total photocurrents as a function of the gap width. In general, J_h is larger than J_e due to the large thickness of *p*-region over *n*-region. However, when the vacuum gap is very small, i.e., $d < 5$ nm, J_e becomes larger than J_h because the enhanced near-field thermal radiation is absorbed very near the surface. The sum of the three photocurrent modes

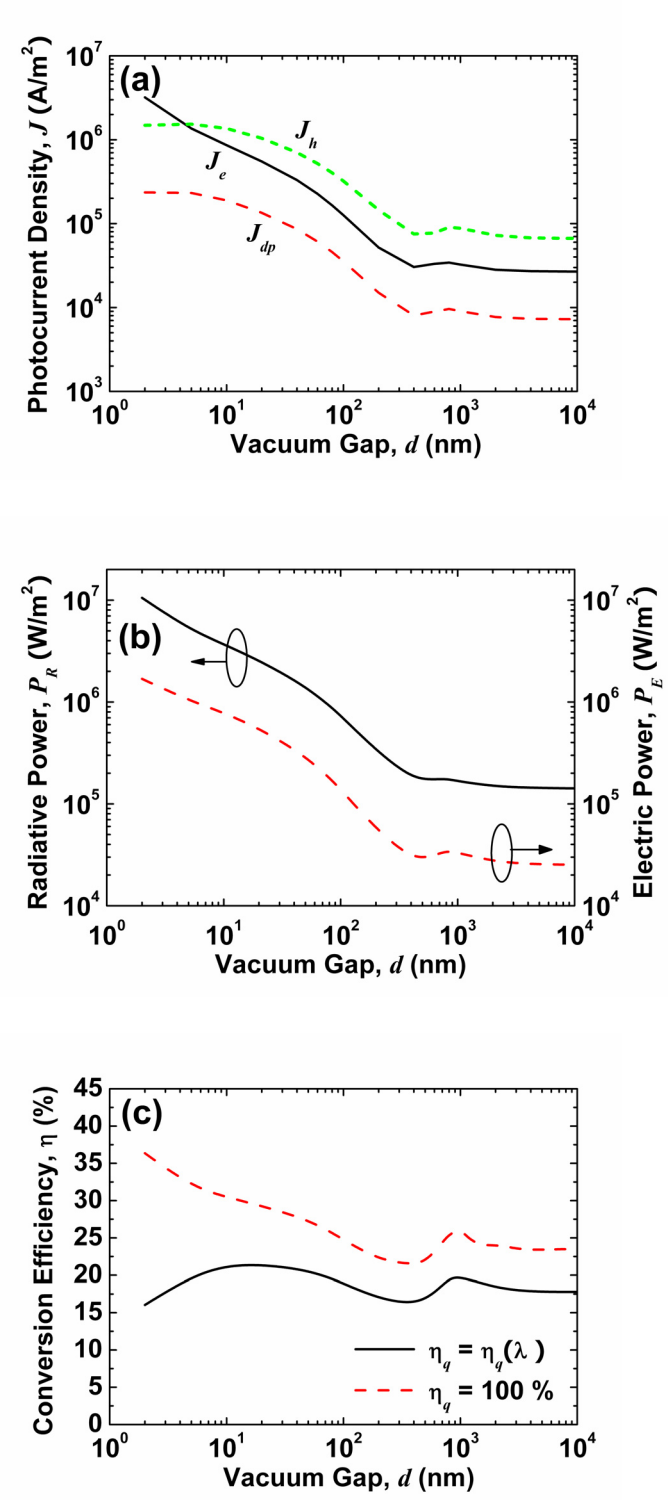

Figure 7.5 (a) Local current generations, (b) thermal radiation absorption and electrical power generation, and (c) the conversion efficiency as functions of the vacuum gap width. For comparison, the efficiency when the quantum efficiency is 100 % as an ideal case is also plotted in Fig. (c).

provides the total electrical power generated from the TPV cell, which is plotted in Fig. 7.5(b) along with the absorbed thermal radiative power. Apparently, the near-field enhancement occurs in both the thermal power absorption and electric power generation. The amount of electric power generation at $d = 10$ nm is predicted to be 1 MW/m^2, suggesting that a TPV device of only 4 in^2 in cross sectional area could generate approximately 2.5 kW, which is enough to meet the electricity demand per household in US [26]. This power output density is three orders of magnitude larger than the highest power output density of a novel nanoscale thermionic-tunneling energy conversion system [27]. Based on the calculated thermal radiation and electric power generation, Fig. 7.5(c) shows the conversion efficiency as a function of the gap width. For comparison, the efficiency for the ideal case is also calculated and plotted together under the assumption that the TPV cell has the 100 % quantum efficiency: that is, all the absorbed photons with energy higher than the energy bandgap contribute to the photocurrent generation. When compared to the ideal case, the efficiency for $\eta_q = \eta_q(\lambda)$ is lower than the ideal efficiency by 5 % to 10 %, and even experiences a decrease as the vacuum gap is further reduced below 10 nm. This decreasing efficiency disproves the prediction of previous works that the near-field effect will improve not only the power output but also the efficiency [8,9]. From Eqs. (7.14) and (7.17), this decrease of the efficiency is the combination of decreasing quantum efficiency and increasing thermal radiation absorption. Thus, despite the remarkable enhancement of the electrical power generation, a small gap does not always guarantee higher efficiency in a near-field TPV system.

Along with the realization of a small and parallel gap between the emitter and TPV cell, the rather low conversion efficiency is a technical challenge to overcome in advancing

a near-field TPV system. One approach widely adopted in conventional TPV devices to improve the efficiency is to filter out the radiation whose energy is smaller than the energy bandgap, which has been realized by positioning a wavelength-selective filter between the emitter and TPV cell [2]. However, this approach cannot be used in the near-field TPV system because the added filter thickness may significantly diminish the near-field effects. Instead, the present work suggests a new approach to improve the efficiency while maintaining the near-field enhancement. Figure 7.6 shows the incident thermal radiation onto the TPV cell plotted against the vacuum gap width. The hatched area denotes the unusable energy smaller than the bandgap, which accounts for more than 10 % of the incident energy. Particularly, at vacuum gaps in the order of 100 nm, the fraction of unusable energy becomes more than 20 %, suggesting that recycling the thermal radiation

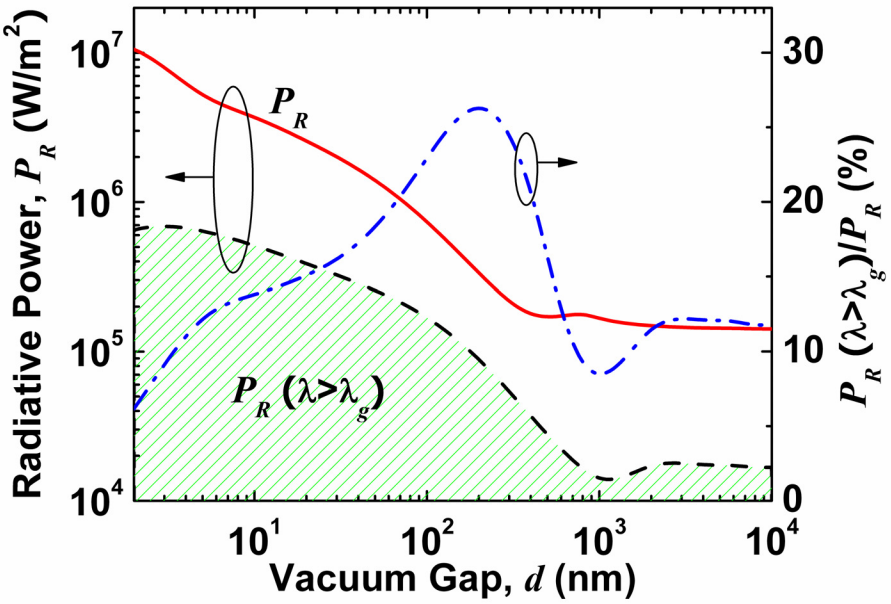

Figure 7.6 Comparison of the total thermal radiation incident on the TPV cell and the unusable portion that is at wavelengths longer than the bandgap wavelength

would significantly improve the efficiency. This improvement could be achieved by depositing a thin metallic layer at the edge of the *p*-*n* junction. The metallic layer will reflect all the radiative heat flux back to the emitter, resulting in two improvements: the radiative energy greater than the bandgap has more chance to be absorbed in the *p*-*n* junction after the reflection. The unusable energy lower than the bandgap is reflected back to the emitter and reabsorbed, reducing the energy required to keep the emitter at the same temperature and thus improving the conversion efficiency. For example, if the vacuum gap is 100 nm and all the reflected thermal radiation is absorbed in the tungsten emitter, around 23 % of the thermal radiation could be reused, improving the conversion efficiency from 18.8 to 24.5 %.

7.4 Conclusion

This work evaluates the performance and efficiency of near-field TPV energy conversion systems by considering the thermal radiation absorption and corresponding photocurrent generation in different regions of the TPV cell. The use of a direct calculation scheme in multilayered structures allows the calculation of absorption patterns of near-field radiation, through which this study demonstrates the near-field effect on the penetration depth. Strong absorption of near-field thermal radiation at the surface significantly affects the photocurrent generation, resulting in a reduction of the quantum efficiency. Contrary to the ideal case with 100 % quantum efficiency, the calculated conversion efficiency decreases when the vacuum gap is smaller than 10 nm, suggesting the existence of an optimal gap of maximum conversion efficiency. Based on the rigorous performance analysis, this study proposes the use of a thin metallic layer as a photon-recycling mirror to improve the efficiency of the near-field TPV system.

7.5 References

[1] T. J. Coutts, "A review of progress in thermophotovoltaic generation of electricity," *Renewable and Sustainable Energy Reviews*, vol. 3, pp. 77-184, 1999.

[2] S. Basu, Y.-B. Chen, and Z. M. Zhang, "Microscale radiation in thermophotovoltaic devices - A review," *International Journal of Energy Research*, 2007 (available online, doi: 10.1002/er.1286).

[3] K. Joulain, J. P. Mulet, F. Marquier, R. Carminati, and J. J. Greffet, "Surface electromagnetic waves thermally excited: Radiative heat transfer, coherence properties and Casimir forces revisited in the near field," *Surface Science Reports*, vol. 57, pp. 59-112, 2005.

[4] C. J. Fu and Z. M. Zhang, "Nanoscale radiation heat transfer for silicon at different doping levels," *International Journal of Heat and Mass Transfer*, vol. 49, pp. 1703-1718, 2006.

[5] A. I. Volokitin and B. N. J. Persson, "Radiative heat transfer between nanostructures," *Physical Review B*, vol. 6320, 205404, 2001.

[6] J. L. Pan, H. K. H. Choy, and C. G. Fonstad, "Very large radiative transfer over small distances from a black body for thermophotovoltaic applications," *IEEE Transactions on Electron Devices*, vol. 47, pp. 241-249, 2000.

[7] M. D. Whale and E. G. Cravalho, "Modeling and performance of microscale thermophotovoltaic energy conversion devices," *Ieee Transactions on Energy Conversion*, vol. 17, pp. 130-142, 2002.

[8] A. Narayanaswamy and G. Chen, "Surface modes for near field thermophotovoltaics," *Applied Physics Letters*, vol. 82, pp. 3544-3546, 2003.

[9] M. Laroche, R. Carminati, and J. J. Greffet, "Near-field thermophotovoltaic energy conversion," *Journal of Applied Physics*, vol. 100, 063704, 2006.

[10] S. M. Rytov, Y. A. Kravtsov, and V. I. Tatarskii, *Principles of Statistical Radiophysics*, vol. 4, Berlin: Springer-Verlag, 1989.

[11] L. Mandel and E. Wolf, *Optical Coherence and Quantum Optics*, Cambridge: Cambridge University Press, 1995.

[12] L. Tsang, J. A. Kong, and K.-H. Ding, *Scattering of Electromagnetic Waves, Theories and Applications*, New York: J. Wiley, 2000.

[13] W. C. Chew, *Waves and Fields in Inhomogeneous Media*, New York: IEEE Press, 1995.

[14] A. Narayanaswamy and G. Chen, "Thermal emission control with one-dimensional metallodielectric photonic crystals," *Physical Review B*, vol. 70, 125101, 2004.

[15] A. Narayanaswamy and G. Chen, "Thermal radiation in 1D photonic crystals," *Journal of Quantitative Spectroscopy & Radiative Transfer*, vol. 93, pp. 175-183, 2005.

[16] E. D. Palik and G. Ghosh, *Handbook of Optical Constants of Solids*, San Diego: Academic Press, 1998.

[17] J. A. Gonzalez-Cuevas, T. F. Refaat, M. N. Abedin, and H. E. Elsayed-Ali, "Modeling of the temperature-dependent spectral response of $In_{1-x}Ga_xSb$ infrared photodetectors," *Optical Engineering*, vol. 45, 044001, 2006.

[18] P. Yeh, *Optical Waves in Layered Media*, New York: Wiley, 1988.

[19] M. G. Mauk and V. M. Andreev, "GaSb-related materials for TPV cells," *Semiconductor Science and Technology*, vol. 18, pp. S191-S201, 2003.

[20] R. Vaillon, L. Robin, C. Muresan, and C. Menezo, "Modeling of coupled spectral radiation, thermal and carrier transport in a silicon photovoltaic cell," *International Journal of Heat and Mass Transfer*, vol. 49, pp. 4454-4468, 2006.

[21] D. M. Caughey and R. E. Thomas, "Carrier mobilities in silicon empirically related to doping and field," *Proceedings of the IEEE*, vol. 55, pp. 2192-2193, 1967.

[22] S. M. Sze, *Physics of Semiconductor Devices*, 2nd ed., New York: Wiley, 1981.

[23] C. A. Dimitriadis, "Determination of Surface Recombination Velocity in Semiconductor Layers by Light Excitation of Schottky Barriers," *Journal of Physics D-Applied Physics*, vol. 16, pp. 1303-1306, 1983.

[24] N. W. Ashcroft and N. D. Mermin, *Solid State Physics*, Philadelphia: Saunders College, 1976.

[25] P. F. Baldasaro, J. E. Raynolds, G. W. Charache, D. M. DePoy, C. T. Ballinger, T. Donovan, and J. M. Borrego, "Thermodynamic analysis of thermophotovoltaic efficiency and power density tradeoffs," *Journal of Applied Physics*, vol. 89, pp. 3319-3327, 2001.

[26] Energy Information Administration, *Househod Electricity Reports*, 2005.

[27] T. F. Zeng, "Thermionic-tunneling multilayer nanostructures for power generation," *Applied Physics Letters*, vol. 88, 153104, 2006.

CHAPTER 8

CONCLUSIONS AND FUTURE RECOMMENDATIONS

8.1 Conclusions

This work presented experimental and theoretical explorations of micro/nanoscale energy transport underlying the operation of the heated microcantilever and the near-field thermophotovoltaics. The research investigated two main areas of interest: 1) Electrical and thermal characterization of the heated microcantilever when the cantilever is off the substrate as well as on the substrate, and 2) performance analysis of the near-field thermophotovoltaic energy conversion system.

8.1.1 Characterization of heated microcantilevers

The first area of interest was motivated by a desire to use a heated cantilever as a thermal metrology tool in various operation conditions. Extensive investigation on the periodic-heating operation of the heated cantilever revealed that the driving frequency as well as the input voltage should be wisely chosen to safely and appropriately operate the cantilever for its purpose. Related with two thermally-determined time constants, i.e., *settling time constant* and *thermal time constant*, there are two distinctive frequency regions in which the cantilever shows different electrical and thermal behaviors. When the cantilever is operated with a lower frequency than its settling time constant, the cantilever voltage signal is composed of higher odd-harmonics due to the nonlinear cantilever TCR. If a driving frequency is higher than the thermal time constant, the

cantilever cannot thermally respond to the fast oscillation of the input power and stays in thermal steady state. Moreover, electrical impedance begins to play an important role in the cantilever response. The heated cantilever was also characterized at cryogenic temperatures and in vacuum, seeking the feasibility of using heated cantilevers in cryogenic environments. The DC characterization showed that the cantilever can be heated above 300 K when its environment is at 77 K. In AC characterization, thermal impedance of the cantilever was determined using a developed thermal transfer function, through which the thermophysical properties of the cantilever could be obtained. Investigation of the cantilever thermal impedances also revealed that regardless of temperature, the cantilever thermal response becomes out of phase and restricted to the heater region as a driving frequency increases. Based on this work, the operation domain of the heated microcantilever can be broadened: the cantilever can now be operated under steady- as well as periodic-heating with the same functionality in various environments, from cryogenic to room temperature and from vacuum to atmospheric pressure.

More investigation was made on the cantilever when it is engaged on the substrate. In this case, substantial amount of heat is transferred from the cantilever to the substrate through the sub-micron air gap and, moreover, is very sensitive to the air gap change. Monitoring the cantilever signal will provide the topography of the substrate with a remarkable sensitivity and resolution. This work went further by operating the heated cantilever in tapping mode. Since the tapping frequency exceeds its thermal time constant, the cantilever stays in thermal steady state even in oscillation, allowing the tapping mode thermally-sensed topography. The cantilever-to-substrate heat transfer was measured with an on-substrate resistive thermometer having a 140 nm lateral resolution. The

measurement confirmed that up to 70 % of the cantilever power is transferred to the substrate, heating the substrate. Maximum temperature change of a 1 μm SiO2-coated silicon substrate is only around 7 K due to the large thermal conductivity of silicon. Other substrates with different thermal conductivities would experience different temperature change, affecting the cantilever performance in turn. The estimated contact thermal conductance is around 40 nW/K, much smaller than the air gap thermal conductance: the air conduction through the cantilever-substrate gap is the dominant heat transfer mechanism.

8.1.2 Near-field thermophotovoltaics

A strong need to develop a new type of sustainable energy conversion system has motivated the second part of this dissertation on a near-field TPV device. Since the near-field thermal radiation is a key energy transport in the system, surface and bulk polaritons and their effects on the near-field radiation of a multilayered structure was first investigated. When surface and bulk polaritons are excited, the radiative properties are significantly changed. Moreover, the layer thickness as well as vacuum gap between two objects was shown to make a significant contribution on the thermal radiation due to photon tunneling. Based on the accumulated knowledge of the near-field radiation, performance and the energy conversion efficiency of the near-field TPV system were rigorously investigated by considering local radiation absorption and photocurrent generation in the TPV cell. The near-field effect indeed alters not only the amount of radiative heat transfer but also the photon penetration depth and photocurrent generation, resulting in the reduction of the quantum efficiency. The evaluation of the energy conversion efficiency demonstrated that while the near-field radiation can enhance the

power throughput, the conversion efficiency is not much improved and may be even reduced. In order to enhance the conversion efficiency, recycling of photon energy with a metallic mirror at the bottom of the TPV cell was envisaged.

8.2 Recommendations for Future Research

This plan for future research addresses thermal micro/nanoelectromechanical systems, nanoscale energy conversion, and near-field optics. The proposed research would seek to develop micro/nanoscale thermal and optical sensors, investigate phonon-, photon- and electron-coupled energy transport at the nanoscale, and apply nanoscale energy transport in novel energy conversion systems. This research will ultimately lead to nanoscale thermal and optical engineering that can measure and control reactions between small numbers of molecules and the creation of nanoscale energy systems that could improve the efficiency much better than their macroscale counterparts. Figure 8.1 illustrates the overview of the proposed research. The results of this dissertation are listed under the headings 'Thermal metrology using heated microcantilevers' and 'Near-field thermophotovoltaics.' Each area offers opportunities for future work, both by deepening the present work and by broadening them into related areas.

8.2.1 Thermal micro/nanoelectromechanical systems (M/NEMS)

Recent advances in nanoscale devices, e.g., fluidic channels, integrated circuits, and electronic biological devices, demand highly accurate nanoscale thermal probes that can investigate and control profiles of heat transfer and thermal reactions. The development of thermal imaging and spectroscopy with a spatial resolution at tens of

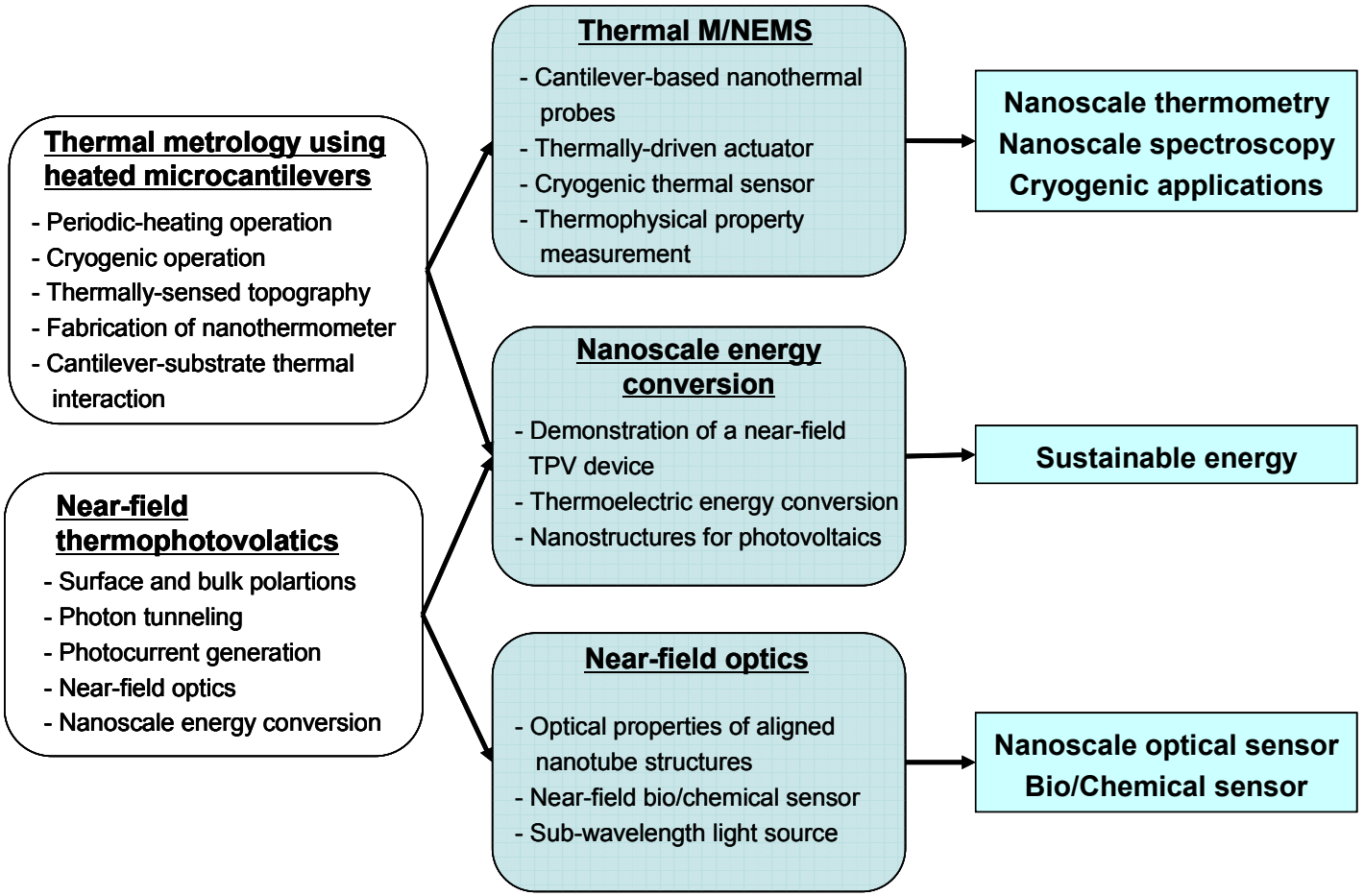

Figure 8.1 Overview of planned future research based on progresses achieved in this dissertation

nanometers will be of great importance. By using nanolithography currently available, a nanometer scale sensing probe can be achieved at the free end of an AFM cantilever, enabling approximately the tens of nanometer spatial resolution, sub-microsecond temporal resolution, and milli-Kelvin thermal resolution. The use of the fabricated thermal probe in the AFM platform will provide nano-resolution thermal images with minimum thermal distortion along with topographic images. When combined with a Fourier-transform infrared interferometer or a monochromator as a frequency-modulated light source focused on the sample, the thermal scanning for different frequencies will provide the photothermal absorption spectra with nano-resolution [1]. Successful completion of the research would bring broad impact on various fields, such as synthesis and inspection of nanomaterials, nanoscale defects or inhomogeneities detection, hot-spot detection of nanoscale IC devices, and chemical characterization of nanoparticle-embedded polymers. Besides nanoscale thermometry and spectroscopy, thermal M/NEMS for cryogenic applications will overcome the technical challenges in current cryogenic thermal sensors and actuators. Particularly, microdevices that sense the temperature and flow rate of coolant and the vacuum condition will offer the opportunity in realizing small cryogenic devices customized for healthcare or defense systems.

8.2.2 Nanoscale energy conversion

As mentioned in Chapter 7, electric power generation of a near-field TPV system could be as high as 1 MW/m^2, suggesting that a TPV device of only 4 in^2 in cross sectional area could generate enough electricity meeting the power demand of one household. However, there has been almost no report that experimentally demonstrates the near-field TPV system, mainly due to the difficulty in realizing an extremely small

and parallel gap between two objects. Recently, a new idea was suggested for realizing a small gap, which introduced partially contacting solid spacers with dielectric nanowires or nanoparticles [2]. By placing nanowires or nanoparticles between the emitter and TPV cell, a parallel gap of sub-100 nm could be realized, enabling the experimental demonstration of the near-field TPV energy conversion. Moreover, with the same setup, more intensive experimental investigation of the near-field thermal radiation would be possible, resolving the debate on whether the near-field thermal radiation can be experimentally verified [3] or not [4] at room temperature. This research will be extended to more general research on nanoscale energy conversions, such as nanoscale thermoelectric energy conversion and nanostructured photovoltaic cells.

8.2.3 Near-field optics

Development of nanotechnology has also improved the optics-based bio/chemical sensors [5]. For example, recent study showed that nanostructures in a wing of tropical *Morpho* butterflies give a different optical response to different individual vapors, which drastically outperforms that of existing photonic sensors [6]. Since a carbon nanotube (CNT) is a very strong candidate for nanoscale optical sensor and light emitter, the optical properties of individual nanotubes and nanotube-embedded composite films have been intensively studied [7-9]. However, difficulties in aligning nanotubes to desired direction and severe light scattering due to intervening nanotubes have limited the practical applications of nanotubes as an optical sensor. Recently, new methods to pattern vertically aligned nanotubes on polymer substrate was suggested [10], opening a possibility to use an aligned nanotube structure for optical metrology. Particularly, periodic grating structures with aligned nanotubes are of great interest, because grating

structures are being vividly used in various optical-based instrumentations such as interferometry, spectroscopy, and optical imaging. Besides the light diffraction due to the periodic feature of the gratings, the interference effect that would occur between individual nanotubes will provide very unique optical properties, which hopefully could be used for ultra-sensitive optical sensors. Successful completion of the research will not only provide deep understanding of the near-field optics in aligned nanostructures but also open practical applications of nanotube/wire structures for the sensor technology.

Another application of near-field optics is a subwavelength light source. The subwavelength light source will provide enormous opportunities in optics-related fields such as optical data storage and optical sensor. Among other possible ways to realize the subwavelength light source, thermal emission is in particular interest. Thermal emission has been known to be incoherent in both spectrum and direction. However, the recent theoretical and experimental studies showed that the thermal emission can become spectrally and directionally coherent with one dimensional photonic crystal (PC) combined with a thin metallic film [11-13]. The doped silicon cantilever or bridge structure can increase the temperature over 1000 K, allowing the thermal emission with the peak wavelength shorter than 3 μm, feasible as an infrared (IR) light source. Thus, by combining coherent thermal emission system with the doped cantilever/bridge MEMS structure that is fabricated in subwavelength size, the subwavelength IR light source could be realized, which is the objective of the proposed research.

8.3 References

[1] A. Hammiche, L. Bozec, M. J. German, J. M. Chalmers, N. J. Everall, G. Poulter, M. Reading, D. B. Grandy, F. L. Martin, and H. M. Pollock, "Mid-infrared microspectroscopy of difficult samples using near-field photothermal microspectroscopy," *Spectroscopy*, vol. 19, pp. 20-42, 2004.

[2] T. F. Zeng, "Thermionic-tunneling multilayer nanostructures for power generation," *Applied Physics Letters*, vol. 88, 153104, 2006.

[3] W. Muller-Hirsch, A. Kraft, M. T. Hirsch, J. Parisi, and A. Kittel, "Heat transfer in ultrahigh vacuum scanning thermal microscopy," *Journal of Vacuum Science & Technology A*, vol. 17, pp. 1205-1210, 1999.

[4] J. B. Xu, K. Lauger, R. Moller, K. Dransfeld, and I. H. Wilson, "Heat transfer between two metallic surfaces at small distances," *Journal of Applied Physics*, vol. 76, pp. 7209-7216, 1994.

[5] Y. T. Yang, C. Callegari, X. L. Feng, K. L. Ekinci, and M. L. Roukes, "Zeptogram-scale nanomechanical mass sensing," *Nano Letters*, vol. 6, pp. 583-586, 2006.

[6] R. A. Potyrailo, H. Ghiradella, A. Vertiatchikh, K. Dovidenko, J. R. Cournoyer, and E. Olson, "*Morpho* butterfly wing scales demonstrate highly selective vapour response," *Nature Photonics*, vol. 1, pp. 123-128, 2007.

[7] W. A. de Heer, W. S. Bacsa, A. Chatelain, T. Gerfin, R. Humphreybaker, L. Forro, and D. Ugarte, "Aligned Carbon Nanotube Films - Production and Optical and Electronic-Properties," *Science*, vol. 268, pp. 845-847, 1995.

[8] S. M. Bachilo, M. S. Strano, C. Kittrell, R. H. Hauge, R. E. Smalley, and R. B. Weisman, "Structure-assigned optical spectra of single-walled carbon nanotubes," *Science*, vol. 298, pp. 2361-2366, 2002.

[9] J. A. Misewich, R. Martel, P. Avouris, J. C. Tsang, S. Heinze, and J. Tersoff, "Electrically induced optical emission from a carbon nanotube FET," *Science*, vol. 300, pp. 783-786, 2003.

[10] E. Sunden, J. K. Moon, C. P. Wong, W. P. King, and S. Graham, "Microwave assisted patterning of vertically aligned carbon nanotubes onto polymer substrates," *Journal of Vacuum Science & Technology B*, vol. 24, pp. 1947-1950, 2006.

[11] B. J. Lee, C. J. Fu, and Z. M. Zhang, "Coherent thermal emission from one-dimensional photonic crystals," *Applied Physics Letters*, vol. 87, 071904, 2005.

[12] B. J. Lee and Z. M. Zhang, "Design and fabrication of planar multilayer structures with coherent thermal emission characteristics," *Journal of Applied Physics*, vol. 100, 063529, 2006.

[13] B. J. Lee and Z. M. Zhang, "Coherent thermal emission from modified periodic multilayer structures," *Journal of Heat Transfer*, vol. 129, pp. 17-26, 2007.